



POLITECNICO
MILANO 1863

SCUOLA DI INGEGNERIA INDUSTRIALE
E DELL'INFORMAZIONE

Generalised Conjugate Gradient for the minimisation of energy functionals in deformed nuclei

TESI DI LAUREA MAGISTRALE IN
NUCLEAR ENGINEERING - INGEGNERIA NUCLEARE

Author: Alessandro Sala

Student ID: 247459

Advisor: Prof. Matteo Passoni

Co-advisors: Prof. Gianluca Colò

Academic Year: 2024-25

Abstract

Energy Density Functionals (EDFs) have been used for a few decades in nuclear structure physics, with a large degree of success. Skyrme functionals are a widely used class that has been applied to the study of masses, radii, deformations, spectroscopy reactions and decays. Due to past computational limitations, calculations were often restricted to given symmetric cases, where nuclei have been assumed to be spherically, or axially symmetric. Many codes assume basis expansions that turn out to be not so effective. Only in recent years calculations in a Cartesian mesh without any imposed symmetry have been explored, which still require a major computational effort, often in the form of large computer clusters. Improving the efficiency of the diagonalisation of large-scale matrices is still a major open problem, not only in the field of nuclear physics, but in physics and engineering as a whole. The present work aims at exploring a novel algorithm, the Generalised Conjugate Gradient, to solve the Kohn–Sham equations consistent with the Skyrme EDF, within an unconstrained minimization. The Generalised Conjugate Gradient algorithm is shown to be a robust, and most importantly efficient alternative for the unconstrained minimization of the energy functional, both in well tested spherical systems, as well as in deformed ones.

Keywords: Skyrme functionals, Generalised Conjugate Gradient, Density Functional Theory, deformed nuclei

Abstract in lingua italiana

Negli ultimi decenni, i Funzionali di Densità di Energia hanno ottenuto un notevole successo nello studio della struttura nucleare. Tra questi, i funzionali di Skyrme rappresentano una delle classi più ampie e utilizzate per l'analisi di raggi, masse, deformazioni, spettroscopia, reazioni e decadimenti nucleari. In passato, i limiti computazionali hanno imposto di considerare soltanto sistemi con simmetria sferica o assiale. Inoltre, molti codici si basano su espansioni in basi complete, che non sempre garantiscono un risultato ottimale. Negli ultimi anni sono stati sviluppati approcci basati su griglie cartesiane prive di vincoli di simmetria, che tuttavia rappresentano ancora una sfida computazionale rilevante, richiedendo spesso l'impiego di ingenti risorse di calcolo su cluster. L'ottimizzazione delle tecniche di diagonalizzazione per matrici di grandi dimensioni costituisce ancora oggi un problema aperto e di fondamentale importanza, non solo nella fisica nucleare, ma più in generale in fisica e nell'ingegneria. Il presente lavoro esplora l'applicazione dell'algoritmo Generalised Conjugate Gradient (GCG) per la risoluzione delle equazioni di Kohn–Sham derivate dalla minimizzazione di un funzionale di Skyrme, senza assunzioni di simmetria. I risultati mostrano che il GCG rappresenta una soluzione robusta ed efficiente per la minimizzazione di funzionali di energia, sia in sistemi sferici, sia deformati.

Parole chiave: Gradiente coniugato, Teoria del funzionale della densità, nuclei deformati, funzionali di Skyrme

Indice

Abstract	i
Abstract in lingua italiana	iii
Indice	v
Introduction	1
1 Nuclear structure and deformations	5
1.1 Nuclear structure models	5
1.1.1 Phenomenology of the NN interaction	6
1.1.2 Structure models	7
1.2 Nuclear pairing	12
1.3 Nuclear deformations	12
1.3.1 Quadrupole deformation	13
1.3.2 Nilsson model	15
1.3.3 Octupole deformations and parity breaking	17
1.4 Nuclear fission	18
2 State of the art, objectives and methods	23
2.1 State of the art and motivation	23
2.2 State of the Art	24
2.2.1 Basis expansion methods	25
2.2.2 Symmetry-Restricted mesh methods	26
2.2.3 Unconstrained coordinate-space (mesh) methods	26
2.2.4 Towards more efficient unconstrained methods	26
2.3 Objectives	27
2.4 Methods	27
3 Energy functional	29

3.1	Hartree–Fock theory	29
3.1.1	Variational principle	29
3.1.2	Hartree–Fock equations	30
3.1.3	Symmetries in Hartree–Fock	32
3.1.4	Density Functional Theory	34
3.2	Pairing in Hartree–Fock theory	36
3.2.1	BCS theory	36
3.2.2	Hartree–Fock–Bogoliubov theory	39
3.3	Microscopic theory and approaches to nuclear fission	42
3.3.1	Microscopic theory	43
3.3.2	Time-dependent DFT and the TDHF formalism	44
3.3.3	Unconstrained Calculations and Symmetry Breaking	45
3.4	Skyrme	46
3.4.1	Skyrme force	46
3.4.2	Energy density functional	48
3.4.3	Functionals	52
3.5	Coulomb interaction	52
3.6	Energy calculation	54
4	Numerical methods	57
4.1	Finite differences	57
4.1.1	3D mesh	57
4.1.2	Schrödinger equation	58
4.1.3	Poisson equation	60
4.2	Eigenvalue problem	61
4.2.1	Conjugate Gradient and numerical techniques	62
4.2.2	Iterative eigensolvers	66
4.2.3	Generalised Conjugate Gradient	69
4.3	Code implementation details	70
4.3.1	Constraints	71
4.3.2	Details on the implementation of the code	73
4.3.3	Optimal parameters choice	73
4.3.4	Numerical stability	74
5	Results for spherical nuclei	79
5.1	Physical quantities	79
5.1.1	Mean square radii	79
5.2	Parameters and mesh choice	80

5.3	Results for ^{16}O	80
5.3.1	Results neglecting Coulomb interaction	81
5.3.2	Results including Coulomb interaction	82
5.4	Results for heavier nuclei	82
5.5	Comparison with experimental values	83
6	Results for deformed nuclei	89
6.1	Deformation parameters	89
6.1.1	Code parameters and axial constraint	90
6.2	Benchmark for ^{24}Mg	91
6.2.1	HFBTHO code and calculation details	92
6.2.2	EV8 code and calculation details	93
6.2.3	Deformation curve for different functionals	94
6.3	Original results	95
6.3.1	α -clustering in light nuclei	98
6.3.2	Nuclei near the drip lines	100
Conclusion and future developments		103
Bibliografia		107
A	Appendix	119
A.1	Spherical harmonics	119
A.1.1	Algorithm	120
A.2	5-point derivatives	120
A.3	Functional derivatives	120
A.4	\bar{U} , \bar{V} matrix structure	122
Elenco delle figure		123
Elenco delle tabelle		125
List of Symbols		127

Introduction

The theoretical study of atomic nuclei provides a bridge between nuclear physics and nuclear engineering. Starting from a framework consistent with quantum mechanics, the strong interaction, and its underlying symmetries, modern nuclear theory aims to construct models characterised by a limited number of free parameters and ideally capable of predicting both nuclear structure, and reactions, across a wide range of systems. While experimental data have long provided invaluable insight into nuclear properties and processes, only a coherent theoretical description allows for systematic extrapolations towards regions of the nuclear chart, or physical conditions, that remain beyond current experimental reach.

In particular, nuclear fission, despite its crucial importance in nuclear engineering, remains only partially understood from a microscopic standpoint. Current models that use empirical approaches [1, 2], successfully reproduce global quantities like fission barrier heights, fragment mass distributions, and average neutron multiplicities for well studied nuclei. However, these models may rely on a huge number of parameters, which limit their predictive power when extrapolated to systems which are less investigated experimentally. A fully microscopic understanding of the collective dynamics leading from the compound nucleus to scission, the treatment of quantum many-body correlations [3], and the description of fragments emission remain among the major open challenges, particularly relevant for the simulation of next-generation reactors, which require the accurate description of nuclei and fuel materials – far less explored than those employed in traditional thermal systems – to be correctly predicted.

Modern nuclear theory aims at starting from the interaction among nucleons to build a complete description of nuclear properties, using the techniques of quantum many body theory. The use of phenomenological potentials based on the Woods–Saxon one is still relevant, thanks to its computational feasibility and its capability to include shell effects in a simple manner, but it cannot be fully satisfactory as it is simply empirical. At the moment, there are two competing frameworks that try to tackle the microscopic description of nuclei,

- i the *ab-initio* approaches [4], where the many-body method is in principle exact and the interactions is consistent with the symmetries of Quantum Chromodynamics; and
- ii the use of effective interactions and nuclear Density Functional Theory[5, 6].

Ab-initio methods, while technically speaking more rigorous, are still limited as of now, since they can only account for light nuclei or medium-heavy nuclei that can be considered as spherical. Energy density functionals and effective interactions, such as the Skyrme force, on the other hand, are more flexible and less computationally expensive, enabling a much wider representation of nuclei across the whole chart, including heavy nuclei and processes such as fission, fusion, reactions and decays, which are of crucial importance in nuclear engineering.

D Vautherin and D M Brink laid the foundations of the nuclear Hartree–Fock theory using the Skyrme interaction in 1972 [7], through spherically symmetric calculations, which are unable to account for nuclear deformations, essential for nuclei far from magic numbers. Over the years, thanks to the increase in computational performance of modern hardware, more general codes that give up the spherical assumption have been written, mainly using basis expansions on the harmonic oscillator [8, 9], which have the downside of not being able to account for nuclei near the drip lines, due to the diffent asymptotic behaviour of the Gaussian basis in the harmonic oscillator and quasi-resonant states.

In the past twenty years, the use of Cartesian meshes to better account for such cases has been introduced [10–13], often times assuming certain approximations, such as plane reflection symmetries [14] and axial symmetry [13]. The use of fully unconstrained Hartree–Fock methods, of critical importance for exotic deformations, is still a novel endeavour that only a handful of implementations have tackled, due to the high computational cost.

The aim of this work is to explore a new computational approach, the Generalised Conjugate Gradient method, to efficiently solve Skyrme functionals without spatial constraints. This thesis is organised as follows:

- In Chapter 1, a short, comprehensive introduction to nuclear physics and its open problems is given, as to prime the reader on the essential physical properties of atomic nuclei, starting from phenomenological facts and empirical models. A formal description of nuclear deformations and fission is also given, to highlight the importance of symmetry breaking.
- In Chapter 2, the motivations and objectives of this work are presented, along with a summary of the methods used to achieve them.

- In Chapter 3, the theoretical framework used in the present work is reviewed, by introducing aspects of Hartree–Fock theory, Density Functional Theory and the EDF employed.
- In Chapter 4, the numerical methods used in this work are presented, along with actual implementations in writing the code.
- In Chapter 5, results for the spherically symmetric case are presented as a way of benchmarking the new implementation of this thesis, along with a description of the main physical quantities we compare.
- In Chapter 6, benchmarks for the deformed nucleus ^{24}Mg are shown, after which original results regarding the study of clustering formation in ^{20}Ne , and the separation energy of the near-drip lines nuclei ^{42}Si and ^{28}S are presented.

In Section 4.2 of Chapter 4, the analysis and implementation work presented was developed within the additional thesis activity carried out for the Honours Programme *Scientific Research in Industrial Engineering – Nuclear Science and Technology*.

1 | Nuclear structure and deformations

In this chapter, a very concise introduction to nuclear structure physics is provided, with the goal of delivering the means to understand the essential phenomenology, physical quantities, and terminology of atomic nuclei. In this way, the reader will have the necessary background to understand nuclear deformations and other properties discussed in later sections. The reader may refer to introductory textbooks on nuclear physics, such as Refs. [15, 16] for a more in-depth treatment of the subject and Ref. [17] for a focus on many-body theory.

This chapter is organised as follows. First, in Section 1.1, we will review the main empirical facts about nuclides, such as the shapes of particle density distributions, the nuclear binding energies and the phenomenological models employed to describe them. We shall then move on to more advanced topics, that are able to complete the general description of nuclear structure, namely nuclear pairing and nuclear deformations in Section 1.2 and Section 1.3 respectively. Lastly, in Section 1.4, we will review the nuclear fission process, discuss a simple model to describe it, and highlight the importance of deformations to accurately describe it.

1.1. Nuclear structure models

The study of low-energy hadron physics has always been a challenging task. This is due to the known fact that the strong force, which is responsible for the interaction between nucleons, is not perturbative at low energies, as opposed to the atomic case for the Coulomb interaction, whose coupling can be assumed as constant at all energies. Nevertheless, both problems have in common the fact that one is confronted with quantum many-body systems, thanks to which they share some challenges and the corresponding solutions, when present.

1.1.1. Phenomenology of the NN interaction

It is possible to obtain a good insight on nuclear structure, by using empirical data obtained experimentally on the bulk properties of nuclei, such as the binding energy and the particle density.

Binding energies

Let us start with the binding energy. We can define it as the mass defect of the nucleus with respect to the constituents – protons and neutrons – isolated from each other. If Z is the number of protons, N the number of neutrons, and $A = N + Z$ the nuclear mass, then the binding energy E_B is given by

$$E_B = (Zm_p + Nm_n - M)c^2, \quad (1.1)$$

where m_p is the proton mass, m_n the neutron mass, and M the nucleus mass.

In Figure 1.1, the binding energy per nucleon E_B/A as a function of A is presented. As shown in the figure, the binding energy per nucleon rapidly saturates and stalls around 7 MeV just after $A = 4$; this striking behaviour is due to nucleons interacting only with near neighbours, since the strong force is a short-range interaction. Otherwise, the trend would follow a behaviour similar to $\sim A$ as in the Coulomb interaction case, meaning the binding energy per nucleon would be linear with the mass number.

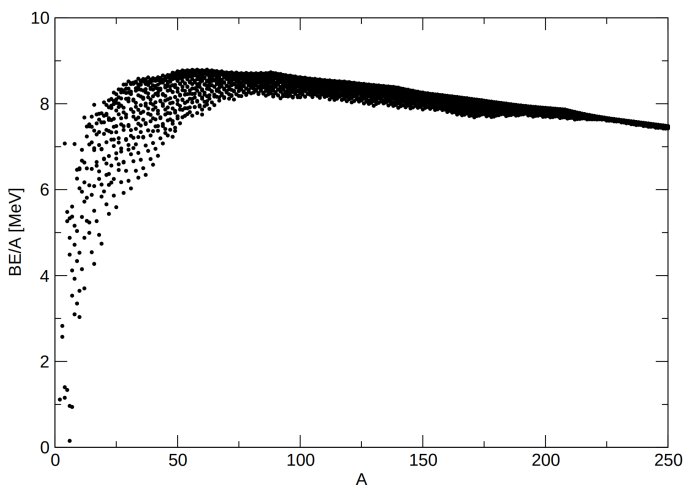


Figura 1.1: Binding energy per nucleon as a function of A . Due to the short range of the strong force, this value saturates around 7 MeV, with a steady, dim decrease after ^{56}Fe . Figure taken from [5].

Nuclear density

An important aspect of nuclear phenomenology that can be accessed experimentally is the nuclear charge density, most notably through elastic electron-nucleus scattering [18]. The measured form factor can be related to the Fourier transform of the charge density, from which the spatial distribution is reconstructed. The resulting densities, as a rule, are reproduced by a Fermi-like distribution of the form

$$\rho(r) = \frac{\rho_0}{1 + e^{(r-R_0)/a}}, \quad (1.2)$$

where R_0 is the nuclear radius, which can be parametrised as $R_0 \approx 1.2A^{1/3}$, and a is the diffusivity, whose value determines how sharp the density drops from its saturation value $\approx \rho_0$ to ≈ 0 . Neutron, or mass densities are known less accurately. Regardless, proton and hadron scattering experiments suggest that neutron densities are very close to proton densities in the inner part, and the neutron excess is visible at the surface. The saturation density ρ_0 is generally universal for all nuclei, amounting to $\approx 0.16 \text{ fm}^{-3}$.

1.1.2. Structure models

We shall now review the main phenomenological models that attempt to describe the nuclear structure.

Liquid drop model

One, if not the first successful model, is the liquid drop model. It is based on the assumption that the nucleus behaves as a liquid droplet, where forces among constituents saturate. This hypothesis, formulated by G Gamow, culminated in the formalization of the semi-empirical mass formula (SEMF) by N Bohr and C F von Weizsäcker in 1935 [19], which reads

$$E_B = a_V A - a_S A^{2/3} - a_C \frac{Z(Z-1)}{A^{1/3}} - a_A \frac{(N-Z)^2}{A} + \delta_P \quad (1.3)$$

where E_B is the binding energy of the nucleus. Each term has a different physical meaning:

- $a_V A$ is the volume energy of the nucleus, given by the approximately constant binding energy per nucleon, which makes the total energy proportional to A ;
- $a_S A^{2/3}$ is the surface energy, a correction to the volume energy due to outer nucleons interacting with fewer nucleons than those in the inner bulk, meaning that a_S is of the same order of a_V ;
- $a_C Z(Z-1)/A^{1/3}$ is the approximation to the Coulomb energy repulsion of the

nucleus, assuming the protons are uniformly distributed;

- $a_A(N-Z)^2/A$ is the asymmetry energy, which is due to the Pauli exclusion principle: since protons and neutrons occupy their respective states, a high imbalance of one species or the other implies that the more numerous species – typically the neutrons – is pushed to higher-energy levels; and
- $\delta_P = a_P A^{-1/2}$ refers to the pairing contribution, due to the increase in binding energy of an even number of neutrons and/or protons. More details on the pairing energy are given in Section 1.2.

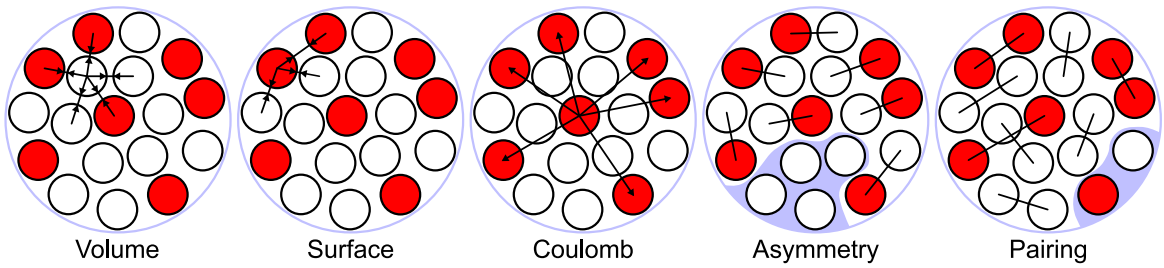


Figura 1.2: Visual representation of the liquid drop model. Figure taken from [20].

The SEMF can be fitted on experimental data to get a good estimate of binding energies [21], but it still lacks the ability of describing many aspects of nuclear structure, mainly, the nuclear shell structure, which can account for magic numbers and nuclear deformations, unless shell corrections are explicitly taken into account.

An example of the SEMF parametrisation is given in Table 1.1, values are taken from [22].

Coefficient	a_V	a_S	a_C	a_A	a_P
Value [MeV]	15.8	17.8	0.711	23.7	11.2

Tabella 1.1: A typical parametrisation of the coefficients in the SEMF (1.3). Values are taken from [22].

Shell corrections

The liquid drop model, while being a good approximation for the description of the nuclear binding energy, it only accounts for the Pauli exclusion principle and the saturation of the strong force, providing only a partial description of the full quantum mechanical

nature of the nucleus. Unfortunately, unlike the atomic case, there is no external source of the field to which nucleons are subject to, since it is generated by the nucleons themselves; nonetheless, the formulation of an empirical mean-field potential which reproduces experimental data has been proven to be successful in providing useful corrections.

The so called Woods–Saxon potential is an empirical field used for modelling the average field to which an independent nucleon is subject to in a nucleus. It is formulated as to follow the shape of the nuclear density (1.2), and it reads

$$U(\mathbf{r}) = -\frac{U_0(A, N)}{1 + e^{\frac{r-R}{a}}}, \quad (1.4)$$

where U_0 is the potential depth

$$U_0(A, N) = U_0 \left(1 \pm \kappa \frac{2N - A}{A} \right), \quad (1.5)$$

and the $+$ and $-$ signs refer to protons and neutrons respectively. R refers to the radius of the nuclear surface, parametrised as

$$R = r_0 A^{1/3} \quad (1.6)$$

and a is the surface diffuseness, as in the density expression (1.2).

Spin-orbit coupling The success of the shell model is mainly due to the possibility of including the spin-orbit coupling, which is incorporated through a term that reads

$$U_{LS}(\mathbf{r}) = U_0^{LS} \left(\frac{r_0}{\hbar} \right)^2 \frac{1}{r} \frac{d}{dr} \left(\frac{1}{1 + e^{\frac{r-R}{a}}} \right). \quad (1.7)$$

A typical parametrisation of the values in the Woods–Saxon potential and the spin-orbit term is given in Table 1.2, values are taken from [23].

U_0 [MeV]	κ	r_0 [fm]	a [fm]	U_0^{LS} [MeV·fm 2]
52.1	0.639	1.260	0.662	22.0

Tabella 1.2: Typical Woods–Saxon potential parameters. Values are taken from [23].

As shown in Table 1.2, the spin-orbit coupling strength is large, compared to the atomic case, this causes a bigger splitting of the energy levels, leading to the formation of stable closed shells when the magic numbers 8, 20, 28, ... are reached, as shown in Figure 1.3.

Coulomb interaction In the spherical case, the Coulomb interaction can be taken, in a first approximation, as the energy potential produced by a sphere of charge Z and radius R , which reads

$$U_C(r) = Ze^2 \begin{cases} \frac{3-(r/R)^2}{2R} & r \leq R, \\ \frac{1}{r} & r > R. \end{cases} \quad (1.8)$$

The complete Hamiltonian then reads

$$\hat{H} = \hat{T} + U + U_{\text{LS}} + U_C, \quad (1.9)$$

where U_C is present only when solving for the proton shells. In the spherical case, the solution to the eigenvalue problem $\hat{H}\psi = E\psi$ is of the form

$$\psi_{nljm_j} = \frac{u_{nl}(r)}{r} [Y_{nl}(\hat{\mathbf{r}}) \otimes \chi_{1/2}]_{jm_j} \quad (1.10)$$

where $Y_{nl}(\hat{\mathbf{r}})$ is the spherical harmonic function of degree l and order m , the $\hat{\mathbf{r}}$ notation is used to denote dependence on the azimuthal and polar angles of \mathbf{r} , the symbol \otimes takes the meaning of the angular momentum coupling with the spinor $\chi_{1/2}$, and $u_{nl}(r)$ satisfies the reduced Schrödinger equation

$$\left(-\frac{\hbar^2}{2m} \frac{d^2}{dr^2} + \frac{\hbar l(l+1)}{2mr^2} + U(r) \right) u_{nl} = Eu_{nl}. \quad (1.11)$$

The effect of the spin-orbit coupling U_{LS} and the Coulomb repulsion U_C could be accounted for by using first order perturbation theory.

Harmonic oscillator

A small digression on the harmonic oscillator is in order. The solution of the spherical potential

$$U_{\text{HO}}(\mathbf{r}) = \frac{1}{2}m\omega^2 r^2, \quad (1.12)$$

produces the spherical harmonic oscillator basis, which is very similar to the basis one would get solving for the Woods–Saxon potential, provided that $\hbar\omega$ is taken as $41/A^{1/3}$ MeV. As a matter of fact, the harmonic oscillator basis is often used to perform calculations in nuclear physics. We will see in Section 4.3 that a harmonic oscillator basis is used as starting guess for the numerical solution of a Woods–Saxon potential.

Shell structure

A graphical representation of the shells for a harmonic oscillator is shown in Figure 1.3, where the contribution of the spin-orbit coupling is also accounted for; compared to the atomic case, shells whose total angular momentum is $j = l + 1/2$ are lowered in energy, viceversa for total angular momentum $j = l - 1/2$, due to the sign of the spin-orbit coupling U_0^{LS} of $U_{\text{LS}}(\mathbf{r})$ in Equation (1.7).

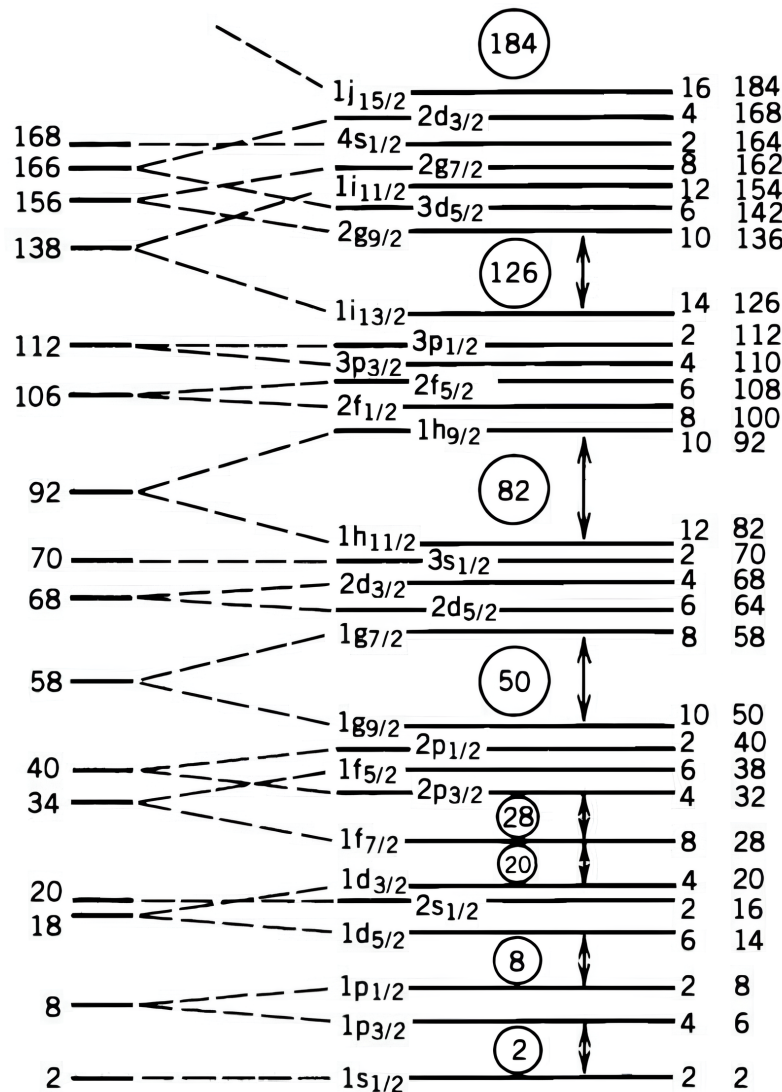


Figura 1.3: Graphical representation of the harmonic oscillator shells, together with the spin-orbit coupling. Shells whose total angular momentum is $j = l + 1/2$ are lowered in energy, viceversa for total angular momentum $j = l - 1/2$. Figure adapted from [24].

1.2. Nuclear pairing

In the semi-empirical mass formula (1.3), the δ_p term can be parametrised as

$$\delta_p = \begin{cases} +\delta_0 & \text{if } N \text{ and } Z \text{ are even,} \\ 0 & \text{if } A \text{ is odd,} \\ -\delta_0 & \text{if } N \text{ and } Z \text{ are odd,} \end{cases} \quad (1.13)$$

hence having an even number of neutrons and/or protons increases the binding energy of the nucleus. A common choice for δ_0 is

$$\delta_0 = a_P A^{-1/2} \text{ MeV.}$$

A typical value for a_P is reported in Table 1.1. This is a phenomena closely related to superconductivity, as nucleons of the same type form pairs that are strongly correlated and increase the nuclear binding. An experimental evidence of this fact is known as odd-even staggering, where the separation energy

$$S_n = E_B(A+1, Z) - E_B(A, Z), \quad (1.14)$$

is higher for even A , an increase that corresponds to the energy necessary to break a pair. A graphical representation of the odd-even staggering for Sn isotopes is shown in Figure 1.4. We will see in Section 3.2 the two main methods to account for pairing at a microscopic level.

1.3. Nuclear deformations

If we were to observe the ratio between the first and second excited states energies of even-even nuclei, respectively $E(2^+)$ and $E(4^+)$, we would find that for nuclei where both N and Z are far from magic numbers, the ratio could be well-approximated as

$$\frac{E(4^+)}{E(2^+)} \approx 3.33. \quad (1.15)$$

The ratio (1.15) can be explained by the collective rotation of the nucleus, when rotational symmetry is broken. Denoting by J the total angular momentum of this rotation, the quantized rotor energy reads

$$E_{\text{rot}} = \frac{\hbar^2}{2I} J(J+1), \quad (1.16)$$

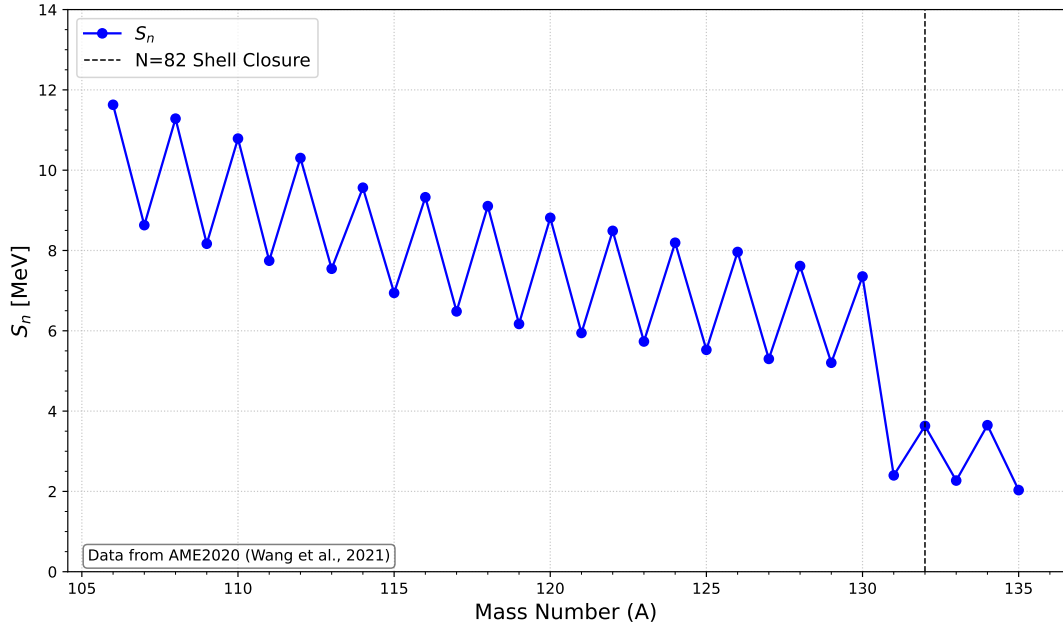


Figura 1.4: Odd-even staggering for Sn isotopes. Data taken from [25].

where \mathcal{I} is the nuclei's moment of inertia. Taking the ratio of Equation (1.16) when $J = 4$ and $J = 2$, yields

$$\frac{20}{6} \approx 3.33. \quad (1.17)$$

Since there are many nuclei that display this property, it becomes obvious that nuclear deformations play a central role in the description of nuclear structure; as such, we shall now give a description of the nuclear shape in a formal framework. We will start by expanding the nuclear radius in terms of spherical harmonics and develop the case of an axial deformation. After that, we will briefly discuss the more general case of triaxial, octupole, and parity breaking configurations.

1.3.1. Quadrupole deformation

Let us suppose to write variations of the nuclear radius R in terms of spherical harmonics, which form a complete basis as is well known

$$R(\theta, \phi) = R_0 \left[1 + \sum_{\lambda\mu} \alpha_{\lambda\mu} Y_{\lambda\mu}(\theta, \phi) \right], \quad (1.18)$$

where the moments $\alpha_{\lambda\mu}$, defined as

$$\alpha_{\lambda\mu} = \int Y_{\lambda\mu}^*(\theta, \phi) R(\theta, \phi) d\Omega \quad (1.19)$$

are considered small, in the sense that $|\alpha_{\lambda\mu}|^2 \ll |\alpha_{\lambda\mu}|$, so that the volume of the system

$$V = \iint_0^{R(\theta,\phi)} R^2 dR d\Omega = \frac{4}{3}\pi R_0^3 \left[1 + \frac{3}{4\pi} \sum_{\lambda\mu} |\alpha_{\lambda\mu}|^2 \right] \quad (1.20)$$

is conserved. Since Y_{00} is constant, including it in the expansion changes the total volume (1.20), we then set $\alpha_{00} = 0$. If we consider only frames of reference where the nucleus has a centre of mass fixed at the origin, we get vanishing $\alpha_{1\mu}$ coefficients.

Now, let us consider only $\alpha_{2\mu}$ coefficients and neglect higher order terms, so that the deformation is purely quadrupolar. Then the radius reads

$$R(\theta, \phi) = R_0 \left[1 + \sum_{\mu=-2}^2 \alpha_{2\mu} Y_{2\mu}(\theta, \phi) \right]. \quad (1.21)$$

If we assume to be in the reference frame in which the inertia tensor, proportional to the coefficients $\alpha_{2\mu}$, is diagonal, which is called intrinsic frame, then the sum

$$\alpha_{21} Y_{21}^* + \alpha_{2-1} Y_{2-1}^*$$

vanishes. Since R is a real valued function, we have the relation

$$\alpha_{\lambda\mu} Y_{\lambda\mu} + \alpha_{\lambda-\mu} Y_{\lambda-\mu} = 2 \operatorname{Re}\{\alpha_{\lambda\mu} Y_{\lambda\mu}\}, \quad (1.22)$$

as a consequence, the resulting expansion reads

$$\begin{aligned} R(\theta, \phi) &= R_0 \left[1 + a_{20} Y_{20} + 2 \operatorname{Re}\{a_{22} Y_{22}\} \right] \\ &= R_0 \left[1 + \sqrt{\frac{5}{16\pi}} \left(a_{20}(3 \cos^2 \theta - 1) + 2a_{22}\sqrt{3} \sin^2 \theta (\cos^2 \phi - \sin^2 \phi) \right) \right]. \end{aligned} \quad (1.23)$$

If we perform the substitution

$$a_{20} = \beta \cos(\gamma) \quad (1.24)$$

$$a_{22} = \beta \sin(\gamma) \quad (1.25)$$

and express the variation of R along the Cartesian axes, we get

$$R_x - R_0 = \delta R_x = \sqrt{\frac{5}{4\pi}} \beta R_0 \cos \left(\gamma - \frac{2\pi}{3} \right), \quad (1.26)$$

$$R_y - R_0 = \delta R_y = \sqrt{\frac{5}{4\pi}} \beta R_0 \cos \left(\gamma + \frac{2\pi}{3} \right), \quad (1.27)$$

$$R_z - R_0 = \delta R_z = \sqrt{\frac{5}{4\pi}} \beta R_0 \cos \gamma. \quad (1.28)$$

Assuming the value of β to always be positive, in the case $\gamma = 0$, $\delta R_x = \delta R_y < \delta R_z$, meaning the nucleus is in a *prolate* configuration; while in the case of $\gamma = \pi/3$, $\delta R_x = \delta R_y > \delta R_z$, meaning the nucleus has an *oblate* shape. A general convention is to write β with a negative sign in the oblate case, and a positive sign in the prolate case. By using trigonometric identities, it is trivial to show that unique shapes are found only for $\gamma \in [0; \pi/3]$, if γ takes a value different from 0 or $\pi/3$, the shape is said to be triaxial, meaning $\delta R_z \neq \delta R_x \neq \delta R_y$, the nucleus has no more rotational symmetries and is only symmetric for reflections along the (x, y) , (x, z) and (y, z) planes, which also induces parity symmetry.

1.3.2. Nilsson model

To understand the effect on single-particle motion of a deformed potential, we can consider the case of an axially deformed harmonic oscillator potential, for which $\omega_z \neq \omega_x = \omega_y = \omega_{\perp}$, meaning the oscillator frequency takes on a different value on the z axis than in the x and y axes.

To treat the deformation perturbatively, we can assume that the various frequencies deviate from the unperturbed $\hbar\omega_0 = 41/A^{1/3}$ MeV, in which case they may read

$$\omega_z = \omega_0 - \frac{2}{3}\varepsilon, \quad (1.29)$$

$$\omega_{\perp} = \omega_0 + \frac{1}{3}\varepsilon, \quad (1.30)$$

this definition of the frequencies satisfies the conservation of volume, at lowest order in ε , assumed to hold for

$$\omega_0^3 = \omega_z \omega_{\perp}^2. \quad (1.31)$$

We can thus write the single-particle Hamiltonian in the deformed potential as

$$H = H_0 + \varepsilon H_1,$$

$$H_0 = -\frac{\hbar^2}{2m} \nabla^2 + \frac{1}{2} m \omega_0^2 r^2, \quad (1.32)$$

$$\varepsilon H_1 = \frac{1}{3} \omega_0^2 \varepsilon (x^2 + y^2 - 2z^2) = -\frac{1}{3} \sqrt{\frac{16\pi}{5}} m \omega_0^2 \varepsilon r^2 Y_{20}. \quad (1.33)$$

H_0 is the usual spherical harmonic potential, for which the eigenfunctions, expressed through the usual quantum numbers $|nljm_j\rangle$ are known. Assuming ε to be small, we can evaluate the first order correction of H_1 to the system, which reads

$$\begin{aligned} \Delta E &= \langle nljm_j | \varepsilon H_1 | nljm_j \rangle, \\ &= -\frac{1}{3} \sqrt{\frac{16\pi}{5}} \varepsilon m \omega_0^2 \int r^2 u_{nl}(r) \langle jm_j | Y_{20} | jm_j \rangle dr, \\ &= \frac{\varepsilon}{6} m \omega_0^2 \int r^2 u_{nl}(r) \frac{3m_j^2 - j(j+1)}{j(j+1)} dr. \end{aligned} \quad (1.34)$$

Thus in the limit of large j , states with the maximum total angular momentum projection m_j are shifted upwards, while states with the minimum m_j are shifted downwards; moreover, eigenstates with $\pm m_j$ are degenerate, as expected by the reflection symmetry of the Hamiltonian if the z axis is inverted.

Adding further empirical terms to reproduce experimental data, and the spin-orbit coupling, results in the formulation of the Nilsson model [26]. In Figure 1.5, a graphical representation of the energy levels in the Nilsson model is shown [27].

Deformed Woods–Saxon

Recent studies of deformed nuclei have been carried out using empirical potentials such as deformed Woods–Saxon potentials [28, 29]. In these models, the nuclear shape is expanded as

$$R(\theta) = R_0 \left[1 + \sum_{\lambda}^L \beta_{\lambda} Y_{\lambda 0} \right], \quad (1.35)$$

so that the solution is axially symmetric and the problem is reduced to just the (r, θ) coordinates, in which we can write the potential as

$$U_{\text{WS}}(r, \theta) = -\frac{U_0(A, N)}{1 + e^{\frac{r-R(\theta)}{a}}}. \quad (1.36)$$

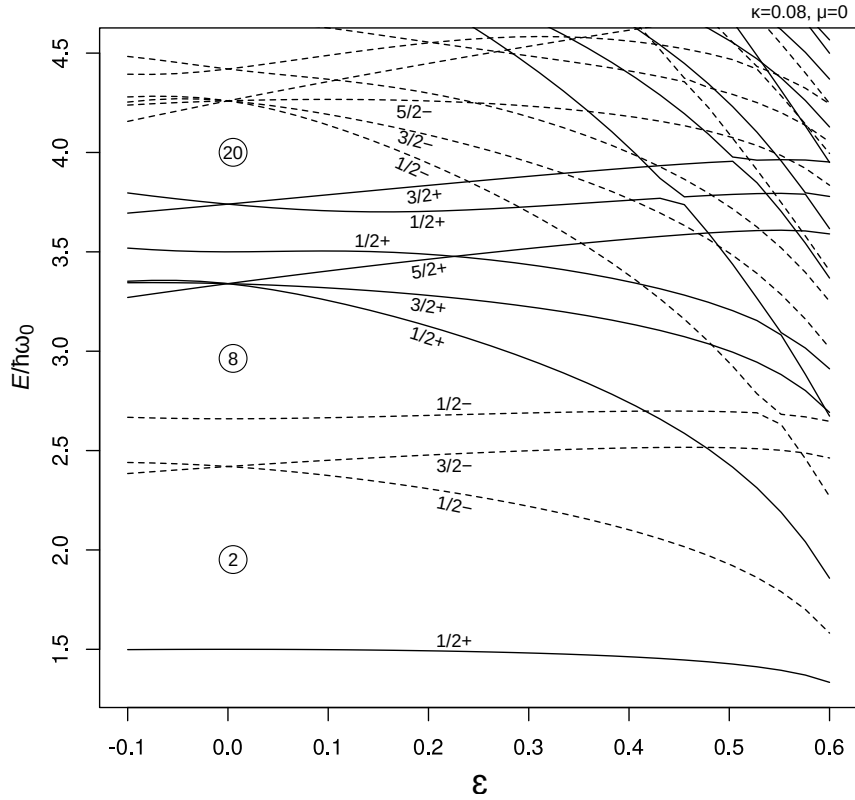


Figura 1.5: Nilsson model single-particle energy levels trends, as a function of ε . Figure taken from [27].

1.3.3. Octupole deformations and parity breaking

While quadrupole deformations concern nuclei across the whole chart, octupole deformations are much less common so far. The evidence for such deformations in even-even nuclei is mainly provided by the existence of rotational bands $I = 1^-, 3^-, \dots$ [30] and the enhanced electric octupole transition probability $B(E3)$, which reads

$$B(E3; 3^- \rightarrow 0^+) = \frac{1}{2J_i + 1} |\langle 0^+ | e r^3 \hat{Q}_3 | 3^- \rangle|^2, \quad (1.37)$$

where J_i is the initial total angular momentum of the nucleus and \hat{Q}_3 is the octupole operator defined as

$$\hat{Q}_3 = r^3 Y_{30}(\hat{r}). \quad (1.38)$$

Evidence of such bands was initially found in neutron-rich Barium isotopes, ^{144}Ba [31] and ^{146}Ba [32], and a while later in Radium isotopes [33] and other heavy nuclei as well [34].

Expansions on spherical harmonics, under the parity operation $\mathcal{P} : \mathbf{r} \mapsto -\mathbf{r}$, transform as

$$\mathcal{P}\alpha_{\lambda\mu} = (-1)^\lambda \alpha_{\lambda\mu}, \quad (1.39)$$

hence a nuclear octupole deformation, whose order $\lambda = 3$, would break the parity symmetry of the mean-field. In Figure 1.6 a graphical representation of the spherical harmonics for $\lambda = 3$ and $\mu = 0, 2$ is shown.



Figura 1.6: Graphical representation of possible octupole deformations. On the left, the axially symmetric Y_{30} deformation, on the right, the non-axial octupole deformation Y_{32} .

1.4. Nuclear fission

Nuclear fission is the process by which a nucleus splits into two – sometimes three – nuclei, whether spontaneously or when induced by a reaction. The physics that governs nuclear fission is that of a many-body, large-amplitude collective mode that gradually elongates the nuclear shape until the so-called *fission barrier* is surmounted and the energetically favoured path leads the nucleus to fragment. In Figure 1.7, a graphical representation of the fission path and corresponding barrier is shown.

Although the basic idea of a nucleus dividing into two pieces may appear simple, the underlying dynamics is remarkably rich and involves several stages. Historically, the first theoretical interpretation of fission was given by Bohr and Wheeler in 1939 [35], who formulated the liquid-drop model description and introduced the concept of the fission barrier, determined by the competition between Coulomb repulsion and surface

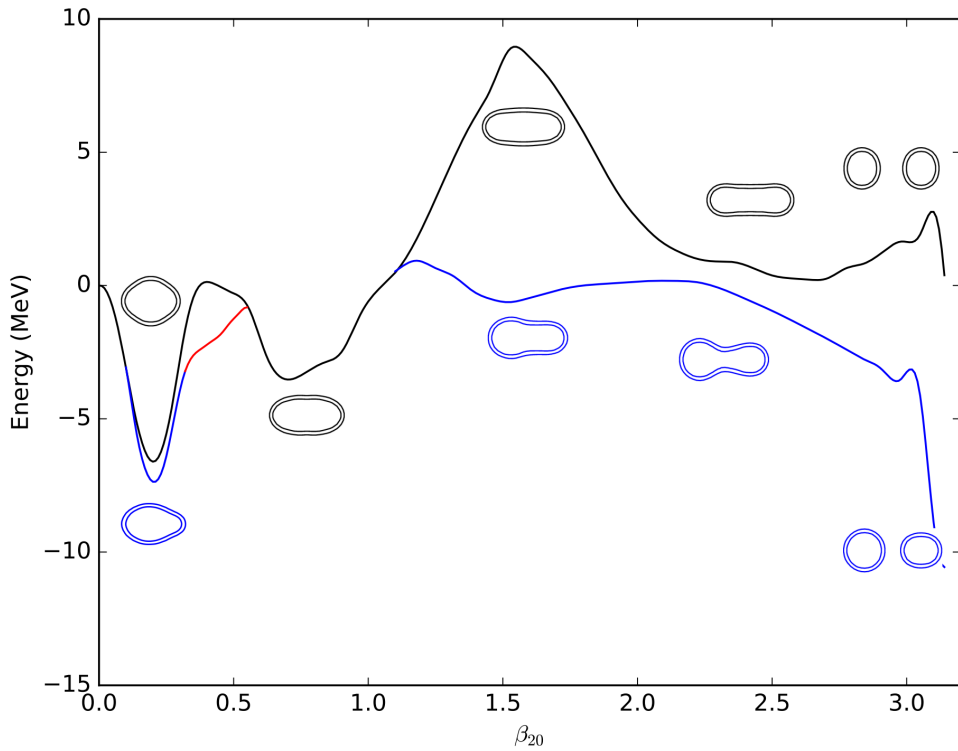


Figura 1.7: Fission path of ^{226}Ra , blue lines indicate axial octupole configurations, black lines indicate axial quadrupole and parity conserving configurations, red lines indicate triaxial, parity conserving configurations. Figure taken from [11].

tension. Their framework already suggested that nuclei may experience intermediate configurations, multiple saddle points, and shape isomerism along the fission path.

Subsequent developments incorporated more detailed descriptions of the collective degrees of freedom and the role of shell effects, leading to the recognition that the fission landscape is often characterised by multiple barriers, intermediate minima, and highly deformed transition states [36, 37]. Modern microscopic approaches, based on energy-density functionals, have further clarified that fission dynamics involves a sequence of slow, dissipative shape evolutions, interspersed with possible gamma-decay pathways, and culminating in the formation of two (or more) pre-fragments connected by a narrowing neck. As the system evolves beyond the outer saddle, exotic spatial configurations appear, and the fragments themselves may exhibit deformation or even reflection asymmetry before scission. A visual representation of the overall fission process is shown in Figure 1.8.

Spontaneous fission model

It should be obvious that a formal treatment of deformations and collective modes is necessary to give a theoretical description of fission reactions. We can derive a simple

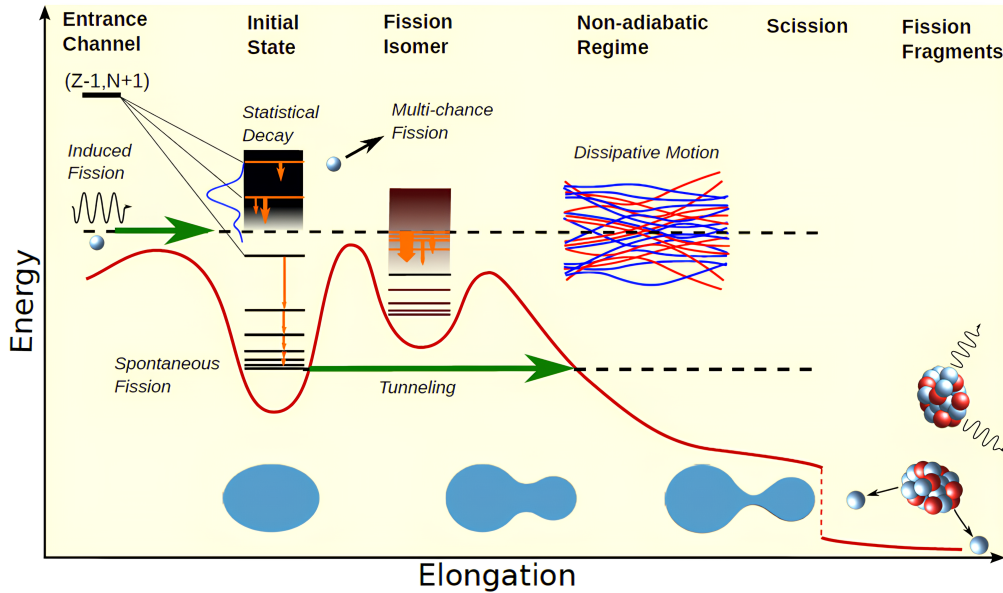


Figura 1.8: Visual representation of the fission process. Figure taken from [38].

spontaneous fission model by studying the effect of an axial quadrupole deformation on the semiempirical mass formula 1.3.

Let us assume that the nuclear radius may be expanded, as previously done in Section 1.3, as

$$R = R_0[1 + \alpha_{20}Y_{20}]. \quad (1.40)$$

Assuming the nuclear volume is conserved across the fission path, the volume energy will not change. As for the surface energy, its variation can be expressed at the lowest order in α_{20} as

$$\Delta E_{\text{surf}} = E_{\text{surf}} - E_{0,\text{surf}} = E_{0,\text{surf}} \frac{2}{5} \alpha_{20}^2. \quad (1.41)$$

Regarding the Coulomb energy, the variation is given by

$$\Delta E_{\text{coul}} = E_{\text{coul}} - E_{0,\text{coul}} = -E_{0,\text{coul}} \frac{1}{5} \alpha_{20}. \quad (1.42)$$

Since the neutron and proton numbers does not change, the surface and Coulomb energies are the only contributions to the total energy difference. We can write

$$\Delta E = \frac{2}{5} \alpha_{20}^2 a_s A^{2/3} - \frac{1}{5} \alpha_{20}^2 a_c Z^2 A^{-1/3}, \quad (1.43)$$

if we set Equation (1.43) to zero, we get, other than the undeformed solution for $\alpha_{20} = 0$,

$$\frac{Z^2}{A} = \frac{2a_s}{a_c}, \quad (1.44)$$

where the ratio $2a_s/a_c$ amounts to ≈ 50 in typical parametrisations of the SEMF. Equation (1.43), shows that for values of the so called *fissility parameter* Z^2/A larger than 50, the energy change becomes negative, favouring a configuration in which the nucleus fragments due to the spontaneous fission.

Pairing correlations in fission

Pairing correlations are fundamental to quantitatively describe the fission process and the difference between fissile and fissionable materials. As a general example, applicable to heavy nuclei in the actinide region, we can examine the difference between ^{235}U and ^{238}U in their fission induced by a thermal neutron. The fission barrier height for ^{239}U is ≈ 5.5 MeV, while for ^{236}U it is ≈ 5.3 MeV. Although the difference is small, when ^{235}U captures a thermal neutron the latter is able to fission while the former is not when ^{238}U captures a thermal neutron. This is due to the stronger pairing correlations in even nuclei than in odd nuclei, as the compound nucleus binding energy is higher when the neutron and/or proton number is even, favouring fission.

The presence of pairing correlations is also fundamental when quantitatively describing the evolution from the ground state to the scission. Pairing correlations allow the nuclear density to take on many different additional configurations, as the fission barrier is traversed in a superposition of these shapes, as explained more in depth in Section 3.3, the fragmentation happens more easily [39].

2 | State of the art, objectives and methods

2.1. State of the art and motivation

The need to account for nuclear deformations has been already highlighted as a central theme in Chapter 1, particularly in the context of heavy nuclei and of the complex fission dynamics discussed in Section 1.4. Without allowing for deformation, several key properties of nuclear systems, such as the rotational bands in the excitation spectrum since spherical nuclei cannot rotate, cannot be captured. Limiting the description to only a subset of shapes, such as axially symmetric configurations, often proves to be inadequate. This is evident in the case of fission dynamics, where the evolution stages happen through very deformed and exotic configurations, explored over relatively long time scales.

The central issue in nuclear structure theory is that the Hamiltonian is not known exactly and must be approximated. At the same time, the problem is inherently a quantum many-body one, which remains computationally demanding, requiring approximations to make calculations tractable. Symmetry assumptions such as spherical or axial symmetry have therefore been widely used in numerical implementations to simplify the calculations and reduce the computational cost. However, these constraints become insufficient in situations where deformation is a defining aspect of the system.

With the increasing availability of computational power and the development of modern numerical techniques, the field is now in a position to move beyond these restrictive assumptions. This motivates the development of new codes capable of treating the many-body problem without imposed symmetries, allowing the full range of nuclear deformations to emerge naturally from the underlying theory.

2.2. State of the Art

The approaches to the nuclear many-body problem can be divided into three families: shell model, ab initio, and Density Functional Theory.

Shell model In the interacting shell model, one assumes that a basis is constituted by nucleons in single-particle orbitals. While some orbitals are *frozen*, there is a space called *valence space* in which one includes all possible configurations with nucleons arbitrarily put in the valence orbitals. The nuclear Hamiltonian is diagonalized in this configuration space. This model is very successful for spectroscopy but also computationally very demanding. Often, the predictive power is strongly dependent on the specific effective Hamiltonian that is assumed.

Ab initio One may be inclined towards studying nuclei starting from the fundamental interaction which binds them, the strong force. This would be done starting from the QCD Lagrangian, however, two problems arise. First, nucleons are bound states of quarks and gluons and what binds the nucleus together is the residual interaction arising from these bound systems. Second, the QCD coupling is large at the energy scale $\Lambda_\chi \approx 0.5 - 1.0$ GeV of nucleons and heavy mesons and as such cannot be treated perturbatively. This is at variance with the higher energy scales like 100 – 1000 GeV where QCD is perturbative.

The solution to this problem is the use of effective chiral Lagrangians, equivalent to the QCD one at low energy scales. The interactions among the nucleons arise from the Feynman diagrams between two, three, or more nucleons, which must be hierarchically ordered, according to some perturbative parameter, usually denoted by $(Q/\Lambda_\chi)^\nu$, where Q is the typical nucleon momentum. The power of ν at which the expansion stops determines the order of the potential that is calculated and used.

These methods are in principle exact, but require nevertheless a series of approximations to make calculations tractable; moreover, their applicability is currently limited to spherical and light deformed nuclei.

Density Functional Theory The issues brought forth by the shell model and the ab initio approaches may be addressed by using an *effective* interaction among nucleons that is not derived from exact principles but reliably reproduces experimental data. This was done starting from the 1970s, by minimising the energy functional $\langle \Psi | \hat{H}_{\text{eff}} | \Psi \rangle$, where \hat{H}_{eff} is a properly designed effective Hamiltonian and Ψ is a Slater determinant.

It was realised early on that the only way to obtain realistic results from this approach was to use density dependent forces, which somewhat account for the important many-body effects. The historical development of this realization has been to first use the Hartree–Fock expectation value of an effective interaction as a starting point for the design of an Energy Density Functional (EDF), which can be used to do nuclear structure calculations using Density Functional Theory. Later, it has been customary to directly write an EDF.

In particular, the minimisation of these EDFs has been done using two numerical approaches: (a) *basis expansion methods*, which represent single-particle states on truncated bases, mainly harmonic oscillator bases, and (b) *coordinate-space (mesh) methods*, which discretise space directly by using a mesh. In the following sections, we review these two classes of methods and motivate the need for more flexible and computationally efficient unconstrained solvers.

2.2.1. Basis expansion methods

Basis expansion approaches are among the most widely used techniques for solving the HF and HFB equations. In these methods, single-particle wavefunctions are expanded on a finite HO basis, chosen for its flexibility and easiness of use, together with the qualitative similarity to the mean-field potential of bound nuclei, as explained in Section 1.1. Codes such as `HFBTHO`, also used in this work for benchmarking our implementation in Section 6.2.1, are based on this framework.

The HO basis, although efficient, introduces inherent limitations. First, weakly bound and continuum-like states, crucial for nuclei near the drip lines, are poorly represented because their asymptotic behaviour differs fundamentally from that of HO functions. Whereas HO states decay as e^{-ar^2} , quasi-bound states decay as $e^{-\kappa r}$, leading to slow convergence and difficulties in describing haloes, neutron skins, and quasi-resonant states [40, 41]. Second, large deformations in heavy nuclei may require many HO shells to reproduce the stretched spatial geometry, significantly increasing the computational cost. The computational complexity grows rapidly with the maximum number of oscillator shells used in the calculation, resulting in demanding memory and CPU requirements for strongly deformed configurations [9].

In summary, despite their efficiency for near-spherical and moderately deformed nuclei, basis-expansion methods become inadequate for describing nuclei near drip lines, far from stability and largely deformed.

2.2.2. Symmetry-Restricted mesh methods

A second major class of HF/HFB solvers uses a spatial mesh. Historically, fully unconstrained three-dimensional meshes were computationally prohibitive, which motivated the introduction of *symmetry constraints* to reduce the dimensionality of the problem. By enforcing specific spatial symmetries, the number of degrees of freedom is greatly reduced, making coordinate-space calculations tractable on available hardware.

The most common choices are spherical and axial symmetry. Spherical HF/HFB solvers [7, 42] reduce the equations to a radial problem, achieving excellent computational efficiency and precision for the structure of spherical or near-spherical nuclei. Axially symmetric solvers [43] generalise this approach to two dimensions, allowing axial deformations while still benefitting from significant computational cost reductions.

However, the limitations of symmetry-restricted approaches are inherent to the constraints themselves, as they forbid the emergence of intrinsic shapes such as triaxial or more general octupole-deformed configurations.

2.2.3. Unconstrained coordinate-space (mesh) methods

To overcome the limitations of basis truncation and symmetry constraints, modern HF / HFB solvers have increasingly adopted coordinate-space discretizations, typically based on three-dimensional Cartesian meshes. Notable examples include MOCCA [11], Sky3D [13], and HFBFFT [44]. These codes solve the HF or HFB equations directly in coordinate space, allowing arbitrary deformations and spontaneous symmetry breaking to emerge naturally.

However, coordinate-space solvers come with their own challenges. High spatial resolution is required to accomodate sufficient numerical accuracy, leading to large three-dimensional grids, thus substantial computational cost. Even with modern resources, fully unconstrained calculations remain computationally intensive, and additional assumptions such as plane reflection symmetry are often introduced to reduce the domain size [11, 14]. Thus, while mesh-based solvers offer maximal flexibility, their computational demands motivate the search for more efficient numerical approaches.

2.2.4. Towards more efficient unconstrained methods

The limitations discussed above highlight the need for methods that combine the flexibility of coordinate-space solvers with improved computational efficiency. In this thesis, we investigate such an approach through the use of the *Generalised Conjugate Gradient* (GCG) method, presented in detail in section 4.2.3. In the HF and energy-density-functional fra-

meworks, the core of the many-body problem reduces to solving a set of single-particle Schrödinger or Kohn–Sham eigenvalue equations, coupled self-consistently through the mean-field. These equations must be solved repeatedly during the iterative HF/HFB cycle, and their efficient solution dominates the overall computational cost.

As shown in the present work, applying GCG to the HF single-particle problem provides a promising route towards efficient, symmetry-unrestricted many-body calculations while mitigating the main bottlenecks of fully coordinate-mesh methods.

2.3. Objectives

The aim of this work is to develop a new implementation of the Hartree–Fock method on an unconstrained 3D mesh, by the use of the Generalised Conjugate Gradient method. The goals addressed by this work are the following:

- demonstrate the feasibility of the Generalised Conjugate Gradient for the solution of large-scale eigenvalue problems;
- solve the self-consistent Hartree–Fock equations on an unconstrained 3D mesh;
- verify the numerical accuracy of the new implementation, first against existing spherical codes;
- second against well-established deformed codes; and
- attempt to produce novel results, and establish the advancement brought to the field by this work.

2.4. Methods

The methods used in this thesis can be grouped into two main components: the formulation of the Energy Density Functional and the solution of the resulting self-consistent equations.

Skyrme Energy Functional The many-body nuclear problem is approached within the Hartree–Fock framework, described in section 3.1. As discussed in Chapter 1, a pure HF treatment is not sufficient for a quantitative description of nuclear structure, and a more general Energy Density Functional (EDF) formulation must be adopted. In this work, we employ the Skyrme EDF, whose construction and resulting mean-field equations

are developed in section 3.4. This provides the self-consistent single-particle Hamiltonian that forms the basis for the numerical treatment.

Finite Differences and Generalised Conjugate Gradient Once the equations to be solved have been derived, their numerical solution requires both a spatial discretization scheme and an efficient solver for the large-scale eigenvalue problem that arises at each iteration of the self-consistent procedure. Chapter 4 details the methods adopted in this work, starting with the finite-difference discretization of derivatives in section 4.1. The resulting discretised eigenvalue problem is then treated using the GCG method to extract the relevant low-lying eigenstates, as described in section 4.2.3. Section 4.3 discusses implementation-specific aspects of the code, including convergence criteria, mixing strategies, and the choice of parameters required to ensure stable and efficient minimisation of the energy functional.

3 | Energy functional

3.1. Hartree–Fock theory

While a phenomenological description of some nuclear structure properties can be carried out using the liquid drop model or empirical mean-field potentials like Woods–Saxon or Nilsson, as we have seen in Section 1.1, this is not sufficient to accurately reproduce all experimental ground state observables, systematically throughout the chart of nuclei, in an accurate manner.

A more rigorous approach needs to take into account the fact that the mean-field the nucleons interact with, is generated by the nucleons themselves. Starting from the many-body Hamiltonian of the system, we will be able to extract a single particle Hamiltonian, including an effective mean-field potential generated by the effective microscopic force, through the use of the Hartree–Fock method.

We start by writing the many-body Hamiltonian of the system, which is a collection of A interacting fermions, given by

$$\hat{H} = \hat{T} + \hat{V} = \sum_i -\frac{\hbar^2}{2m} \nabla_i^2 + \sum_{i < j} v_{ij}^{(2)} + \sum_{i < j < k} v_{ijk}^{(3)} + \dots \quad (3.1)$$

The corresponding Schrödinger equation reads

$$\hat{H}\Psi = E\Psi. \quad (3.2)$$

3.1.1. Variational principle

Since \hat{H} is a many body operator, finding its eigenstates would be a rather challenging task. To our aid, comes the variational principle, from which we can show that Equation (3.2) is equivalent to

$$\delta E[\Psi] = \delta \frac{\langle \Psi | E | \Psi \rangle}{\langle \Psi | \Psi \rangle} = 0. \quad (3.3)$$

The variation (3.3) can be obtained from an arbitrary variation of Ψ , which can be done independently on $\langle \Psi |$ and $|\Psi \rangle$, since Ψ is complex, yielding

$$\langle \delta\Psi | \hat{H} - E | \Psi \rangle + \langle \Psi | \hat{H} - E | \delta\Psi \rangle = 0 \quad (3.4)$$

since the variation is arbitrary, we can multiply by a phase factor $|\delta\Psi\rangle \mapsto i|\delta\Psi\rangle$ and get

$$-i\langle \delta\Psi | \hat{H} - E | \Psi \rangle + i\langle \Psi | \hat{H} - E | \delta\Psi \rangle = 0. \quad (3.5)$$

Combining equations (3.4) and (3.5), we get

$$\langle \delta\Psi | \hat{H} - E | \Psi \rangle = 0. \quad (3.6)$$

Again, since the variation is arbitrary, Equation (3.6) satisfies Equation (3.2).

Ground state

Since we always restrict ourselves to a certain subspace of the full Hilbert space, we can only find an approximate solution to the eigenvalue problem. Expanding this solution on the complete set of exact eigenstates of \hat{H} , we have

$$|\Psi\rangle = \sum_n a_n |\Psi_n\rangle \quad (3.7)$$

the total energy amounts to

$$E[\Psi] = \frac{\sum_{nn'} \langle a_{n'} \Psi_{n'} | \hat{H} | a_n \Psi_n \rangle}{\sum_{nn'} \langle a_{n'} \Psi_{n'} | a_n \Psi_n \rangle} = \frac{\sum_n E_n |a_n|^2}{\sum_n |a_n|^2} \geq \frac{\sum_n E_0 |a_n|^2}{\sum_n |a_n|^2} \geq E_0, \quad (3.8)$$

where E_0 is the ground state energy of the system. The orthonormality of the Hamiltonian eigenfunctions $\langle \Psi_{n'} | \Psi_n \rangle = \delta_{nn'}$ has been used. Equation (3.8) tells us that the minimum of the functional $E[\Psi]$ in any variational subspace we are considering is bound from below by the true ground state energy.

3.1.2. Hartree–Fock equations

The Hartree–Fock method is the application of the variational principle (3.6) to a system of independent particles, whose wavefunction takes the form of a Slater determinant,

which reads

$$\Psi = \frac{1}{\sqrt{A!}} \sum_{\{p\}} (-1)^p \varphi_{p(1)}(\mathbf{r}_1) \dots \varphi_{p(A)}(\mathbf{r}_A), \quad (3.9)$$

and where φ_i are the single-particle orthonormal states, which serve the role of variational parameters in Hartree–Fock. The Slater determinant sums over all possible permutations of the A fermions on the single particle states, with a $-$ sign according to the parity of the permutation. The Slater determinant satisfies the permutation symmetry of fermions, so that the Pauli exclusion principle is not violated.

To ensure the orthonormality of the single-particle states, we need to add a Lagrange multiplier to the variation (3.6) of E , which ends up reading

$$\delta \left(E[\Psi] - \sum_i \lambda_i \int \varphi_i^* \varphi_i d\mathbf{r} \right) = 0. \quad (3.10)$$

The total energy of the system is given by

$$E[\Psi] = \langle \Psi | \hat{T} + \hat{V} | \Psi \rangle = \langle \Psi | \hat{T} | \Psi \rangle + \langle \Psi | \hat{V} | \Psi \rangle, \quad (3.11)$$

which can be expressed through the single-particle states $\{\varphi_i\}$, yielding

$$\langle \Psi | \hat{T} | \Psi \rangle = \sum_i^A -\frac{\hbar^2}{2m} \int \varphi_i^*(\mathbf{r}) \nabla^2 \varphi_i(\mathbf{r}) d\mathbf{r} = \sum_i \langle i | t | i \rangle \quad (3.12)$$

$$\begin{aligned} \langle \Psi | \hat{V} | \Psi \rangle &= \frac{1}{2} \sum_{ij} \int \varphi_i^*(\mathbf{r}) \varphi_j^*(\mathbf{r}') v_{ij}(\mathbf{r}, \mathbf{r}') \varphi_i(\mathbf{r}) \varphi_j(\mathbf{r}') d\mathbf{r} d\mathbf{r}' \\ &\quad - \frac{1}{2} \sum_{ij} \int \varphi_i^*(\mathbf{r}) \varphi_j^*(\mathbf{r}') v_{ij}(\mathbf{r}, \mathbf{r}') \varphi_i(\mathbf{r}') \varphi_j(\mathbf{r}) d\mathbf{r} d\mathbf{r}' \\ &= \frac{1}{2} \sum_{ij} \langle ij | \bar{v} | ij \rangle. \end{aligned} \quad (3.13)$$

If we use $\varphi_i^*(\mathbf{r})$ as the quantity to be varied in Equation (3.10), we get the *Hartree–Fock equations*

$$\begin{aligned} &- \frac{\hbar^2}{2m} \nabla^2 \varphi_i \\ &+ \frac{1}{2} \sum_j^A \int \varphi_j^*(\mathbf{r}') v_{ij}(\mathbf{r}, \mathbf{r}') \varphi_j(\mathbf{r}') \varphi_i(\mathbf{r}) d\mathbf{r}' \end{aligned} \quad (3.14)$$

$$- \frac{1}{2} \sum_j^A \int \varphi_j^*(\mathbf{r}') v_{ij}(\mathbf{r}, \mathbf{r}') \varphi_j(\mathbf{r}) \varphi_i(\mathbf{r}') d\mathbf{r}' = \varepsilon_i \varphi_i \quad (3.15)$$

which can be written compactly as

$$h\varphi_i = \varepsilon_i \varphi_i, \quad (3.16)$$

where h is the single-particle Hamiltonian. Here the Lagrange multipliers λ_i have been replaced by ε_i , since they can be interpreted as the energy of the single-particle states.

The first interaction term (3.14), called Hartree term, arises from considering independent particles, each of one interacting with the mean-field produced by the others, and is also routinely found in classical physics. The second one in (3.15), called Fock term, or exchange term, takes the form of an integral operator and is present when considering quantum mechanical indistinguishable particles. For what concerns the solution of Equation (3.16), the Fock term complicates the problem, as it implies solving an integro-differential equation. This can be avoided using zero-range forces like the Skyrme one [45], which is used in the present work, since it renders the exchange term as a local one.

Even if the interaction terms are local, the equation is still highly non-linear, since the mean-field potential will be a function of the eigenfunctions themselves. The consequence is that the solution needs to be found *self-consistently*, that is, by solving for the set of eigenfunctions $\{\varphi_i\}$, using them to build the new mean-field, and solving again, repeating the process until convergence.

3.1.3. Symmetries in Hartree–Fock

Since the objective of this work is to solve the Hartree–Fock equations without spatial symmetry assumptions, it is useful to first understand how symmetries propagate along the self-consistent calculation. We start by defining the creation and annihilation operators of the single particle hamiltonian eigenstates, a_i^\dagger, a_i , which abide the usual anticommutation relations of fermions

$$\{a_i, a_j^\dagger\} = \delta_{ij}. \quad (3.17)$$

If we expand on a different, orthonormal complete basis $\{\chi_l\}$, we can write the corresponding creation and annihilation operators c_l^\dagger, c_l as

$$\begin{aligned} \varphi_k &= \sum_l D_{lk} \chi_l, \\ a_k^\dagger &= \sum_l D_{lk} c_l^\dagger, \\ a_k &= \sum_l D_{lk}^\dagger c_l. \end{aligned}$$

Since orthonormality is guaranteed for both sets, taking $\langle \varphi_j | \varphi_k \rangle$ yields

$$\delta_{jk} = \langle \varphi_j | \varphi_k \rangle = \sum_{ll'} D_{l'j}^\dagger D_{lk} \langle \chi_l | \chi'_{l'} \rangle \implies DD^\dagger = 1, \quad (3.18)$$

meaning that D is a unitary transformation. We can define the density matrix as

$$\rho_{ll'} = \langle \Psi | c_{l'}^\dagger c_l | \Psi \rangle, \quad (3.19)$$

whose trace is equal to the particle number A , as per Equation (3.20)

$$\text{Tr } \rho = \sum_{ll} \langle \Psi | c_l^\dagger c_l | \Psi \rangle = \sum_{ll} \langle \Psi | a_l^\dagger a_l | \Psi \rangle = \sum_{ll}^A \langle \Psi | \Psi \rangle = A. \quad (3.20)$$

Writing the many body hamiltonian (3.2) in the arbitrary basis of the second quantization operators c_l^\dagger, c_l , we get

$$\hat{H} = \sum_{l_1 l_2} t_{l_1 l_2} c_{l_1}^\dagger c_{l_2} + \frac{1}{4} \sum_{l_1 l_2 l_3 l_4} \bar{v}_{l_1 l_2 l_3 l_4} c_{l_1}^\dagger c_{l_2}^\dagger c_{l_3} c_{l_4} \quad (3.21)$$

where $t_{l_1 l_2}$ and $\bar{v}_{l_1 l_2 l_3 l_4}$ are defined as

$$t_{l_1 l_2} = \langle - | c_{l_1} c_{l_2} t c_{l_1}^\dagger c_{l_2}^\dagger | - \rangle = \langle l_1 l_2 | t | l_1 l_2 \rangle \quad (3.22)$$

$$\bar{v}_{l_1 l_2 l_3 l_4} = \langle l_1 l_2 l_3 l_4 | v | l_1 l_2 l_3 l_4 \rangle - \langle l_1 l_2 l_4 l_3 | v | l_1 l_2 l_4 l_3 \rangle. \quad (3.23)$$

The minimisation (3.10) can be restated as the variation of $\langle \Psi | \hat{H} | \Psi \rangle$, with respect to the density matrix $\rho_{ll'}$, which yields

$$h_{ll'} = \frac{\partial E[\rho]}{\partial \rho_{ll'}} = t + \sum_{kk'} \bar{v}_{lk'lk} \rho_{kk'} = t + \Gamma_{ll'} \quad (3.24)$$

where $\Gamma_{ll'}$ is the mean-field potential in the arbitrary basis. Being h diagonal in the Hartree–Fock basis, the self-consistent solution is the one for which

$$[h, \rho] = 0 \quad (3.25)$$

holds.

Symmetry propagation

When solving the Hartree–Fock equations, we start from an initial guess with a density matrix $\rho^{(0)}$. Let us suppose that this initial guess is symmetric under the action of a unitary many-body symmetry operator S , meaning

$$S\rho^{(0)}S^\dagger = \rho^{(0)}, \quad (3.26)$$

where S commutes with the many-body Hamiltonian

$$[S, \hat{H}] = 0. \quad (3.27)$$

It can be shown [17] that

$$S\Gamma[\rho]S^\dagger = \Gamma[S\rho S^\dagger], \quad (3.28)$$

the single particle Hamiltonian h will then display the same property

$$Sh[\rho]S^\dagger = h[S\rho S^\dagger]. \quad (3.29)$$

If the equality (3.26) holds, we get

$$Sh[\rho^{(0)}]S^\dagger = h[S\rho^{(0)}S^\dagger] = h[\rho^{(0)}], \quad (3.30)$$

meaning that h will be symmetric under the action of S , as well as the next iteration's density matrix $\rho^{(1)}$. The symmetry S gets propagated self-consistently until the minimum is found.

This has profound numerical implications, since the minimum energy configuration of a deformed nucleus can be reached only from a starting guesses with the same broken symmetries. It can be the case that numerical noise allows to explore the full energy surface, but if one has to take into consideration the numerical cost of a bad guess, then it is still advantageous to start from a correct one in terms of symmetries.

3.1.4. Density Functional Theory

It shall be evident shortly, in Section 3.4, that a more general approach to microscopic models has to be taken in order to give a satisfactory description of nuclei and nuclear matter. The method that we will briefly outline here is called Density Functional Theory (DFT).

DFT was introduced by P Hohenberg and W Kohn in 1964 [46], by proving two theorems. The **first** Hohenberg-Kohn (HK) theorem states that the energy of a fermion system, subject to an external potential V_{ext} , can be expressed solely as a functional of the particle density ρ of the system

$$E[\rho] = F[\rho] + \int V_{\text{ext}}\rho(\mathbf{r})d\mathbf{r}, \quad (3.31)$$

where $F[\rho]$ is a universal functional given by the type of fermions considered, while V_{ext} term is the external potential to which the system is subject to; when treating atomic nuclei, the potential is generated by the nucleons themselves, so this term will be omitted in the following. The **second** HK theorem states that the ground state of the system is found by minimising the functional (3.31) with respect to ρ .

HK theorems are fundamental but not constructive [5], since they do not provide a form for the functional F , which is intrinsic to the physics of the fermions at hand. A pragmatic approach to using DFT was outlined by Kohn and Sham in 1965 [47]. They proposed expressing the system as a set of non-interacting particles occupying auxiliary orbitals φ_i , which yield the particle density

$$\rho(\mathbf{r}) = \sum_i |\varphi_i(\mathbf{r})|^2 \quad (3.32)$$

and an energy functional of the form

$$E[\rho] = T[\rho] + E_H[\rho] + E_{\text{xc}}[\rho]. \quad (3.33)$$

Where T is the kinetic energy, which reads

$$T[\rho] = -\frac{\hbar^2}{2m} \sum_i \varphi_i^*(\mathbf{r}) \nabla^2 \varphi_i(\mathbf{r}) \quad (3.34)$$

and E_H is the classical Hartree term, which in an electronic system may read

$$E_H[\rho] = \iint \frac{\rho(\mathbf{r})\rho(\mathbf{r}')}{|\mathbf{r} - \mathbf{r}'|} d\mathbf{r} d\mathbf{r}', \quad (3.35)$$

while E_{xc} is an unknown exchange term. In electronic systems, the Hartree term is known (3.14) and the exchange term can be approximated thanks to the compensation of its error with the one of particles correlation neglection [48]. In nuclear physics, things are more complicated, since both terms are unknown; historically, effective interactions in HF have been used to extract an effective Hamiltonian density from which an EDF can be

formulated, whenever a pure interaction is not sufficient to describe nuclear systems, as we shall see in Section 3.4.

3.2. Pairing in Hartree–Fock theory

In this section, we will discuss the two common approaches to include nuclear pairing in the HF theory. The aim of these few pages is to provide a brief overview of how the BCS equations are derived and understand the basics of the more general Hartree–Fock–Bogoliubov theory. The former method is the most widely implemented thanks to its low complexity [10, 42, 49], while the latter, more sophisticated and advanced, is the standard in modern codes [8, 12, 50]. We will touch on it so that the reader may appreciate in the numerical chapter the natural extension of this work to the more general Bogoliubov ansatz. The reader may refer to introductory textbooks on many-body theory, such as Ref. [17] for an in-depth treatment of nuclear pairing.

3.2.1. BCS theory

The BCS approximation, from Bardeen-Cooper-Schrieffer, is the same theory used to describe Cooper pairs in superconductors, applied to the nuclear case. The ansatz of BCS is that nucleons are paired in states whose total angular momentum is zero, so that the wavefunction of a pair is $|JM\rangle = |00\rangle$ and reads

$$|00\rangle = \sum_{m_j} \langle jm_j j - m_j | 00 \rangle |jm_j\rangle |j - m_j\rangle. \quad (3.36)$$

Introducing the time-reversal operator $\hat{\mathcal{T}} : t \mapsto -t$, it acts on $|jm_j\rangle$ as

$$\hat{\mathcal{T}} |jm_j\rangle = \widetilde{|jm_j\rangle} = (-1)^{j+m_j} |j - m_j\rangle, \quad (3.37)$$

and using this relation, Equation (3.36) becomes

$$|00\rangle = -\frac{1}{\sqrt{2j+1}} \sum_{m_j} |jm_j\rangle \widetilde{|jm_j\rangle}. \quad (3.38)$$

The BCS ansatz amounts to replacing the Slater determinant with a more general wavefunction where pairs partially occupy time-reversal states. The BCS wavefunction reads

$$|\text{BCS}\rangle = \prod_{k>0} (u_k + v_k a_k^\dagger a_k^\dagger) |-\rangle \quad (3.39)$$

where k is a shorthand notation for $|jm\rangle$, $\tilde{k} = -k$ denotes the time-reversal state of k , and v_k and u_k are variational parameters, we shall see shortly that v_k^2 is the probability of finding a particle in state k . The product runs over positive k only. The BCS wavefunction is the creation in the vacuum of quasi-particles made of time-reversal paired particles, instead of individual ones. The normalization condition on the BCS wavefunction reads

$$1 = \langle \text{BCS} | \text{BCS} \rangle = \prod_{k>0} \langle - | (u_k + v_k a_k a_{\tilde{k}})(u_k + v_k a_{\tilde{k}}^\dagger a_k^\dagger) | - \rangle = \prod_{k>0} (u_k^2 + v_k^2) = 1 \quad (3.40)$$

which implies, for every pair k , the normalization condition

$$u_k^2 + v_k^2 = 1. \quad (3.41)$$

Taking the expectation value of the particle number operator $\hat{N} = \sum_k a_k^\dagger a_k$ yields [15]

$$\langle \text{BCS} | \hat{N} | \text{BCS} \rangle = 2 \sum_{k>0} v_k^2, \quad (3.42)$$

where v_k^2 is the probability of finding a particle in state k , while the expectation value of the particle number dispersion reads

$$\langle \Delta \hat{N}^2 \rangle = \langle \hat{N}^2 \rangle - \langle \hat{N} \rangle^2 = 4 \sum_{k>0} v_k^2 u_k^2. \quad (3.43)$$

The consequence of this result is profound. The BCS ansatz does not assume a fixed number of particles, rather it has an expectation value that depends on how the parameters v_k^2 are set, and presents fluctuations around it.

We can now write the many body Hamiltonian of the system as in Equation (3.21)

$$\hat{H} = \sum_{k_1 k_2} t_{k_1 k_2} a_{k_1}^\dagger a_{k_2} + \frac{1}{4} \sum_{k_1 k_2 k_3 k_4} \bar{v}_{k_1 k_2 k_3 k_4} a_{k_1}^\dagger a_{k_2}^\dagger a_{k_3} a_{k_4} \quad (3.44)$$

and replace it with the Routhian

$$\langle \text{BCS} | \hat{H} - \lambda \hat{N} | \text{BCS} \rangle \quad (3.45)$$

so that the expected number of particles may be fixed, under the appropriate choice of λ , by the relation

$$\frac{\partial}{\partial N} \langle \text{BCS} | \hat{H} | \text{BCS} \rangle = \lambda. \quad (3.46)$$

the Lagrange multiplier λ takes on the meaning of the chemical potential. We can now apply the variational principle (3.6) to (3.45) using the v_k as variational quantities, which yields

$$4\tilde{\varepsilon}_k^2 u_k^2 v_k^2 = \Delta_k^2 - 4\Delta_k^2 u_k^2 v_k^2, \quad (3.47)$$

where the pairing gap Δ_k is defined as

$$\Delta_k = - \sum_{k'} \bar{v}_{k\tilde{k}k'\tilde{k}'} v_{k'} u_{k'} \quad (3.48)$$

and the quantity $\tilde{\varepsilon}_k$ is defined as

$$\tilde{\varepsilon}_k = \frac{1}{2} \left[t_{kk} + t_{\tilde{k}\tilde{k}} - 2\lambda + \sum_{k'} (\bar{v}_{k\tilde{k}k'\tilde{k}'} v_{k'} u_{k'} + \bar{v}_{\tilde{k}k'\tilde{k}k'} v_{k'} u_{k'}) v_{k'}^2 \right] \quad (3.49)$$

$$= \frac{1}{2} [h_{kk} + h_{\tilde{k}\tilde{k}}] - \lambda. \quad (3.50)$$

Introducing the quasi-particle energy

$$E_k = \sqrt{\tilde{\varepsilon}_k^2 + \Delta_k^2} \quad (3.51)$$

we can combine definitions (3.48) and (3.51) with Equation (3.49), under the normalization condition (3.41), to get an equation for v_k^2

$$v_k^2 = \frac{1}{2} \pm \frac{|\tilde{\varepsilon}_k|}{2E_k}. \quad (3.52)$$

Since in the Hartree–Fock limit, where the occupations v_k^2 are equal to one below the Fermi energy and zero above, and the gaps Δ_k vanish, rendering $E_k = \tilde{\varepsilon}_k$, we only select the solution

$$v_k^2 = \frac{1}{2} - \frac{\tilde{\varepsilon}_k}{2E_k}. \quad (3.53)$$

Using the normalization condition to write $u_k^2 = 1 - v_k^2$, and plugging it into the gaps definition (3.48), we arrive to the gap equation

$$\Delta_k = - \sum_{k'} \frac{\Delta_{k'} \bar{v}_{k\tilde{k}k'\tilde{k}'}}{2E_{k'}}. \quad (3.54)$$

The system of equations (3.54, 3.41, 3.52, 3.51, 3.49), together with the condition on \hat{N} – ie $\langle \hat{N} \rangle = N$ – is closed and can be solved numerically, usually through an effective pairing interaction.

3.2.2. Hartree–Fock–Bogoliubov theory

The most general ansatz to account for pairing interactions in Hartree–Fock theory is the Hartree–Fock–Bogoliubov (HFB) theory, that allows a treatment of the mean-field and pairing interactions in a unified way. The quasi-particles created on the vacuum are not necessarily time-reversal pairs but the most general ones according to the symmetries of the system. Let us start by writing a Bogoliubov transformation from the particle basis c_i to a quasi-particle one

$$\beta_k^\dagger = \sum_l U_{lk} c_l^\dagger + V_{lk} c_l. \quad (3.55)$$

If we take the Hermitian conjugate of the relation (3.55), we get the transformation for β_k , and we are then able to write the two in matrix form

$$\begin{pmatrix} \beta \\ \beta^\dagger \end{pmatrix} = \begin{pmatrix} U^\dagger & V^\dagger \\ V^T & U^T \end{pmatrix} \begin{pmatrix} c \\ c^\dagger \end{pmatrix} = \mathcal{W}^\dagger \begin{pmatrix} c \\ c^\dagger \end{pmatrix}, \quad (3.56)$$

where the super-matrix of matrices \mathcal{W} reads

$$\mathcal{W} = \begin{pmatrix} U & V^* \\ V & U^* \end{pmatrix}. \quad (3.57)$$

Taking the product $\mathcal{W}^\dagger \mathcal{W}$ and imposing separate fermionic commutation relations of the operators $\beta, \beta^\dagger, c, c^\dagger$, we get that \mathcal{W} is unitary, hence

$$\mathcal{W}^\dagger \mathcal{W} = \mathcal{W} \mathcal{W}^\dagger = I. \quad (3.58)$$

We can now invert Equation (3.56) by multiplying both sides on the left by \mathcal{W} , which yields

$$\mathcal{W} \begin{pmatrix} \beta \\ \beta^\dagger \end{pmatrix} = \begin{pmatrix} c \\ c^\dagger \end{pmatrix}.$$

Using the Messiah-Bloch decomposition [51], we can write the unitary matrix \mathcal{W} as

$$\mathcal{W} = \begin{pmatrix} D & 0 \\ 0 & D^* \end{pmatrix} \begin{pmatrix} \bar{U} & \bar{V} \\ \bar{V} & \bar{U} \end{pmatrix} \begin{pmatrix} C & 0 \\ 0 & C^* \end{pmatrix} \quad (3.59)$$

where D and C are unitary matrices and \bar{U} and \bar{V} are real matrices, which have a particular blocked form, expressed through the coefficients u_k, v_k ; the reader may refer to

appendix A.4 for the explicit representation. We can also define the matrices U, V as

$$U = D\bar{U}C, \quad V = D^*\bar{V}C. \quad (3.60)$$

Using the decomposition (3.59) we can define the *canonical basis* as

$$a_k^\dagger = \sum_l D_{lk}^\dagger c_l^\dagger, \quad (3.61)$$

a *special Bogoliubov transformation* between *paired* levels as

$$\alpha_k^\dagger = u_k a_k^\dagger - v_k a_{\tilde{k}}^\dagger, \quad (3.62)$$

$$\alpha_{\tilde{k}}^\dagger = u_k a_k^\dagger + v_k a_{\tilde{k}}, \quad (3.63)$$

and *blocked* levels

$$\alpha_i = a_i, \quad \alpha_n^\dagger = a_n^\dagger \quad (3.64)$$

$$\alpha_i = a_i^\dagger, \quad \alpha_n = a_n, \quad (3.65)$$

where $u_k = u_{\tilde{k}}$, $v_k = -v_{\tilde{k}}$, and a unitary transformation of the quasi-particle operators α_k^\dagger among themselves

$$\beta_k^\dagger = \sum_{k'} C_{k'k} a_{k'}^\dagger. \quad (3.66)$$

We are now able to define the Bogoliubov ground state $|\text{HFB}\rangle$, as the one for which

$$\beta_k |\text{HFB}\rangle = 0 \quad \forall k = 1, \dots, M \quad (3.67)$$

where M is the number of single-particle states in the chosen basis. The wavefunction that satisfies this condition reads

$$|\text{HFB}\rangle = \prod_k^M \beta_k |-\rangle. \quad (3.68)$$

The *pairing tensor* is defined as

$$\kappa_{ll'} = \langle \text{HFB} | c_{l'} c_l | \text{HFB} \rangle, \quad (3.69)$$

which in matrix form reads

$$\kappa = U V^\dagger, \quad (3.70)$$

while the density matrix, defined in Equation (3.19), in matrix form reads

$$\rho = V^* V^T. \quad (3.71)$$

We can now apply the variational principle (3.6)

$$\delta \frac{\langle \text{HFB} | \hat{H} - \lambda \hat{N} | \text{HFB} \rangle}{\langle \text{HFB} | \text{HFB} \rangle} = 0, \quad (3.72)$$

which yields the eigenvalue problem

$$\begin{pmatrix} h - \lambda & \Delta \\ -\Delta^* & -(h - \lambda)^* \end{pmatrix} \begin{pmatrix} U_k \\ V_k \end{pmatrix} = \mathcal{H}_{\text{HFB}} \begin{pmatrix} U_k \\ V_k \end{pmatrix} = E_k \begin{pmatrix} U_k \\ V_k \end{pmatrix}, \quad (3.73)$$

here, h is the single-particle Hamiltonian, which reads

$$h_{kk'} = t_{kk'} + \Gamma_{kk'}, \quad (3.74)$$

and $\Gamma_{kk'}$ is the mean-field potential, given by

$$\Gamma_{kk'} = \sum_{ll'} \bar{v}_{kl'k'l} \rho_{ll'}, \quad (3.75)$$

while the pairing field Δ reads

$$\Delta_{kk'} = \sum_{ll'} \bar{v}_{kk'l'l} \kappa_{ll'}. \quad (3.76)$$

In the canonical basis, we are able to solve for the occupation numbers

$$u_k^2 = \frac{1}{2} \left(1 + \frac{h_{kk} + h_{\bar{k}\bar{k}}}{\sqrt{(h_{kk} + h_{\bar{k}\bar{k}})^2 + 4\Delta_{kk}^2}} \right) \quad (3.77)$$

where $v_k^2 = 1 - u_k^2$ is guaranteed by the unitarity of the matrices. Starting from an initial guess, we solve the eigenvalue problem (3.73), we extract the occupation numbers (3.77), use them to build the new mean-field (3.75) and pairing field (3.76), and repeat the process until convergence.

HFB quasi-particle spectrum Let us assume that $\Psi = (U, V)^T$ is a solution of Equation (3.73) with eigenvalue E

$$\mathcal{H}_{\text{HFB}} \Psi = E \Psi. \quad (3.78)$$

Let the particle-hole matrix \mathcal{C} be defined as

$$\mathcal{C} = \begin{pmatrix} 0 & I \\ I & 0 \end{pmatrix}, \quad (3.79)$$

it is trivial to show that

$$\mathcal{C} \mathcal{H}_{\text{HFB}} \mathcal{C} = -\mathcal{H}_{\text{HFB}}^*, \quad (3.80)$$

and

$$\mathcal{C} = \mathcal{C}^{-1} \implies \mathcal{C} \mathcal{H}_{\text{HFB}} = -\mathcal{H}_{\text{HFB}}^* \mathcal{C}. \quad (3.81)$$

If we take the complex conjugate of Equation (3.78), we get

$$\mathcal{H}_{\text{HFB}}^* \Psi^* = E \Psi^*, \quad (3.82)$$

if we multiply both sides on the left by \mathcal{C} and use (3.81), we get

$$\mathcal{H}_{\text{HFB}} \mathcal{C} \Psi^* = -E \mathcal{C} \Psi^*, \quad (3.83)$$

meaning that $\mathcal{C} \Psi^*$ is a solution of the eigenvalue problem (3.73) as well, with eigenvalue $-E$, hence for every quasi-particle state we have a corresponding opposite-sign one; moreover, it can be proven that the HFB hamiltonian is unbounded, both from below and above [52]. This feature poses a challenge for the numerical diagonalisation of the HFB problem, as we shall see in Section 4.2.

3.3. Microscopic theory and approaches to nuclear fission

Having described the framework of nuclear DFT and the treatment of pairing correlations within the HFB formalism, we wish to spend a few pages in regards to the microscopic theory of fission. As we shall see, the application of these frameworks to the description of nuclear fission is one of the main drives for the development of new, spatially unconstrained solvers.

3.3.1. Microscopic theory

The use of phenomenological macroscopic-microscopic models has long provided valuable insight into fission processes, allowing for the prediction of barrier heights and fragment yields through parametrised shape degrees of freedom and empirical shell corrections [53–55]. In these models, the total energy is expressed as

$$E_{\text{tot}}(\mathbf{q}) = E_{\text{LD}}(\mathbf{q}) + \delta E_{\text{shell}}(\mathbf{q}) + \delta E_{\text{pair}}(\mathbf{q}), \quad (3.84)$$

where E_{LD} is the macroscopic liquid-drop term depending on deformation coordinates \mathbf{q} , while δE_{shell} and δE_{pair} account for shell and pairing corrections, respectively. While such models reproduce many global observables, they lack a true microscopic foundation. In particular, the coordinates \mathbf{q} are not derived from the underlying many-body dynamics, and the empirical shell corrections cannot describe the self-consistent rearrangement of the mean-field along the fission path.

A more fundamental understanding is achieved within self-consistent mean-field approaches such as the HF or HFB formalisms. The resulting constrained HF/HFB calculations produce the potential energy surface (PES) $E(\mathbf{q})$, mapping the energy of the system as a function of collective deformations such as the quadrupole (Q_{20}), octupole (Q_{30}), and triaxial (Q_{22}) moments. The minima and saddle points of this multidimensional PES determine the fission barriers and shape isomeric states [3, 56].

However, static mean-field approaches are limited by their single-reference character: the HFB vacuum represents only one configuration at a time, typically corresponding to a local minimum of the PES. In the vicinity of the fission barrier, where several configurations with different intrinsic quantum numbers coexist, this approximation breaks down. The wave function should instead be expressed as a superposition of several self-consistent configurations $\{|\Psi(\mathbf{q})\rangle\}$, leading to a correlated state of the form

$$|\Psi\rangle = \int f(\mathbf{q}) |\Psi(\mathbf{q})\rangle d\mathbf{q}, \quad (3.85)$$

which is the essence of the *Generator Coordinate Method* (GCM) [57, 58]. The GCM maps the microscopic many-body problem onto a *collective Schrödinger equation* (CSE)

$$\left[-\frac{\hbar^2}{2} \sum_{ij} \frac{\partial}{\partial q_i} B_{ij}(\mathbf{q}) \frac{\partial}{\partial q_j} + V(\mathbf{q}) \right] g_k(\mathbf{q}) = E_k g_k(\mathbf{q}), \quad (3.86)$$

where $B_{ij}(\mathbf{q})$ is the collective inertia tensor and $V(\mathbf{q})$ the potential energy extracted from

constrained HFB. This framework naturally incorporates tunnelling through the barrier and provides access to observables such as fission lifetimes and fragment distributions.

Beyond-mean-field extensions also restore symmetries that are spontaneously broken at the mean-field level. For instance, particle-number, parity, and angular-momentum projection techniques [59, 60] are required to recover good quantum numbers and remove spurious symmetry mixing. In multi-reference DFT [6], these symmetry restorations can be combined with configuration mixing, yielding highly accurate fission barrier calculations.

3.3.2. Time-dependent DFT and the TDHF formalism

Static HF/HFB solutions provide a sequence of constrained energy minima along deformation coordinates, but they cannot describe the real-time evolution of the system. A fully dynamical extension is obtained within time-dependent Density Functional Theory (TDDFT), whose nuclear implementation corresponds to the time-dependent HF (TDHF) or time-dependent HFB(TDHFB) equations [61].

TDHF follows from the time-dependent variational principle applied to a Slater determinant

$$\delta \int dt \langle \Psi(t) | i\hbar\partial_t - \hat{H} | \Psi(t) \rangle = 0,$$

The resulting Euler-Lagrange equations lead to a set of non-linear Schrödinger equations for the occupied single-particle orbitals

$$i\hbar\partial_t\varphi_k(\mathbf{r}, t) = h[\rho(t)]\varphi_k(\mathbf{r}, t), \quad (3.87)$$

with $h[\rho(t)]$ the self-consistent mean-field Hamiltonian obtained from the Energy Density Functional. The time evolution of the one-body density matrix,

$$\rho_{ij}(t) = \langle \Psi(t) | a_j^\dagger a_i | \Psi(t) \rangle,$$

is therefore governed by the Liouville-von Neumann equation

$$i\hbar \frac{d\rho}{dt} = [h[\rho], \rho], \quad (3.88)$$

which ensures hermiticity, idempotency, and particle-number conservation. For Skyrme EDFs, the Hamiltonian includes local densities and currents, so the TDHF evolution also incorporates time-odd fields essential for dynamical processes [62].

In the presence of pairing, the formalism generalises to TDHFB through the Bogoliubov

density matrices

$$\mathcal{R}(t) = \begin{pmatrix} \rho(t) & \kappa(t) \\ -\kappa^*(t) & 1 - \rho^*(t) \end{pmatrix}, \quad \mathcal{H}(t) = \begin{pmatrix} h(t) & \Delta(t) \\ -\Delta^*(t) & -h^*(t) \end{pmatrix},$$

which satisfy the generalized equation of motion

$$i\hbar \frac{d\mathcal{R}}{dt} = [\mathcal{H}, \mathcal{R}]. \quad (3.89)$$

Time-dependent methods offer several key advantages for the description of fission dynamics. First, they treat collective motion and intrinsic excitations on the same footing: changes in configuration occur through level crossings, rearrangements of occupation probabilities, and dynamical time-odd fields. This enables the exploration of diabatic pathways unavailable to static constrained minimisation. Second, the scission process is described naturally as the neck density decreases and two self-bound fragments emerge, carrying well-defined densities, currents, and angular momenta. Fragment intrinsic excitation energy may be extracted from post-scission relaxation [63].

Despite these advantages, TDHF has fundamental limitations. Being restricted to a single Slater determinant, it cannot describe quantum tunnelling (necessary for spontaneous fission) nor generate fragment mass and charge distributions. Its dynamics is deterministic, yielding only the mean trajectory in collective space. Extensions such as the time-dependent random-phase approximation (TDRPA), the stochastic mean-field approach [64], and the time-dependent GCM with Gaussian overlap approximation [57] introduce fluctuations and correlations around the TDHF path, enabling more realistic descriptions of fission fragment observables.

3.3.3. Unconstrained Calculations and Symmetry Breaking

An equally important aspect of microscopic fission theory is the treatment of spatial symmetries. Historically, many calculations imposed constraints such as axial symmetry or reflection symmetry with respect to a plane to reduce the computational cost of solving the HFB equations. While such restrictions simplify the description of the nucleus, they artificially constrain the fission path and may even prevent the identification of energetically preferred configurations [65, 66], as shown in Figure 1.7. Fission involves strongly deformed, triaxial, and reflection-asymmetric shapes; the correct description of barrier heights and scission configurations therefore requires breaking as many spatial symmetries as possible.

In a self-consistent mean-field framework, spontaneous symmetry breaking is a feature rather than a flaw: it allows the system to adopt a deformed intrinsic shape corresponding to a broken rotational or parity symmetry, while the symmetry of the total many-body Hamiltonian is preserved. For example, an axially deformed HFB state violates rotational invariance, but the restoration of this symmetry through angular-momentum projection recovers the correct laboratory-frame properties. Triaxiality, for example, has been shown to lower the inner barrier of actinides by several MeV [3, 65]. Similarly, parity breaking through octupole deformation is essential to describe asymmetric fission fragment distributions. Likewise, reflection-asymmetric (octupole) degrees of freedom are necessary to reproduce mass-asymmetric fission in heavy nuclei.

Recent computational developments have made possible fully symmetry-unrestricted HFB and TDDFT calculations, in which all spatial and time-reversal symmetries can be broken if energetically favourable [3, 67]. Codes such as HFODD and Sky3D implement three-dimensional solvers capable of describing triaxial, octupole, and time-odd components of the density matrix. These advances have revealed new fission pathways, scission configurations, and fragment-spin correlations inaccessible to axially symmetric models.

3.4. Skyrme

Now that the theoretical framework is clear, we can use the Skyrme microscopic effective interaction to do nuclear structure calculations.

3.4.1. Skyrme force

The Skyrme interaction was first proposed by Tony Skyrme in 1958 [45] as a zero range force between nucleons, comprising a two body attractive term that reads

$$\begin{aligned} v^{(2)}(\mathbf{r}_1, \mathbf{r}_2) = & t_0 (1 + x_0 P_\sigma) \delta(\mathbf{r}) \\ & + \frac{1}{2} t_1 (1 + x_1 P_\sigma) [\mathbf{P}'^2 \delta(\mathbf{r}) + \delta(\mathbf{r}) \mathbf{P}^2] \\ & + t_2 P_\sigma \mathbf{P}' \cdot \delta(\mathbf{r}) \mathbf{P} \\ & + i W_0 \boldsymbol{\sigma} \cdot [\mathbf{P}' \times \delta(\mathbf{r}) \mathbf{P}] \end{aligned}$$

and a three body term, that is

$$v^{(3)}(\mathbf{r}_1, \mathbf{r}_2, \mathbf{r}_3) = t_3 \delta(\mathbf{r}_1 - \mathbf{r}_2) \delta(\mathbf{r}_2 - \mathbf{r}_3),$$

which mimics the repulsive three-body force; without it, a collapse of the nuclear density would occur. The different operators are defined as

$$\mathbf{r} = \mathbf{r}_1 - \mathbf{r}_2, \quad \mathbf{R} = \frac{\mathbf{r}_1 + \mathbf{r}_2}{2}, \quad (3.90)$$

which are respectively the relative position of two particles and their centre of mass coordinate, assuming equal masses,

$$\mathbf{P} = \frac{-i(\nabla_1 - \nabla_2)}{2} \quad (3.91)$$

which is the so called relative wave-number operator, corresponding to the relative momentum of the two interacting particles.

$$\boldsymbol{\sigma} = \boldsymbol{\sigma}_1 + \boldsymbol{\sigma}_2 \quad (3.92)$$

is the total spin of the two interacting particles, and lastly

$$\mathbf{P}_\sigma = \frac{(1 + \boldsymbol{\sigma}_1 \cdot \boldsymbol{\sigma}_2)}{2} \quad (3.93)$$

represents the spin-exchange operator. Primed operators refer to the adjoint acting on the left. It is trivial to show that the three-body term, in the case of even-even nuclei, is equivalent to a two-body, density-dependent interaction [7]

$$v^{(3)}(\mathbf{r}_1, \mathbf{r}_2) = \frac{1}{6} t_3 (1 + P_\sigma) \delta(\mathbf{r}) \rho(\mathbf{R}). \quad (3.94)$$

The zero-range feature is apparent in the choice of the Dirac delta $\delta(\mathbf{r})$, which allows the writing of the Fock term detailed in (3.15) as a purely local one.

Modern parametrisation

The Skyrme force has evolved from the original one to accomodate new nuclei and properties, done through the addition of a few parameters, yielding the following form of the

interaction [68]

$$\begin{aligned}
v^{(2)}(\mathbf{r}_1, \mathbf{r}_2) = & t_0 (1 + x_0 P_\sigma) \delta(\mathbf{r}) \\
& + \frac{1}{2} t_1 (1 + x_1 P_\sigma) [\mathbf{P}'^2 \delta(\mathbf{r}) + \delta(\mathbf{r}) \mathbf{P}^2] \\
& + t_2 (1 + x_2 P_\sigma) \mathbf{P}' \cdot \delta(\mathbf{r}) \mathbf{P} \\
& + \frac{1}{6} t_3 (1 + x_3 P_\sigma) [\rho(\mathbf{R})]^\sigma \delta(\mathbf{r}) \\
& + i W_0 \boldsymbol{\sigma} \cdot [\mathbf{P}' \times \delta(\mathbf{r}) \mathbf{P}] \\
& + \frac{1}{6} t_3 (1 + x_3 P_\sigma) [\rho(\mathbf{R})]^\sigma \delta(\mathbf{r})
\end{aligned}$$

Here, the boundary between Hartree–Fock and DFT starts to thin out, as the exponent σ of the density makes that piece of the force a true three-body interaction only for the value $\sigma = 1$ [69]. On top of that, additional, empirical tuning of the resulting energy density needed to reach satisfactory physical accuracy, such as the case for the spin-orbit couplings [70], prompts for the following, well-established proceeding: use the Skyrme interaction to obtain the Hamiltonian density

$$\langle H \rangle = \langle \Psi | H | \Psi \rangle = \int \mathcal{H}(\mathbf{r}) d\mathbf{r} \quad (3.95)$$

and use it as a starting point to build an Energy Density Functional and employ DFT.

3.4.2. Energy density functional

The energy functional to be minimised is of the form [6]

$$E_{\text{HF}} = E_{\text{Kin}} + E_{\text{Skyrme}} + E_{\text{Coul}} = \int (\mathcal{E}_{\text{Kin}} + \mathcal{E}_{\text{Skyrme}} + \mathcal{E}_{\text{Coul}}) d\mathbf{r}. \quad (3.96)$$

Densities

The energy functional (3.96) can be expressed through a series of generalized particle densities. Let us define them and express them on the spin coordinates up (\uparrow) and down (\downarrow) for the convenience in a mesh representation.

The starting point is the density matrix, defined as

$$\rho_q(\mathbf{r}\sigma, \mathbf{r}\sigma') = \sum_{\alpha} \phi_{\alpha,\sigma}(\mathbf{r}) \phi_{\alpha,\sigma'}^*(\mathbf{r}') \quad (3.97)$$

where the index α goes through all single particle states of the particles of type q (protons,

neutrons) and the index σ refers to the spin coordinate. The particle density is defined as

$$\begin{aligned}\rho_q(\mathbf{r}) &:= \rho_q(\mathbf{r}, \mathbf{r}') \Big|_{\mathbf{r}=\mathbf{r}'} \\ &:= \sum_{\sigma} \rho(\mathbf{r}\sigma, \mathbf{r}'\sigma) \Big|_{\mathbf{r}=\mathbf{r}'} \\ &= \sum_{\alpha} \phi_{\uparrow}(\mathbf{r})\phi_{\uparrow}^*(\mathbf{r}') + \phi_{\downarrow}(\mathbf{r})\phi_{\downarrow}^*(\mathbf{r}') \Big|_{\mathbf{r}=\mathbf{r}'} \\ &= \sum_{\alpha} |\phi_{\uparrow}(\mathbf{r})|^2 + |\phi_{\downarrow}(\mathbf{r})|^2.\end{aligned}\tag{3.98}$$

The kinetic density reads

$$\begin{aligned}\tau_q(\mathbf{r}) &:= \sum_{\alpha} \nabla' \cdot \nabla \rho_q(\mathbf{r}, \mathbf{r}') \Big|_{\mathbf{r}'=\mathbf{r}} \\ &= \sum_{\sigma, \alpha} \nabla \phi_{\sigma}(\mathbf{r}) \cdot \nabla \phi_{\sigma}^*(\mathbf{r}') \Big|_{\mathbf{r}=\mathbf{r}'} \\ &= \sum_{\sigma, \alpha} |\nabla \phi_{\sigma}(\mathbf{r})|^2 \\ &= \sum_{\alpha} |\nabla \phi_{\uparrow}(\mathbf{r})|^2 + |\nabla \phi_{\downarrow}(\mathbf{r})|^2.\end{aligned}\tag{3.99}$$

The spin density reads

$$s_q(\mathbf{r}, \mathbf{r}') := \sum_{\sigma\sigma', i} \rho_q(\mathbf{r}\sigma, \mathbf{r}'\sigma') \langle \sigma' | \hat{\boldsymbol{\sigma}} | \sigma \rangle = \sum_{\alpha} \begin{bmatrix} \phi_{\uparrow}^*(\mathbf{r}') & \phi_{\downarrow}^*(\mathbf{r}') \end{bmatrix} \hat{\boldsymbol{\sigma}} \begin{bmatrix} \phi_{\uparrow}(\mathbf{r}) \\ \phi_{\downarrow}(\mathbf{r}) \end{bmatrix}\tag{3.100}$$

and lastly, the spin-orbit density tensor reads

$$\begin{aligned}J_{q,\mu\nu} &:= \frac{1}{2i} (\partial_{\mu} - \partial'_{\mu}) s_{q,\nu}(\mathbf{r}, \mathbf{r}') \Big|_{\mathbf{r}'=\mathbf{r}} \\ &= \frac{1}{2i} \left(\begin{bmatrix} \phi_{\uparrow}^*(\mathbf{r}') & \phi_{\downarrow}^*(\mathbf{r}') \end{bmatrix} \partial_{\mu} \hat{\sigma}_{\nu} \begin{bmatrix} \phi_{\uparrow}(\mathbf{r}) \\ \phi_{\downarrow}(\mathbf{r}) \end{bmatrix} - \begin{bmatrix} \phi_{\uparrow}(\mathbf{r}) & \phi_{\downarrow}(\mathbf{r}) \end{bmatrix} \partial'_{\mu} \hat{\sigma}_{\nu} \begin{bmatrix} \phi_{\uparrow}^*(\mathbf{r}') \\ \phi_{\downarrow}^*(\mathbf{r}') \end{bmatrix} \right)_{\mathbf{r}'=\mathbf{r}} \\ &= \sum_{\alpha} \text{Im} \left\{ \begin{bmatrix} \phi_{\uparrow}^*(\mathbf{r}) & \phi_{\downarrow}^*(\mathbf{r}) \end{bmatrix} \partial_{\mu} \hat{\sigma}_{\nu} \begin{bmatrix} \phi_{\uparrow}(\mathbf{r}) \\ \phi_{\downarrow}(\mathbf{r}) \end{bmatrix} \right\}\end{aligned}\tag{3.101}$$

which also defines the spin-orbit current vector \mathbf{J} that reads

$$J_{q,\kappa}(\mathbf{r}) = \sum_{\mu\nu} \epsilon_{\kappa\mu\nu} J_{q,\mu\nu}(\mathbf{r}).\tag{3.102}$$

Kinetic functional

The kinetic term can be expressed as

$$\mathcal{E}_{\text{Kin}} = \frac{\hbar^2}{2m} \tau \quad (3.103)$$

which is found integrating by parts (3.34).

Skyrme functional

Since this work only deals with even-even nuclei, only time-even densities, which are the ones previously defined, are non-vanishing, due to the ground state being time-reversal invariant [6]. This reduces the Skyrme functional to the following form [71]

$$\mathcal{E}_{\text{Skyrme}} = \sum_{t=0,1} \left\{ C_t^\rho [\rho_0] \rho_t^2 + C_t^{\Delta\rho} \rho_t \nabla^2 \rho_t + C_t^{\nabla \cdot J} \rho_t \nabla \cdot \mathbf{J}_t + C_t^\tau \rho_t \tau_t \right\} \quad (3.104)$$

where

$$C_0^\rho = +\frac{3}{8}t_0 + \frac{3}{48}t_3 \rho_0^\sigma, \quad (3.105)$$

$$C_1^\rho = -\frac{1}{8}t_0(1+2x_0) - \frac{1}{48}t_3(1+x_3)\rho_0^\sigma, \quad (3.106)$$

$$C_0^\tau = +\frac{3}{16}t_1 + \frac{1}{16}t_2(5+4x_2), \quad (3.107)$$

$$C_1^\tau = -\frac{1}{16}t_1(1+2x_1) + \frac{1}{16}t_2(1+2x_2), \quad (3.108)$$

$$C_0^{\Delta\rho} = -\frac{9}{64}t_1 + \frac{1}{64}t_2(5+4x_2), \quad (3.109)$$

$$C_1^{\Delta\rho} = +\frac{3}{64}t_1(1+2x_1) + \frac{1}{64}t_2(1+2x_2), \quad (3.110)$$

$$C_0^{\nabla \cdot J} = -\frac{3}{4}W_0, \quad (3.111)$$

$$C_1^{\nabla \cdot J} = -\frac{1}{4}W_0. \quad (3.112)$$

Here, $t = 0, 1$ refers to the isoscalar and isovector components of the densities, that is

$$\rho_0 = \rho_p + \rho_n,$$

$$\rho_1 = \rho_p - \rho_n$$

and the same holds for all generalised densities. We can now derive the Kohn–Sham equations, by minimising the functional under the constraint

$$\langle \varphi_i | \varphi_j \rangle = \delta_{ij}. \quad (3.113)$$

The resulting Kohn–Sham equations are of the form

$$\left[-\nabla \left(\frac{\hbar^2}{2m_q^*(\mathbf{r})} \nabla \right) + U_q(\mathbf{r}) + \delta_{q,\text{proton}} U_C(\mathbf{r}) - i\mathbf{B}_q(\mathbf{r}) \cdot (\nabla \times \boldsymbol{\sigma}) \right] \varphi_\alpha = \varepsilon_\alpha \varphi_\alpha \quad (3.114)$$

where an effective mass field arises, which is defined as

$$\frac{\hbar^2}{2m_q^*(\mathbf{r})} = \frac{\delta \mathcal{E}}{\delta \tau_q}, \quad (3.115)$$

a mean-field potential, which reads

$$U_q(\mathbf{r}) = \frac{\delta \mathcal{E}}{\delta \rho_q} \quad (3.116)$$

and a spin-orbit field, given by

$$\mathbf{B}_q(\mathbf{r}) = \frac{\delta \mathcal{E}}{\delta \mathbf{J}_q}. \quad (3.117)$$

The coulomb field U_C , which is present only in the single particle equation for protons, doesn't come from the Skyrme interaction, rather from the Coulomb part of the whole functional. It will be properly derived in Section 3.5.

Following the rules for functional derivatives, outlined in the appendix A.3 we get

$$\begin{aligned} \frac{\hbar^2}{2m_q^*(\mathbf{r})} &= + \frac{\hbar^2}{2m} \\ &+ \frac{1}{8} [t_1(2+x_1) + t_2(2+x_2)] \rho(\mathbf{r}) \\ &- \frac{1}{8} [t_1(1+2x_1) + t_2(1+2x_2)] \rho_q(\mathbf{r}) \end{aligned} \quad (3.118)$$

$$\begin{aligned}
U_q(\mathbf{r}) = & + \frac{1}{8} [t_1(2+x_1) + t_2(2+x_2)]\rho \\
& + \frac{1}{8} [t_2(1+2x_2) - t_1(1+2x_1)]\rho_q \\
& + \frac{1}{8} [t_1(2+x_1) + t_2(2+x_2)]\tau \\
& + \frac{1}{8} [t_2(1+2x_2) - t_1(1+2x_1)]\tau_q \\
& + \frac{1}{16} [t_2(2+x_2) - 3t_1(2+x_1)]\nabla^2\rho \\
& + \frac{1}{16} [3t_1(2x_1+1) + t_2(2x_2+1)]\nabla^2\rho_q
\end{aligned} \tag{3.119}$$

$$\begin{aligned}
\mathbf{B}_q(\mathbf{r}) = & + \frac{1}{2} W_0 [\nabla\rho + \nabla\rho_q] \\
& - \frac{1}{8} (t_1x_1 + t_2x_2)\mathbf{J} + \frac{1}{8} (t_1 - t_2)\mathbf{J}_q.
\end{aligned} \tag{3.120}$$

Unless otherwise specified, unlabelled densities denote isoscalar quantities (sum of neutron and proton).

3.4.3. Functionals

The set of parameters $(t_0, t_1, t_2, t_3, x_0, x_1, x_2, \sigma, W_0)$ in the Skyrme functional (3.104) is not universal and varies between different parametrisations. These parameters are fitted to experimental data so that the resulting EDF can reproduce known nuclear properties with good accuracy.

The last widely used family of Skyrme forces derived directly from an effective interaction is the SLy series, which was primarily fitted to properties of magic nuclei and to constraints from neutron-rich matter in neutron stars [72]. Subsequently, the development of new parametrisations has been driven by the need to reproduce more accurately the masses and radii of nuclei across the nuclear chart, including open-shell and deformed systems. Notable examples include the classic SIII force [73], the deformation-oriented SkM* parametrisation [74] to accurately reproduce the ^{240}Pu fission barrier, and modern large-scale optimisations such as UNEDF0 [75].

3.5. Coulomb interaction

Unlike the Skyrme interaction, the Coulomb force is finite-range, giving rise to an unwanted integral operator in the single-particle Hamiltonian. A well known and widely used

device is the Slater approximation [76], which gives a local exchange interaction. In this approximation, the Coulomb energy reads

$$E_{\text{Coul}} = \int \mathcal{E}_{\text{Coul}}(\mathbf{r}) d\mathbf{r},$$

where the energy density is given by

$$\mathcal{E}_{\text{Coul}}(\mathbf{r}) = \frac{e^2}{2} \left[\int \frac{\rho_p(\mathbf{r})\rho_p(\mathbf{r}')}{|\mathbf{r} - \mathbf{r}'|} d\mathbf{r}' - \frac{3}{2} \left(\frac{3}{\pi} \right)^{\frac{1}{3}} \rho_p^{4/3}(\mathbf{r}) \right], \quad (3.121)$$

which results in the Coulomb potential field

$$U_C(\mathbf{r}) = \frac{\delta \mathcal{E}_{\text{Coul}}}{\delta \rho_p} = \frac{e^2}{2} \left[\int \frac{\rho_p(\mathbf{r}')}{|\mathbf{r} - \mathbf{r}'|} d^3\mathbf{r}' - 2 \left(\frac{3}{\pi} \right)^{\frac{1}{3}} \rho_p^{1/3}(\mathbf{r}) \right] \quad (3.122)$$

where the first term is the direct Coulomb interaction, which simply is the Coulomb energy generated by the proton density, while the second term is the exchange Coulomb interaction, which is local and depends on the proton density through a power factor of 1/3. From a computational standpoint, the exchange part is trivial, while the direct one is more involved. One could compute the integral, but the complexity on a 3D mesh grows as $\mathcal{O}(N^6)$, where N is the total number of points on the mesh, rendering it unfeasible for fine calculations.

An alternative approach is to solve the Poisson equation (from now on, V_c refers to the direct part only)

$$\nabla^2 V_c = 4\pi e^2 \rho_p. \quad (3.123)$$

Given the proton density, we can impose Dirichlet boundary conditions, which can be extracted from a quadrupole expansion of the charge density [77]

$$V_c(\mathbf{r}) = 4\pi e^2 \sum_{\lambda=0}^2 \sum_{\mu=-\lambda}^{\lambda} \frac{\langle Q_{\lambda\mu} \rangle Y_{\lambda\mu}}{r^{1+\lambda}} \text{ on } \partial\Omega, \quad (3.124)$$

where $\langle Q_{\lambda\mu} \rangle$ is defined as

$$\langle Q_{\lambda\mu} \rangle = \int r^\lambda Y_{\lambda\mu}^*(\mathbf{r}) \rho_p(\mathbf{r}) d^3\mathbf{r}. \quad (3.125)$$

Since we expect a charge density confined to the nuclear shape, higher order terms in the expansion can be neglected, provided that the box is sufficiently large. In a reference

frame where the nucleus centre of mass is at the origin, the expansion reduces to

$$V_c(\mathbf{r}) = \frac{Ze^2}{r} + e^2 \sum_{\mu=-2}^2 \frac{\langle Q_{2\mu} \rangle Y_{2\mu}}{r^3} \text{ on } \partial\Omega. \quad (3.126)$$

The reader may refer to appendix A.1 for the definition and numerical evaluation of the spherical harmonics $Y_{\lambda\mu}$.

3.6. Energy calculation

One, if not the most important physical quantity we want to compute is the total energy of the system.

Integrated energy

The obvious way would be to evaluate the functional for a given density. We will call this *integrated energy*.

$$E_{\text{int}} = E[\rho, \tau, J_{\mu\nu}] = \int \mathcal{E} d\mathbf{r}$$

Hartree–Fock energy

An alternative approach can be used, as in a stationary point $\delta E = 0$, the single particle eigenvalue Equation (3.114) stands true, summarised as

$$(t + U)\varphi_k = \varepsilon_k \varphi_k. \quad (3.127)$$

We can multiply (3.127) on the left by φ_k^* and integrate to get

$$\int -\varphi_k^* \frac{\hbar^2}{2m} \nabla^2 \varphi_k d\mathbf{r} + \int \varphi_k^* U \varphi_k d\mathbf{r} = \int \varphi_k^* \varepsilon_k \varphi_k d\mathbf{r}. \quad (3.128)$$

The integral on the right hand side of (3.128) evaluates to ε_k due to the orthonormality constraint. If we sum over all states k we get

$$\begin{aligned} \sum_k \left\{ \int -\varphi_k^* \frac{\hbar^2}{2m} \nabla^2 \varphi_k d\mathbf{r} + \int \varphi_k^* U \varphi_k d\mathbf{r} \right\} &= \sum_k \varepsilon_k \\ \sum_k t_k + \int \rho U &= \sum_k \varepsilon_k. \end{aligned} \quad (3.129)$$

Since U is calculated as the functional derivative with respect to the density ρ (3.116), assuming that the functional has a power dependence from ρ of the form $\mathcal{E}_{\text{Skyrme}} = A\rho^{\sigma+1}$ as in our case, we get the *rearrangement energy*

$$\rho U = \rho \frac{\delta \mathcal{E}_{\text{Skyrme}}}{\delta \rho} = \rho(1 + \sigma)A\rho^\sigma = (1 + \sigma)A\rho^{\sigma+1} = \mathcal{E}_{\text{Skyrme}} + \sigma\mathcal{E}_{\text{Skyrme}} = \mathcal{E}_{\text{Skyrme}} - \mathcal{E}_{\text{rea}}. \quad (3.130)$$

If we explicit ρU in Equation (3.129) using (3.130), we get to

$$\sum_k t_k + \int (\mathcal{E}_{\text{Skyrme}} - \mathcal{E}_{\text{rea}}) d\mathbf{r} = \sum_k \varepsilon_k,$$

isolating the Skyrme energy density

$$\int \mathcal{E}_{\text{Skyrme}} d\mathbf{r} = \sum_k (\varepsilon_k - t_k) + \int \mathcal{E}_{\text{rea}} d\mathbf{r} \quad (3.131)$$

and given the total energy of the system from Equation (3.11)

$$E = \sum_k t_k + \frac{1}{2} \int \mathcal{E}_{\text{Skyrme}} d\mathbf{r} \quad (3.132)$$

substituting (3.131) in (3.132) yields

$$E_{\text{HF}} = \frac{1}{2} \sum_k (\varepsilon_k + t_k) + \int \mathcal{E}_{\text{rea}} d\mathbf{r} = \frac{1}{2} \left(T + \sum_k \varepsilon_k \right) + E_{\text{rea}} \quad (3.133)$$

which is called *Hartree–Fock energy*.

Sidenote The actual functional, including the Coulomb exchange term, has different ρ terms, which can be summarised as

$$\mathcal{E}_{\text{Skyrme}} = \sum_j A_j \rho^{\sigma_j+1} \implies E_{\text{rea}} = - \sum_j \sigma_j A_j \rho^{\sigma_j+1}$$

This means that only terms with a $\sigma_j \neq 0, -1$ actually contribute to the rearrangement energy. Since Equation (3.133) is valid only for $\delta E = 0$, it is useful to check its equivalence with the integrated energy at convergence, so one can be sure to actually be in a stationary point of the EDF.

4 | Numerical methods

This chapter is devoted to describing the practical implementation of the nuclear Hartree–Fock method of this work. In Section 4.1, the two partial differential equations (PDEs) of interest, the Kohn–Sham equation and the Poisson equation, are numerically approximated through finite differences. In Section 4.2, a breakdown of numerical solvers for the large-scale eigenvalue problem posed by the KS equation is presented, to pedagogically illustrate the rationale and implementation of the GCG algorithm. Finally, in Section 4.3, the self-consistent calculation is presented, along with the implementation of spatial constraints and the optimisation of the numerical parameters of GCG.

4.1. Finite differences

The framework used to numerically solve the relevant PDEs of the problem, is the one of finite differences. The core idea is to discretise the domain on a 3D mesh, use Taylor expansions to approximate differential operators and then solve the resulting system of linear equations.

4.1.1. 3D mesh

The first step of the process is representing the different fields in a numerical, discretised fashion. Generally speaking, we deal at most with 2-rank tensors, which depend on three space coordinates and one spin coordinate. Discretizing the 3D Cartesian space with a 3-index mesh, choosing a box whose size along x, y, z is respectively $[-a_x, +a_x]$, $[-a_y, +a_y]$, $[-a_z, +a_z]$, and a number of points n_x, n_y, n_z , the resulting lattice will be given by

$$V = \{(-a_x + ih_x, -a_y + ih_y, -a_z + ih_z)\} = \{(x_i, y_j, z_k)\},$$

where the indices and step sizes are

$$\begin{aligned} i = 0, \dots, n_x - 1 \quad h_x &= \frac{2a_x}{n_x - 1}, \\ j = 0, \dots, n_y - 1 \quad h_y &= \frac{2a_y}{n_y - 1}, \\ k = 0, \dots, n_z - 1 \quad h_z &= \frac{2a_z}{n_z - 1}. \end{aligned}$$

The following implementation assumes $a = a_x = a_y = a_z = a$ and $n = n_x = n_y = n_z = n$, without losing generality. Including the spin degree of freedom, we can finally represent the fields in a numerical way through

$$\varphi(\mathbf{r}, \sigma) \mapsto \varphi(x_i, y_j, z_k, s) = \varphi_{ijkl}. \quad (4.1)$$

Differential operators discretization

By using Taylor series, it is possible to write approximations to derivatives [78], in any point of the lattice, of any (reasonable) order of accuracy, involving only near neighbouring points. In the present work, 5-points derivatives are used, meaning Taylor expansions are written for $\varphi(x \pm h)$ and $\varphi(x \pm 2h)$ to compute the differential operators. Formulae for first and second derivates are given in appendix A.2. From the theory background of Chapter 3, we discern two main kinds of PDEs: the Schrödinger-like KS equation, and the Poisson equation.

4.1.2. Schrödinger equation

Starting from the Schrödinger Equation (3.114), reported here for clarity:

$$\left[-\nabla \left(\frac{\hbar^2}{2m_q^*(\mathbf{r})} \nabla \right) + U_q(\mathbf{r}) + \delta_{q,\text{proton}} U_C(\mathbf{r}) - i\mathbf{B}_q(\mathbf{r}) \cdot (\nabla \times \boldsymbol{\sigma}) \right] \varphi = \varepsilon \varphi,$$

it can be compactly written as

$$f(\nabla^2 \varphi, \nabla \varphi, \varphi, \mathbf{r}, s) = \varepsilon \varphi. \quad (4.2)$$

If f is linear in φ , it is possible to rewrite it as a linear combination of the values of φ on the mesh, after which we can use linear algebra methods to solve the problem.

Linearity Breaking down each part of the equation, the kinetic term

$$\nabla \left(\frac{\hbar^2}{2m_q^*(\mathbf{r})} \nabla \right) \varphi = \frac{\hbar^2}{2m_q^*(\mathbf{r})} \nabla^2 \varphi + \nabla \left(\frac{\hbar^2}{2m_q^*(\mathbf{r})} \right) \cdot \nabla \varphi \quad (4.3)$$

is evidently linear in φ . The spin-orbit term of (3.114), which we write as

$$\begin{aligned} \hat{h}_{SO} &= -i\mathbf{B}_q(\mathbf{r}) \cdot (\nabla \times \boldsymbol{\sigma}) \\ &= -i[\mathbf{B}_{q,x}(\mathbf{r})(\sigma_z \partial_y - \sigma_y \partial_z) + \mathbf{B}_{q,y}(\mathbf{r})(\sigma_x \partial_z - \sigma_z \partial_x) + \mathbf{B}_{q,z}(\mathbf{r})(\sigma_y \partial_x - \sigma_x \partial_y)] \end{aligned}$$

is also linear in φ . Finally, the mean-field terms U_q, U_c

$$(U_q + \delta_{q,\text{proton}} U_c) \varphi$$

are just multiplicative, hence linear.

Given that the whole equation is linear in φ , we can evaluate it on the chosen mesh, using finite differences to approximate the differential operators, yielding a linear eigenvalue problem of the form

$$\sum_{\alpha=1}^N A_{\alpha\beta} \varphi_\beta = E \varphi_\alpha \quad (4.4)$$

where the shorthand notation $N = 2 \cdot N_x \cdot N_y \cdot N_z$ is used to denote the size of the matrix A , which is $N \times N$.

Boundary conditions

We expect the nucleus to be a localised object, leading to vanishing Dirichlet boundary conditions for the Schrödinger equation. Near the boundaries, the derivatives will involve points outside the box and setting these points to zero, is equivalent to solving

$$\begin{bmatrix} 0 & 0 & 0 & 0 & 0 \\ 0 & 0 & 0 & 0 & 0 \\ 0 & 0 & A & 0 & 0 \\ 0 & 0 & 0 & 0 & 0 \\ 0 & 0 & 0 & 0 & 0 \end{bmatrix} \begin{bmatrix} \varphi_{-2} \\ \varphi_{-1} \\ \varphi \\ \varphi_N \\ \varphi_{N+1} \end{bmatrix} = E \begin{bmatrix} \varphi_{-2} \\ \varphi_{-1} \\ \varphi \\ \varphi_N \\ \varphi_{N+1} \end{bmatrix} \quad (4.5)$$

from this system of equations, we get for points outside the boundary:

$$\begin{cases} \varphi_{-2} = 0 \\ \varphi_{-1} = 0 \\ \dots \end{cases} \quad (4.6)$$

Meaning that φ outside the box will automatically be set to zero if the A matrix is built assuming those points to be zero when computing its coefficients.

4.1.3. Poisson equation

The other fundamental PDE we need to solve is the Poisson equation encountered in Section 3.5. Dropping the c and p subscripts, it reads

$$\nabla^2 V = 4\pi e^2 \rho.$$

It is simpler than the Schrödinger equation, as it only involves a Laplacian and it is not an eigenvalue problem. The right hand side is given, and the solution is found by inverting the coefficients' matrix.

Boundary conditions

Unlike the Schrödinger equation, we do not expect the solution to rapidly decay near the boundaries; as reported in Section 3.5, we have fixed, non-vanishing boundary conditions, which we have to properly impose on the system. We can choose a direction, say x , and look at the discretised equation at the boundaries $x = \pm a$. Since the indices j, k won't vary, we can omit them, and ignore the other derivates in the following equations. The discretization of the Poisson equation reads

$$\begin{aligned} \nabla^2 V &= \partial_{xx} V + \partial_{yy} V + \partial_{zz} V \\ &= \frac{-V_{i-2} + 16V_{i-1} - 30V_i + 16V_{i+1} - V_{i+2}}{12h^2} + \dots = 4\pi e^2 \rho_i. \end{aligned} \quad (4.7)$$

Near a boundary, say $i = 0$, the formula calls for points outside the box, known as *ghost points*. Since they are not part of the linear system, but they are known, we can bring them on the right hand side of Equation (4.7)

$$\frac{-30V_0 + 16V_1 - V_2}{12h^2} = 4\pi e^2 \rho_0 + \frac{V_{-2} - 16V_{-1}}{12h^2} = \tilde{\rho}_0. \quad (4.8)$$

The same procedure must be applied to all equations involving ghost points, eg for $i = 1$

$$\frac{+16V_0 - 30V_1 + 16V_2 - V_3}{12h^2} = 4\pi e^2 \rho_1 + \frac{V_{-1}}{12h^2} = \tilde{\rho}_1. \quad (4.9)$$

The proper system to solve will then be

$$AV = \tilde{\rho}. \quad (4.10)$$

Where A is constructed as previously specified. Solving with $\tilde{\rho}$ on the right hand side will force the solution to obey boundary conditions.

On higher order approximations and performance

Higher and higher order approximations for derivatives involve more points that are further away. This increases accuracy by reducing the finite differences error, but it also decreases the matrix sparseness.

4.2. Eigenvalue problem

This section is devoted to the approximate solution of the eigenvalue problem, needed for the Schrödinger Equation (3.114). The analysis and implementation work presented here was developed within the additional thesis activity carried out for the Honours Programme *Scientific Research in Industrial Engineering – Nuclear Science and Technology*.

Eigenvalue problems are ubiquitous in physics and engineering, and while solving one for a small matrix is trivial, it still requires roughly $O(n^3)$ operations [79] to do so. More often than not, real computational applications result in large-scale matrices, which are completely out of question for exact eigenvalues calculations, thus requiring the use of approximate algorithms.

We will begin by describing common building blocks of iterative eigensolvers in Section 4.2.1, namely:

- the approximate solutions of linear systems by the use of the Conjugate Gradient method;
- matrix preconditioning to speed up convergence;
- the Rayleigh-Ritz procedure to find good approximations to the eigenpairs in a certain subspace; and

- the shift-and-invert method, to select the desired portion of the eigenvalue spectrum.

After describing these building blocks, some of the most commonly used eigensolvers are described in Section 4.2.2, focusing on the core ideas and stating their limitations, to finally address the Generalised Conjugate Gradient method, whose implementation in the present work is detailed in Section 4.2.3.

4.2.1. Conjugate Gradient and numerical techniques

Conjugate Gradient method

Solving linear systems of the form

$$Ax = b \quad (4.11)$$

is crucial in many eigensolvers. The Conjugate Gradient (CG) is perhaps the most famous iterative solver in this sense, especially in connection with sparse matrices, as we will see in a moment. CG applies to cases where A is a real, $n \times n$, positive-definite, symmetric matrix, and x and b are n -dimensional vectors. Many generalisations to this method exist, which relax the requirements on the matrix, like BiCGSTAB, CGRES and so on [80]. We will describe the working principle of CG, but the same applies to all the others, with slight variations.

Steepest descent method The quadratic form $f(x)$ derived from the system (4.11) is

$$f(x) = \frac{1}{2}x^T Ax - b^T x, \quad (4.12)$$

if A is symmetric, positive-definite, the shape of $f(x)$ is convex and has a global minimum for

$$\nabla_x f(x) = Ax_m - b = 0 \implies Ax_m = b, \quad (4.13)$$

hence the extremum of the quadratic form is the also the solution of the linear system (4.11). We can employ the well-known gradient descent technique [81] to find such point: starting from a guess x_0 , we compute the direction d_i where f decreases the most (the residual r_i), compute the step size that gives the largest decrease, and update x_i at each

iteration accordingly, repeating until convergence.

$$d_i = r_i = b - Ax_i, \quad (4.14)$$

$$x_{i+1} = x_i + \alpha_i r_i, \quad (4.15)$$

$$\text{with } \alpha_i \text{ such that } \frac{df}{d\alpha_i} = 0 \implies \alpha_i = \frac{r_i^T r_i}{r_i^T A r_i}. \quad (4.16)$$

This is a powerful but highly inefficient procedure. We are not ensuring that the search direction doesn't end up with components in subspaces that were explored already. It can be proven [81] that the norm of the error $e_i = x_i - x_m$ is minimal at each iteration if the search directions d_i are chosen to be A -orthogonal to the next error, i.e. $d_i^T A e_{i+1} = 0$. This makes the algorithm converge at the exact solution in n steps, but most importantly it allows to truncate the iterations without a large error on the approximation x_i . In this case, the algorithm is called Conjugate Gradient Method and is formulated as

$$\alpha_i = \frac{r_i^T r_i}{d_i^T A d_i}, \quad (4.17)$$

$$x_{i+1} = x_i + \alpha_i d_i, \quad (4.18)$$

$$r_{i+1} = r_i - \alpha_i A d_i, \quad (4.19)$$

$$\beta_{i+1} = \frac{r_{i+1}^T r_{i+1}}{r_i^T r_i}, \quad (4.20)$$

$$d_{i+1} = r_{i+1} + \beta_{i+1} d_i, \quad (4.21)$$

where iterations are truncated if the norm of the residual r_i is smaller than a certain threshold. It can be proven that the orthonormalization of the new search direction, with respect to all the previous ones, can be done only through the rescaling factor β_{i+1} [81]. CG converges to the exact solution in n steps, moreover, it represents a great method for sparse matrices, because it can be proven to be of complexity $O(m)$, where m is the number of non-zero elements in A [81]. In Figure 4.1, a visual representation of the conjugation of search directions and the subsequent exact solution is shown for a two-dimensional problem.

Complex matrices Algorithm (4.17) and the CG method in general can be used for complex matrices, under the condition that A is Hermitian and positive-definite when using the complex inner product, meaning that

$$A = A^\dagger \text{ and } x^\dagger A x > 0. \quad (4.22)$$

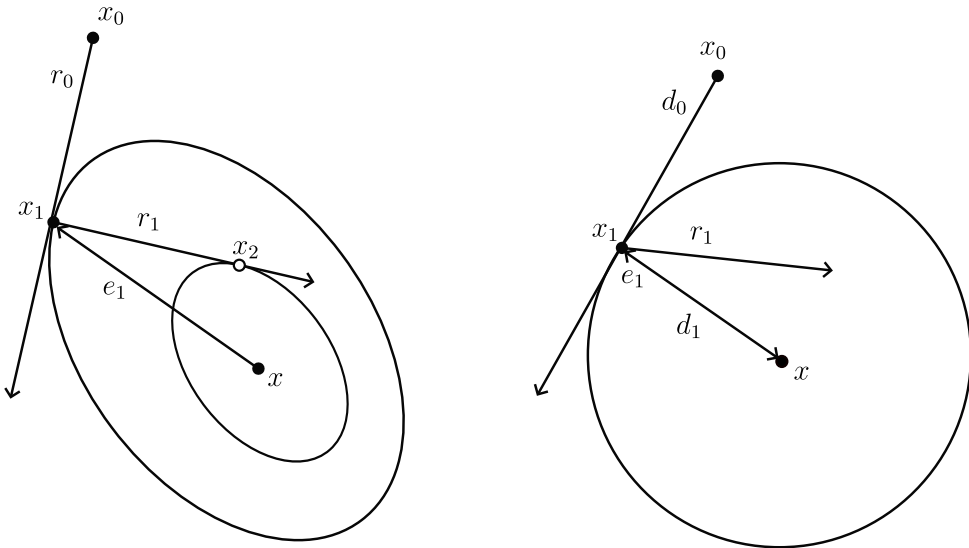


Figura 4.1: Comparison between the steepest descent method on the left, and the conjugate gradient method on the right, for a two-dimensional matrix. Ellipses represent contour lines of the quadratic form $f(x) = x^T Ax - b^T x$, in the ‘stretched’ space Ax on the right. As shown in the figure, the conjugation of the search directions eliminates components of the error e_i , until the exact convergence in n (2) steps.

Preconditioning

The CG method convergence is known to be limited by the modulus of the condition number of A , $\kappa(A)$, given by [81]

$$\kappa(A) = \frac{\lambda_{\max}(A)}{\lambda_{\min}(A)}, \quad (4.23)$$

where λ_{\max} and λ_{\min} are respectively the largest and smallest eigenvalues of A in magnitude. If we were able to find a good *preconditioner* M , symmetric and positive-definite, such that $\kappa(M^{-1}A) \ll \kappa(A)$, and M^{-1} is easy to compute, then the algorithm would converge much faster, by solving $M^{-1}Ax = M^{-1}b$, since x is also the solution of $Ax = b$.

$$x = (M^{-1}A)^{-1}M^{-1}b = A^{-1}MM^{-1}b = A^{-1}b. \quad (4.24)$$

Without delving into the details of the preconditioner implementation, detailed in [81], note that, in general, $M^{-1}A$ is neither positive-definite nor symmetric, which requires a Cholesky decomposition [82] $M = EE^T$ to be used, so that the problem may be restated with a symmetric positive-definite matrix $E^{-1}AE^{-T}$. The catch with preconditioning is that M has no unique recipe. Preconditioners are widely spread across numerical analysis, so many methods have been explored and implemented [83].

Rayleigh-Ritz procedure

A common denominator of all these algorithms is the search of good approximations for the correct eigenvectors in a certain subspace. The method is called Rayleigh-Ritz (RR) procedure [80], and is here outlined.

Let us suppose to have a matrix A of size $n \times n$, with entries in \mathbf{C} and a collection of vectors k organized in a matrix K , where K is of size $n \times k$. Generally speaking, n is large, while k is much smaller. The best approximation of the true eigenvectors of A in the subspace \mathcal{K} , spanned by the vectors in K , can be computed by solving the small scale eigenvalue problem

$$K^\dagger A K C = C \Lambda. \quad (4.25)$$

Here matrices $K^\dagger A K$ and C are of size $k \times k$. Computing $K C$ gives a matrix of size $n \times k$, whose column vectors are the best approximations of the true eigenvectors of A in the subspace \mathcal{K} , with their corresponding eigenvalues in the entries of the diagonal matrix Λ .

Shift and Invert

The power iteration is the technique on which Krylov subspace search methods are based [79]. By repeatedly applying matrix A to a vector x , x gets skewed towards the eigenvector whose eigenvalue is of largest magnitude λ_n .

Let us assume A is a hermitian matrix, thus diagonalizable. This means we can write an arbitrary vector $x^{(0)}$ as a linear combination of the eigenvectors $\{v_i\}$ of A

$$x^{(0)} = \sum_i^n \alpha_i v_i. \quad (4.26)$$

If we apply A to $x^{(0)}$ k times, we get

$$x^{(k)} = A^k x^{(0)} = \sum_i^n \alpha_i A^k v_i = \sum_i^n \alpha_i \lambda_i^k v_i. \quad (4.27)$$

It can be proven that the ratio of the j -th component of $x_j^{(k)}$ and $x_j^{(k-1)}$ converges to λ_n

$$\lim_{k \rightarrow \infty} \frac{x_j^{(k)}}{x_j^{(k-1)}} = \lambda_n, \quad (4.28)$$

which means, that for large enough k , we have the relation

$$Ax^{(k)} \approx \lambda_n x^{(k)}. \quad (4.29)$$

So $x^{(k)}$ is an approximation of the eigenvector v_n of A whose eigenvalue is λ_n .

Smallest eigenvalue If instead of the largest eigenvalue, we were interested in the smallest one – in magnitude – λ_0 , then we would need to apply the inverse matrix A^{-1} to $x^{(k)}$, which would change the ratio (4.28) to

$$\lim_{k \rightarrow \infty} \frac{x_j^{(k)}}{x_j^{(k-1)}} = \lambda_0. \quad (4.30)$$

Let us assume for a moment that we are solving a nuclear single-particle Hamiltonian, where we have a certain number of bound states of negative energy and a much larger number of unbound states with positive energy. In this case, the inverse power iteration would converge to the states whose energy is closer to zero, avoiding the interesting ones at the bottom of the spectrum. The solution is, before inverting, to shift the matrix by a quantity σ that is very close to the lowest eigenvalue we want to compute, call it λ_σ (eigenvector v_σ). Now, the eigenvalue of lowest magnitude of $(A - \sigma I)$ is $\lambda_\sigma - \sigma$ and by applying $(A - \sigma I)^{-1}$ to $x^{(k)}$, we will get the approximation to the eigenvector v_σ . This is the procedure implemented in step 8 of algorithm 4.3.

4.2.2. Iterative eigensolvers

Now that the main techniques used by iterative eigensolvers have been laid out, we can look at three general methods, which are the most commonly used ones.

Jacobi-Davidson

The Jacobi-Davidson method is a type of algorithm where at each iteration, the approximation to an eigenpair of matrix A is improved by correcting the eigenvector through the solution of a certain linear system, as we shall see shortly. Given an approximation (u, θ) of an eigenpair of matrix A , where u is the approximate eigenvector and θ is the approximate eigenvalue, if the residual

$$r = Au - \theta u \quad (4.31)$$

is ≈ 0 , then the eigenpair converged. Otherwise, we want to find a correction t such that

$$r = A(u + t) - (\theta + \delta\theta)(u + t) = 0. \quad (4.32)$$

Linearizing Equation (4.32) in t gives

$$(A - \theta I)t = -r, \quad (4.33)$$

to avoid singularity of this equation near convergence, since u approximately spans a subspace of the system's kernel $\ker(A - \theta I)$, and enrich the subspace search with a useful orthogonal correction, we project the problem onto the orthogonal subspace of u , which finally gives

$$(I - uu^\dagger)(A - \theta I)(I - uu^\dagger)t = -r \quad (4.34)$$

Although simple, this method is computationally efficient only by using preconditioning,

Algorithm 4.1 Jacobi-Davidson method

- 1: Choose normalised initial vectors $\{u_k\}$, set $V = [u_1, \dots, u_k]$
 - 2: **repeat**
 - 3: Compute eigenpair: $T = V^\dagger AV$, solve $Ty = \theta y$
 - 4: Set $u = Vy$, residual $r = Au - \theta u$
 - 5: **if** $\|r_k\| < \varepsilon \forall k$ **then**
 - 6: **return** (θ, u)
 - 7: **end if**
 - 8: Solve approximately $(I - u_k u_k^\dagger)(A - \theta I)(I - u_k u_k^\dagger)t_k = -r_k$ using preconditioned iterative solver, ensuring $t_k \perp u_k$
 - 9: Normalise: $v_k = t_k / \|t_k\|$
 - 10: Expand subspace, setting $V = [V, v]$
 - 11: **until** convergence for $k = 1, \dots, \text{nev}$
-

which is known to be unstable in many cases [80].

Lanczos

Lanczos algorithm [84] is probably the most used iterative eigensolver for hermitian matrices. It is a Krylov subspace search method, meaning the Rayleigh-Ritz procedure is done on a subspace formed as

$$\mathcal{K} = \{v_1, Av_1, A^2v_1, \dots, A^{k-1}v_1\} \quad (4.35)$$

which exploits the power iteration. After orthogonalizing the new approximation to the previous one and diagonalizing the small scale problem, we end up with the new best approximations to the eigenvectors of A . Lanczos is extremely efficient, memory- and

Algorithm 4.2 Lanczos Method

```

1: Choose normalised initial vector  $v_1$ , set  $\beta_0 = 0$ ,  $m =$  subspace size.
2: repeat
3:   for  $j = 1, 2, \dots, m$  do
4:      $w \leftarrow Av_j - \beta_{j-1}v_{j-1}$ 
5:      $\alpha_j \leftarrow v_j^*w$ 
6:      $w \leftarrow w - \alpha_jv_j$ 
7:      $\beta_j \leftarrow \|w\|$ 
8:     if  $\beta_j = 0$  then
9:       break
10:    end if
11:     $v_{j+1} \leftarrow w/\beta_j$ 
12:  end for
13:  Form tridiagonal matrix  $T_m = \text{tridiag}(\beta_{1:m-1}, \alpha_{1:m}, \beta_{1:m-1})$ 
14:  Compute eigen-decomposition  $T_m y_k = \theta_k y_k$ , for  $k = 1, \dots, \text{nev}$ 
15:  Form Ritz approximations  $x_k = V_m y_k$ , where  $V_m = [v_1, \dots, v_m]$ 
16:  Compute residual norms  $r_k = \|Ax_k - \theta_k x_k\|$  for all  $k$ 
17: until convergence for  $k = 1, \dots, \text{nev}$ 

```

CPU-wise for extremal eigenvalues, but this limits its applicability, as one may be interested in the inner portion of the eigenvalue spectrum, such in the case of Hartree–Fock–Bogoliubov (HFB). A shift-and-invert strategy would be unfeasible in the case of large scale problems, since all Lanczos steps need to be performed exactly to avoid instabilities, a well known problem in the Arnoldi generalisation [80].

LOBPCG

The last algorithm of this short list is LOBPCG, it is the newest and most sophisticated one of the three. Introduced by A. V. Knyazev in 1991 [85], it is a block, preconditioned conjugate gradient method, explicitly targeted at solving large-scale eigenvalue problems, and it has been used in modern solutions of the Schrödinger/KS equation in recent years [86–89]. We will not go into the details of LOBPCG, since GCG shares with it many aspects, like blocking and search directions calculation.

LOBPCG works very well for large scale problems, but it has limitations. On the one hand, it is not possible to arbitrarily select the portion of the matrix spectrum to calculate, which is required for problems where variational collapse happens, like in HFB or the Dirac equation, which manifests particle/antiparticle solutions [89]. To solve this, an additional

filtering step is required [88, 89], which introduces a computational cost in the algorithm. Lastly, LOBPCG may fail when poor conditioning is present or when high precision on the eigenvalues is required [90].

4.2.3. Generalised Conjugate Gradient

The Generalised Conjugate Gradient is an iterative eigensolver designed with the aim of improving LOBPCG, it is a blocked algorithm, which uses the inverse power method and previous search directions to generate the search subspace. GCG is proven to be faster and more stable than LOBPCG [90]. The search subspace is built as

$$V = [X, P, W], \quad (4.36)$$

where X , of dimensions $n \times k$ is the matrix containing the approximations to the eigenvectors of matrix A , P , of dimensions $n \times k$ is the matrix containing the previous search directions, and W , of dimension $n \times a$ is the matrix containing the eigenvectors on which the inverse power method is applied approximately using the CG.

A slightly different implementation of the algorithm is employed in the present work, detailed in algorithm 4.3, to improve applicability to HF calculations and reduce the computational cost.

Eigenvalue problem The original algorithm aims at solving the general eigenvalue problem $AX = \lambda BX$. Since in our case $B = I$, it is omitted from the procedure, reducing the computational cost of the algorithm, in particular, the one of the search direction block P . After orthonormalization of V , the columns of X are orthonormal as well and the calculation of P is given by

$$P = X_{\text{new}} - X(X^\dagger X_{\text{new}}), \quad (4.37)$$

which is the projection of X_{new} onto the orthogonal complement of X , used in step 12 of algorithm 4.3.

Complex matrix The algorithm has been generalised to the complex case, where the matrix is complex Hermitian and, as such, the transposition operation is replaced by the conjugate transpose.

Blocking The algorithm is designed to allow blocking of the eigenvectors, such that $X = [X_c, X_a, X_r]$, where X_c are the converged eigenvectors, X_a are the active eigenvectors on which we perform the inverse power iteration, with $\text{col}(X_a)$ being a fixed number, and X_r are the remaining eigenvectors, which are to be inserted in X_a as soon as some of its columns converge. This allows to save some computations by avoiding the expensive inverse power on pairs that have already converged. Since in a self-consistent calculation the matrix changes rapidly at each HF iteration, it is the case that the maximum number of iterations is reached before convergence of all eigenpairs, so we must work at all times on the remaining un converged eigenvectors. For this reason, we only implement the $X = [X_c, X_a]$ scheme, where the only distinction we make is between converged eigenvectors X_c and un converged ones X_a .

Orthogonalization The original paper [90] suggests an improved orthogonalization procedure; being beyond the scope of this work, the simpler Gram-Schmidt [91] orthogonalization is used in the present work.

Shift update The shift update is either fixed, in case of known spectrum, eg for HFB `shift = 0`, or adaptive [90], so that the inverse power step can find the lowest eigenvalues, using the update formula

$$\text{shift} = (\lambda_{\text{nev}} - 100\lambda_1)/99, \quad (4.38)$$

where λ_{nev} is the biggest eigenvalue of the RR procedure and λ_1 is the smallest of the active eigenpairs.

Preconditioning Since the use of a properly designed preconditioner is beyond the scope of this work, a simple diagonal preconditioner is used.

4.3. Code implementation details

In this last section regarding numerical methods, some important features about the actual code implementation of the HF method are discussed. Mainly, the implementation of the Augmented Lagrangian Method to enforce spatial constraints on the HF solution, the pseudocode of the entire self-consistent procedure, and the choice of optimal parameters for the functional minimisation.

Algorithm 4.3 Generalised Conjugate Gradient algorithm

- 1: **Input:** Matrix A of dimensions $n \times n$, number of desired eigenpairs nev , X_{guess} initial guess of dimensions $n \times k$, with $k \geq \text{nev}$, max_iter maximum iterations
- 2: Initialise block $X = [X_a] \leftarrow X_{\text{guess}}$ and X_c as an empty block
- 3: Initialise blocks P and W as empty blocks
- 4: Solve the Rayleigh Ritz problem $X^\dagger A X C = C \Lambda$
- 5: Update $X = XC$
- 6: Initialise **shift**, Initialise **iter** = 0
- 7: **while** $\text{col}(X_c) < \text{nev}$ and $\text{iter} < \text{max_iter}$ **do**
- 8: Solve approximately $(A + \text{shift} \cdot I)W = X_a \Lambda$ with some CG steps, initial value X_a to generate W as an approximation to $W = (A + \text{shift} \cdot I)^{-1} X_a \Lambda$
- 9: Orthogonalize $V = [X, P, W]$, of dimensions $n \times (k + k + a)$
- 10: Solve the Rayleigh Ritz problem $V^\dagger (A + \text{shift} \cdot I) V C = C \Lambda$
- 11: Update X_{new} with the first nev columns of VC and $\Lambda_{\text{new}} = \Lambda - \text{shift} \cdot I$
- 12: Compute $P = X_{\text{new}} - X(X^\dagger X_{\text{new}})$
- 13: Compute the residual $R = AX_{\text{new}} - \Lambda X_{\text{new}}$
- 14: Check convergence on k -th column norm of R , if $\|R_k\| < \text{tol}$, move $X_{a,k}$ to X_c .
- 15: Update **shift** using formula (4.38) and $\text{iter} \leftarrow \text{iter} + 1$
- 16: **end while**
- 17: **Output:** Approximate eigenpairs (Λ, X)

4.3.1. Constraints

The purpose of spatial constraints is to find the minimum of the energy functional under the condition that the expectation value of a given operator \mathcal{Q} equals a prescribed target value q_0 . Constrained calculations are a fundamental tool to assess the stability of the ground-state minimum and to investigate dynamical properties of the nucleus, such as fission barriers [92].

Constraints can be formulated as an equality-constrained optimisation problem (ECP), formulated as

$$\begin{aligned} & \min_{|\Psi\rangle} E \\ & \text{constrained to } \langle \Psi | \mathcal{Q} | \Psi \rangle = \langle \mathcal{Q} \rangle = q_0. \end{aligned} \tag{4.39}$$

Which yields the Lagrangian

$$E' = E + \lambda(\langle \mathcal{Q} \rangle - q_0), \tag{4.40}$$

where λ is a Lagrange multiplier determined by the condition $\langle \mathcal{Q} \rangle = q_0$. After finding the

minimum of E' , it is trivial to show that for a given λ , we get [93]

$$\frac{dE}{d\langle Q \rangle} = -\lambda. \quad (4.41)$$

From a numerical standpoint, λ needs to be tuned at each iteration to reach the desired value of q_0 . This method was the one used in early constrained Hartree–Fock calculations [94]. Although this method is simple, it often fails. Moreover, for the same value of λ , many, possibly infinite values of $\langle Q \rangle$ can be obtained, for which we are only allowed to get the one with the most stable solution.

A different method is provided by the Quadratic Penalty Method (QPM). Briefly speaking, instead of a Lagrange multiplier, we add a quadratic contribution to the functional, such that

$$E' = E + \frac{c}{2}(\langle Q \rangle - q_0)^2. \quad (4.42)$$

This is a straightforward method; intuitively one penalises (hence the name), any solution for which $\langle Q \rangle \neq q_0$ by increasing its energy. However, the success of such procedure is heavily influenced by the choice of c , often leading to instabilities for large values. What happens is that for small values of c , the penalty may be insufficient to reach the target q_0 , while for bigger values, the penalty may be so strong that the self-consistent calculation oscillates and fails.

Augmented Lagrangian Method

A modern, robust approach, used by HF/HFB codes [44, 95] is given in the form of the Augmented Lagrangian Method (ALM) [96]. Its main idea is to combine the precision of the ECP with the accuracy of the QPM. Without delving into cumbersome mathematical details, we'll see how the algorithm is practically implemented in the code.

Given the functional

$$E' = E + \lambda(q - q_0) + \frac{c}{2}(q - q_0)^2, \quad (4.43)$$

where $q = \langle Q \rangle$, the resulting mean-field potential will be given by

$$U' = U + \lambda Q + c(q - q_0)Q \quad (4.44)$$

$$= U + c(q - q_0(\lambda))Q, \quad (4.45)$$

where $q_0(\lambda)$ is updated at each iteration with the formula

$$q_0(\lambda) = q_0 - \frac{\lambda}{c}, \quad (4.46)$$

$$\lambda^{(i+1)} = \lambda^{(i)} + \mu c(q - q_0). \quad (4.47)$$

Here, a slight deviation from the original ALM is present. Since the original work [96] doesn't provide guidance regarding what is considered an *iteration*, we employ the strategy [44] of using a damping factor $\mu \in [0, 1]$, so λ can be updated at each HF iteration for fast convergence, without large oscillations or instabilities of any kind.

This method is what powers the deformation curves that are shown in Chapter 6, allowing to explore the energy surface with arbitrary precision in reaching the value of q_0 at convergence, provided that enough HF iterations are performed. Note that, since $\lambda^{(0)} = 0$, for $\mu = 0$ ALM reduces to the standard QPM.

4.3.2. Details on the implementation of the code

The whole Hartree–Fock framework presented up to this point, has been implemented using the C++ language [97] and the Eigen library [98], which implements linear algebra operations through low level routines such as LAPACK and BLAS. In Figure 4.2, the schematics of the program structure is reported.

4.3.3. Optimal parameters choice

Inside the ‘Diagonalise h ’ step in Figure 4.2, the execution of the GCG algorithm is performed, using the current iteration’s single-particle Hamiltonian as the matrix to diagonalise and the previous iteration’s orbitals as the initial guess. This is the main computational bottleneck of the code, where a correct choice of the execution parameters can drastically reduce execution times. The parameters that need to be chosen carefully are essentially the inverse power step tolerance and the number of maximum GCG iterations.

Inverse power step tolerance

The first parameter to be tuned is the tolerance on the CG step which approximately solves the system

$$(A + \text{shift} \cdot I)W = X_a\Lambda \quad (4.48)$$

in algorithm 4.3, where A is actually the single-particle Hamiltonian h . When the CG residual $(A + \text{shift} \cdot I)W - X_a\Lambda$ is smaller than the tolerance, the procedure stops and

outputs the W block.

In Figure 4.3, the relative absolute error of the total energy is calculated against a reference benchmark value (details in the results Chapter 5), for different values of the CG tolerance. It is clear that at least a tolerance of 10^{-3} is needed for good convergence, while tolerances $\geq 10^{-4}$ stop offering increasing returns, rendering a choice between 10^{-4} and 10^{-5} an optimal one.

Inner GCG iterations

The number of inner GCG maximum iterations, here named ‘inverse power steps’ to avoid confusion, is slightly more nuanced than the CG tolerance. The algorithm converges to the true eigenpairs as the power steps are performed, so one could think that a higher number of steps would bring to HF convergence faster, since the precision on the eigenvalues increases, but this is not the case. In Figures 4.4 and 4.5, the convergence of the HF calculation is plotted for different number of steps, respectively, for the spherical nucleus ^{16}O and the deformed nucleus ^{24}Mg .

It is evident that in both cases, a steps number greater than 3 leads to oscillating behaviour near convergence, without accelerating it, while in the case of the spherical nucleus, just one step is enough to quickly, and reliably reach convergence. In any case, it is clear that delaying the inverse power steps to later HF iterations is safer in terms of stability. This counter intuitive behaviour is likely due to the fact that at each HF iteration the hamiltonian changes and a great number of steps leads to solutions too biased towards the current matrix eigenpairs, at the expense of the next iteration; however, in the case of deformed nuclei, due to sharp shape changes at the start of the calculation, just one step may not be enough to sustain the pace at which the Hamiltonian changes, hence the quicker convergence with more steps.

4.3.4. Numerical stability

As a final remark, the numerical stability of the solver is reported in Figure 4.6. The map is produced for a spherical calculation of ^{16}O , with varying box and mesh sizes. It is possible to observe that for a box whose side is at least ≈ 2.5 times the nuclear radius, the solver numerical stability is loosely dependent on the box extension, but rather on the step size. This is not surprising, as the points separation in space h dictates the precision of the discretised derivatives, as mentioned in Section 4.1.

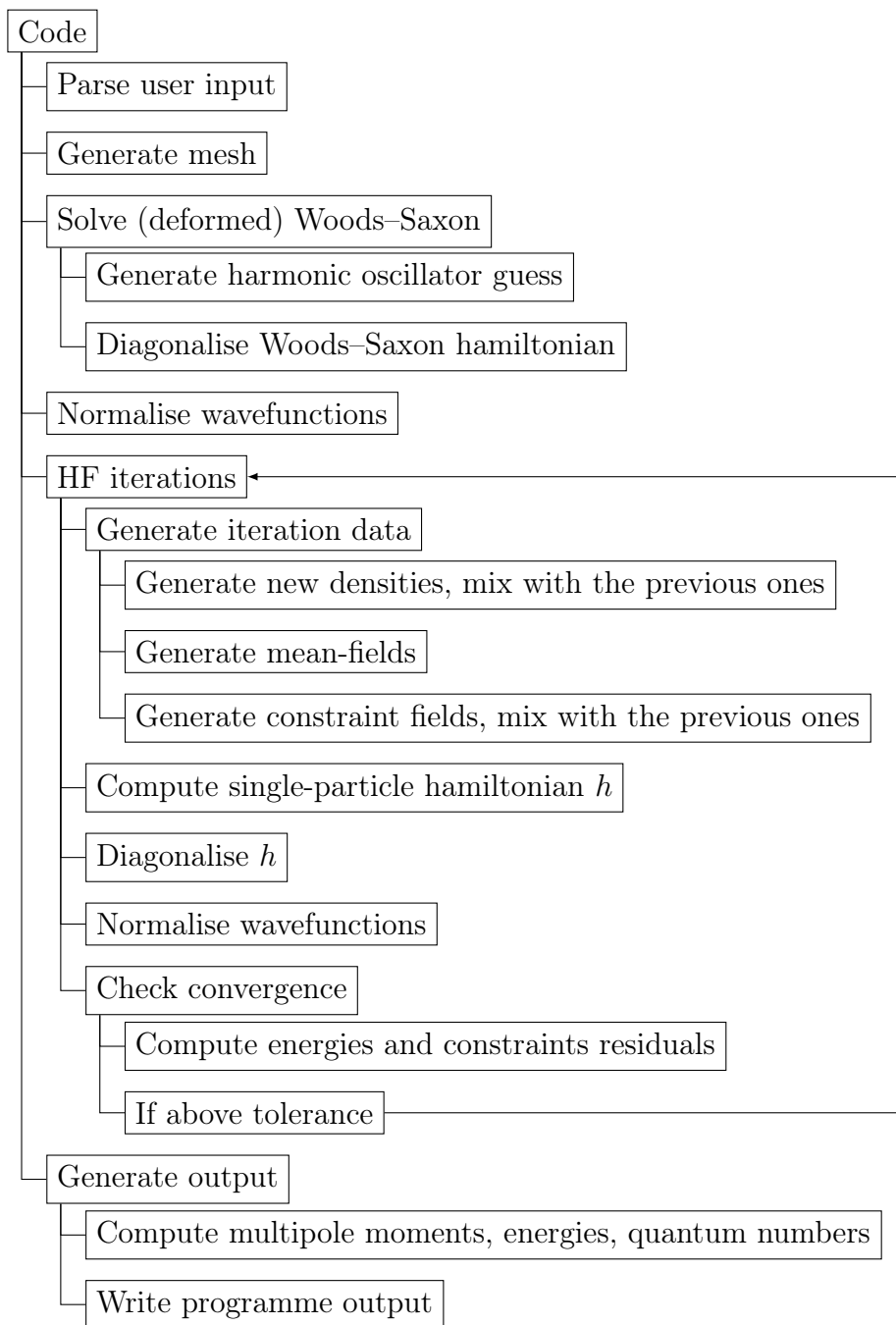


Figura 4.2: Pseudocode of the Hartree-Fock program.

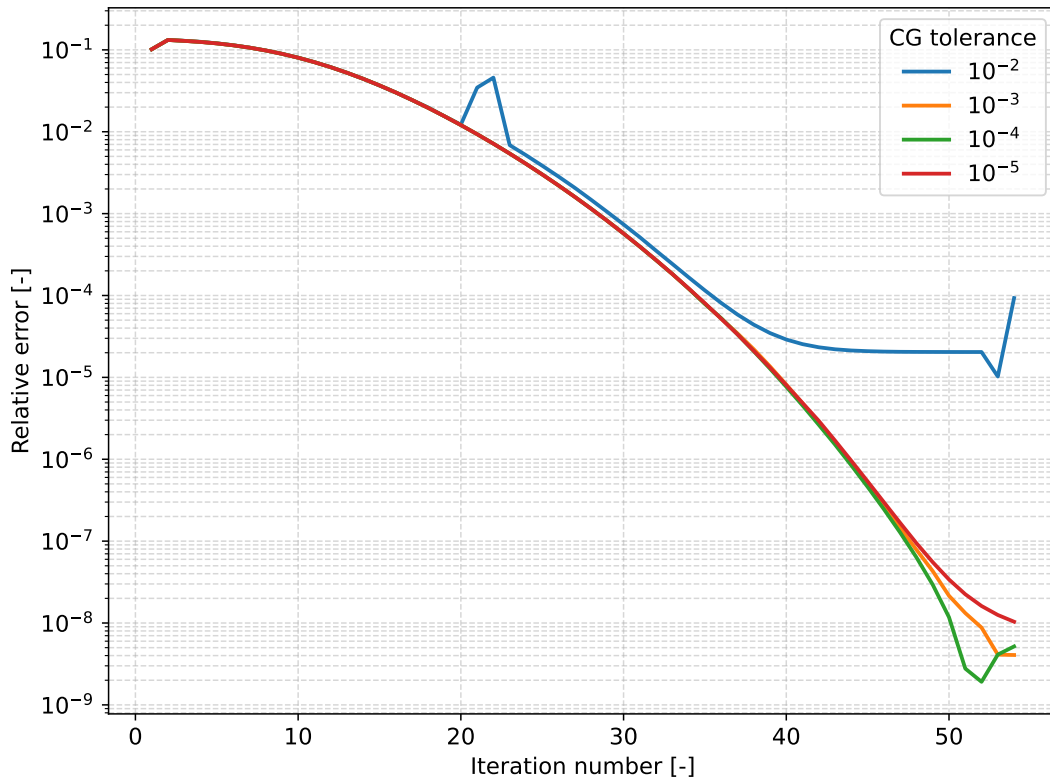


Figura 4.3: HF calculation convergence with varying CG tolerance for ^{16}O , box $[-9, +9]$ fm, step size 0.3 fm.

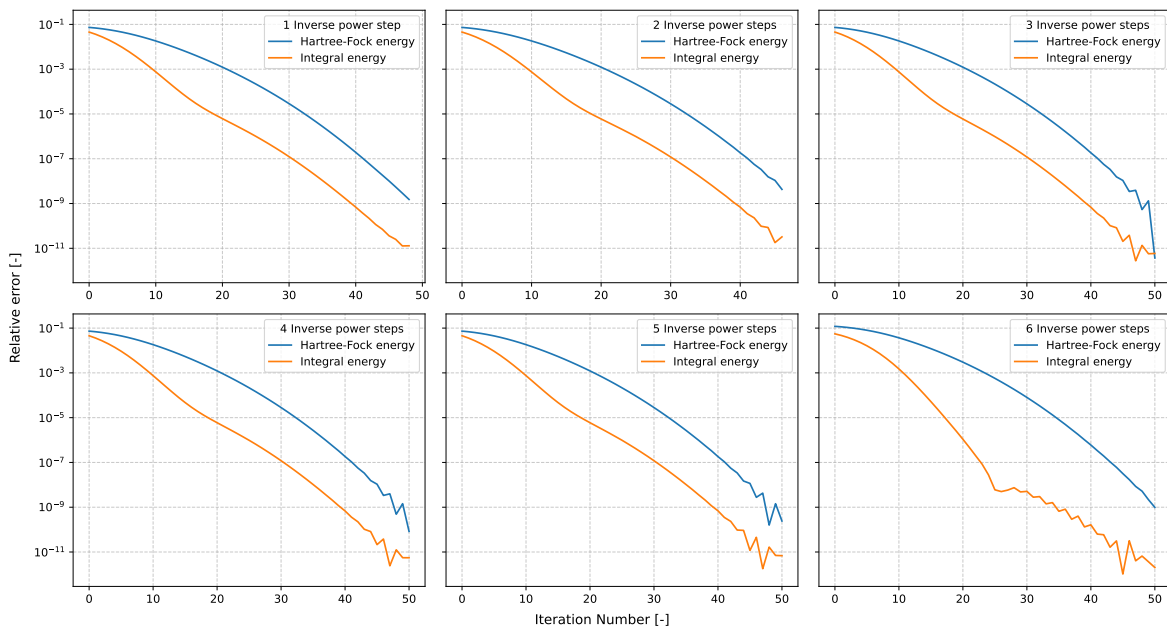


Figura 4.4: HF calculation convergence with varying number of inverse power steps for ^{16}O , box $[-9, +9]$ fm, step size 0.3 fm.

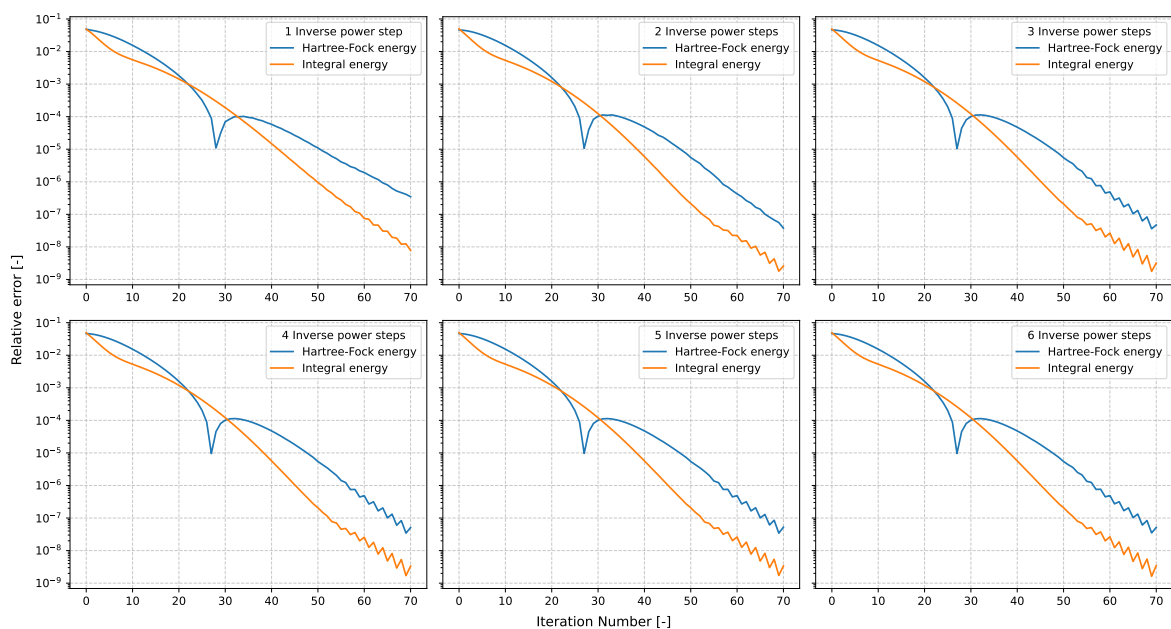


Figura 4.5: HF calculation convergence with varying number of inverse power steps for the deformed nucleus ^{24}Mg , box $[-10, +10]$ fm, step size 0.33 fm.

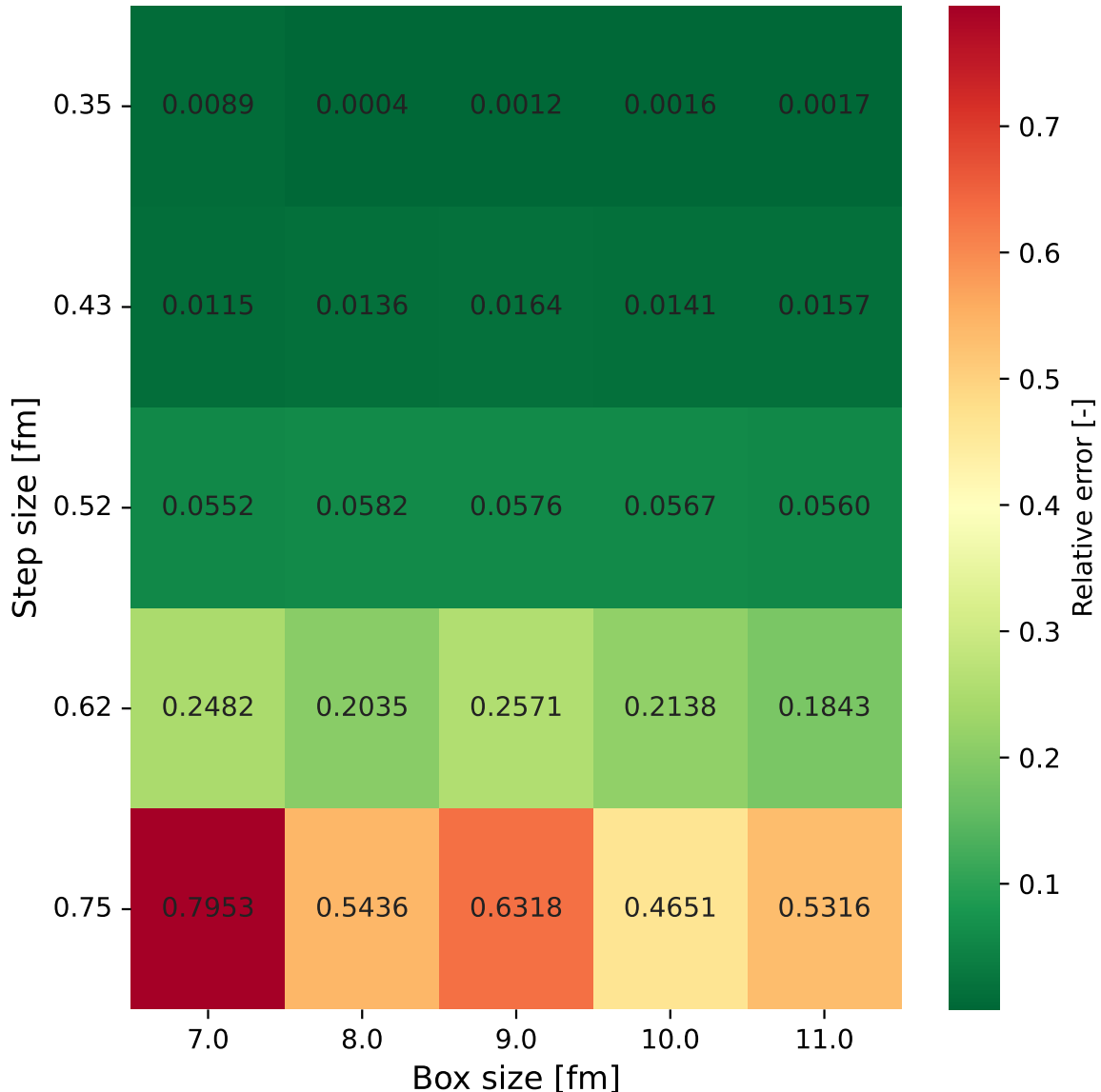


Figura 4.6: Numerical stability map of the HF solver for ^{16}O for different box and step sizes. Relative error is taken against a benchmark reference value.

5 | Results for spherical nuclei

In this chapter, results for spherical nuclei are presented. These are calculated for doubly magic nuclei, with the exception of ^{90}Zr , since a pairing interaction is not implemented in the present work. The reason behind choosing spherical nuclei as an initial benchmark is that spherical codes have the advantage of assuming quantities to be dependent only on the radial coordinate, ie they are 1D. The low dimensionality allows the use of very fine meshes, with a step size that can go down to the order of ~ 0.1 fm, without significant computational overhead. We can use these codes as a reference ideal value for the different quantities produced by our code in the case of spherical nuclei. The choice for benchmarking spherical results in the present work has been the `hfbcsl_qrpa` code [42].

This chapter is organised as follows. Section 5.1 introduces the evaluation of mean-square radii used to numerically validate the code. Section 5.2 introduces the calculation parameters, Section 5.3 presents benchmark results for ^{16}O , and Section 5.4 extends the analysis to the heavier nuclei ^{48}Ca , ^{56}Ni , and ^{90}Zr .

5.1. Physical quantities

After finding the energy minimum of the functional, we are able to compute different physical properties of the system. We can use these values as a numerical reference when comparing our results with other codes.

5.1.1. Mean square radii

An important set of quantities characterising the nuclear density are certainly the mean square radii. The individual nuclear species' mean square radius is defined as

$$\langle r_q^2 \rangle = \frac{\int \rho_q(\mathbf{r}) r^2 d\mathbf{r}}{\int \rho_q(\mathbf{r}) d\mathbf{r}}. \quad (5.1)$$

The charge mean square radius formula is derived from the convolution of the neutron and proton particle densities with their respective internal charge distribution [99], which

yields

$$\langle r_{ch}^2 \rangle = \langle r_p^2 \rangle + \langle r_N^2 \rangle_P + \frac{N}{Z} \langle r_N^2 \rangle_N + \frac{2}{Z} \left(\frac{\hbar}{mc} \right)^2 \sum_{\alpha q} \mu_q \langle \boldsymbol{\sigma} \cdot \boldsymbol{\ell} \rangle_{\alpha q} \quad (5.2)$$

where q runs over the nuclear species and α runs over all single particle states of species q . The vector $\boldsymbol{\sigma}$ is the vector operator of Pauli matrices, while $\boldsymbol{\ell}$ is the angular momentum operator $-i(\mathbf{r} \times \nabla)$. $\langle r^2 \rangle_P$ and $\langle r^2 \rangle_N$ refer to the square charge radii of the proton and the neutron, while μ_q to their respective magnetic dipole moment in units of nuclear magneton μ_N . All square charge radii computed in this work use the set of parameters in Table 5.1, taken to be equal to the spherical benchmark code `hfbcsl_qrpa`.

Parameter	Value	Units
$\langle r^2 \rangle_P$	0.64	fm ²
$\langle r^2 \rangle_N$	-0.11	fm ²
μ_p	2.792847	μ_N
μ_n	-1.913043	μ_N

Tabella 5.1: Parameters used to compute the charge mean square radius. Values are taken from [68].

5.2. Parameters and mesh choice

All `hfbcsl_qrpa` calculations were performed using a mesh size of 0.1 fm, no pairing interaction, and a radial mesh size whose radius is equal to the size of the box in our computation. The lattice of our code depends on the extension of the nucleus, which is directly determined by its mass A ; since the number of subdivisions that allows reasonable CPU times on a standard laptop caps around 60 – 70, step sizes vary across different calculations. In the results shown here, for ^{16}O , we are able to reach a 0.3 fm step size, while for the heaviest, ^{90}Zr , we are only able to reach 0.42 fm. The reason behind this choice is that as the nucleus size increases, a bigger box is needed to ensure that all relevant states are able to decay to zero at the boundary. All the data reported in this chapter is computed with the SLy5 parametrisation [72].

5.3. Results for ^{16}O

The first results we will take a look at are the ones for ^{16}O . It is an ideal benchmark for gauging the solver’s performance, as it is a very light, double magic nucleus, meaning it has no pairing and a spherical shape. All calculations are performed in a box of size

$[-9, +9]$ fm in all three directions and a step size of 0.3 fm, corresponding to $2 \cdot 60^3$ mesh points.

5.3.1. Results neglecting Coulomb interaction

Since the Skyrme functional includes many terms of increasing complexity, results are shown for more and more terms in expression (3.104). We start by including only C_0^ρ , C_1^ρ , C_0^τ , C_1^τ and neglecting the others, and the Coulomb interaction; results are reported in Table 5.2. Without further terms, the spin-orbit field $\mathbf{B}(\mathbf{r})$ (3.117) vanishes, hence the $1p_{3/2}$ and $1p_{1/2}$ levels show degeneration in energy.

Since $N = Z$, assuming equal masses the single-particle equations will be exactly equal between the two species, therefore only neutron values are reported. Note that C_1 terms vanish in this case, that is until we either break the $N = Z$ equality or introduce the Coulomb interaction.

Physical quantities					
		GCG	hfbcg_qrpa	Δ	$\Delta\%$
E_{TOT}	[MeV]	-141.582	-141.582	-	-
$\langle r_n^2 \rangle^{1/2}$	[fm]	2.6504	2.6510	0.0006	2.26×10^{-2}
$\langle r_{ch}^2 \rangle^{1/2}$	[fm]	2.7486	2.7491	0.0005	1.82×10^{-2}

Neutron energy levels					
		GCG	hfbcg_qrpa	Δ	$\Delta\%$
$1s_{1/2}$	[MeV]	-36.142	-36.139	0.003	8.30×10^{-3}
$1p_{3/2}$	[MeV]	-18.573	-18.572	0.001	5.38×10^{-3}
$1p_{1/2}$	[MeV]	-18.573	-18.572	0.001	5.38×10^{-3}

Tabella 5.2: ^{16}O including C_0^ρ , C_1^ρ , C_0^τ , C_1^τ terms and neglecting the Coulomb interaction. Δ refers to the difference between the two codes in absolute value, while $\Delta\%$ refers to the relative difference in percent.

In Table 5.3 the $C_0^{\nabla \cdot J}$ and $C_1^{\nabla \cdot J}$ terms are included just for the spin-orbit field $\mathbf{B}(\mathbf{r})$, but not for the mean-field $U(\mathbf{r})$; it is as if we were neglecting the J^2 terms in the energy density [72]. As expected, the $1p_{3/2}$ and $1p_{1/2}$ degeneration is removed, displaying the spin-orbit splitting, which lowers the total angular momentum $j = 3/2$ level and raises the $j = 1/2$ level.

Physical quantities					
		GCG	hfbcsl_qrpa	Δ	$\Delta\%$
E_{TOT}	[MeV]	-142.080	-142.080	-	-
$\langle r_n^2 \rangle^{1/2}$	[fm]	2.6516	2.6516	-	-
$\langle r_{ch}^2 \rangle^{1/2}$	[fm]	2.7497	2.7497	-	-

Neutron energy levels					
		GCG	hfbcsl_qrpa	Δ	$\Delta\%$
1s _{1/2}	[MeV]	-36.314	-36.312	0.002	5.5×10^{-3}
1p _{3/2}	[MeV]	-20.696	-20.696	-	-
1p _{1/2}	[MeV]	-14.335	-14.335	-	-

Tabella 5.3: ^{16}O including C_0^ρ , C_1^ρ , C_0^τ , C_1^τ , $C_0^{\nabla \cdot J}$, $C_1^{\nabla \cdot J}$ terms, neglecting the Coulomb interaction and J^2 terms. Δ refers to the difference between the two codes in absolute value, while $\Delta\%$ refers to the relative difference in percent.

Lastly, the $C_0^{\nabla \cdot J}$ and $C_1^{\nabla \cdot J}$ terms are also included in the calculation of the mean-field, resulting in the full implementation of the Skyrme functional. As shown in Table 5.4, the effect of this addition on the ground state is little, as the spin current $J_{\mu\nu}$ is small in light, closed shell nuclei.

5.3.2. Results including Coulomb interaction

As the final step to get a complete description of ^{16}O , the Coulomb interaction is included as detailed in Section 3.5. Results are shown in Table 5.5.

As shown in tables 5.2, 5.3, 5.4, and 5.5 results for ^{16}O are in good agreement with the output of the `hfbcsl_qrpa` code for all the terms in the energy functional.

5.4. Results for heavier nuclei

In the following section, results for some spherical nuclei heavier than ^{16}O are presented. ^{48}Ca in Table 5.6, ^{56}Ni in Table 5.7, and ^{90}Zr in Table 5.8. Our code still shows good agreement with the `hfbcsl_qrpa` one. A slight increase of the numerical error can be observed as the step size increases, which is compatible with the polynomial error in the finite difference method. The increase of the cubic box size is necessary to accomodate larger nuclei, due to the increase in volume occupied, as to guarantee that less bound states decay to zero at the boundary. Running the code on HPC computers or clusters

Physical quantities					
		GCG	hfbcsl_qrpa	Δ	$\Delta\%$
E_{TOT}	[MeV]	-142.074	-142.074	-	-
$\langle r_n^2 \rangle^{1/2}$	[fm]	2.6515	2.6516	0.0001	3.77×10^{-3}
$\langle r_{ch}^2 \rangle^{1/2}$	[fm]	2.7497	2.7497	-	-

Neutron energy levels					
		GCG	hfbcsl_qrpa	Δ	$\Delta\%$
1s _{1/2}	[MeV]	-36.309	-36.308	0.001	2.75×10^{-3}
1p _{3/2}	[MeV]	-20.684	-20.685	0.001	4.83×10^{-3}
1p _{1/2}	[MeV]	-14.361	-14.361	-	-

Tabella 5.4: ^{16}O neglecting the Coulomb interaction. Δ refers to the difference between the two codes in absolute value, while $\Delta\%$ refers to the relative difference in percent.

would enable the use of finer meshes, ie more lattice points, a smaller step size and an increase in the numerical precision.

5.5. Comparison with experimental values

The Skyrme functional is highly successful at producing theoretical values in great accordance with experimental data, just by fitting a small set of parameters [6]. In Table 5.9, binding energies of some of the spherical nuclei presented so far are compared with experimental values, taken from the Atomic Mass Data Center [25].

Physical quantities

		GCG	hfbcsl_qrpa	Δ	$\Delta\%$
E_{TOT}	[MeV]	-128.402	-128.400	0.002	1.56×10^{-3}
$\langle r_n^2 \rangle^{1/2}$	[fm]	2.6584	2.6585	0.0001	3.76×10^{-3}
$\langle r_p^2 \rangle^{1/2}$	[fm]	2.6835	2.6836	0.0001	3.73×10^{-3}
$\langle r_{ch}^2 \rangle^{1/2}$	[fm]	2.7805	2.7803	0.0002	7.19×10^{-3}

Neutron energy levels

		GCG	hfbcsl_qrpa	Δ	$\Delta\%$
1s _{1/2}	[MeV]	-36.140	-36.137	0.003	8.30×10^{-3}
1p _{3/2}	[MeV]	-20.611	-20.611	-	-
1p _{1/2}	[MeV]	-14.427	-14.428	0.001	6.93×10^{-3}

Proton energy levels

		GCG	hfbcsl_qrpa	Δ	$\Delta\%$
1s _{1/2}	[MeV]	-32.349	-32.345	0.004	1.24×10^{-2}
1p _{3/2}	[MeV]	-17.137	-17.137	-	-
1p _{1/2}	[MeV]	-11.081	-11.082	0.001	9.02×10^{-3}

Tabella 5.5: ^{16}O complete of the Skyrme functional and Coulomb interaction. Δ refers to the difference between the two codes in absolute value, while $\Delta\%$ refers to the relative difference in percent.

Physical quantities					
		GCG	hfbcsl_qrpa	Δ	$\Delta\%$
E_{TOT}	[MeV]	-415.955	-415.931	0.024	5.77×10^{-3}
$\langle r_n^2 \rangle^{1/2}$	[fm]	3.6106	3.6110	0.0004	1.11×10^{-2}
$\langle r_p^2 \rangle^{1/2}$	[fm]	3.4502	3.4507	0.0005	1.45×10^{-2}
$\langle r_{ch}^2 \rangle^{1/2}$	[fm]	3.5274	3.5060	0.0214	0.610

Neutron energy levels					
		GCG	hfbcsl_qrpa	Δ	$\Delta\%$
1s _{1/2}	[MeV]	-49.758	-49.752	0.006	1.21×10^{-2}
1p _{3/2}	[MeV]	-35.952	-35.949	0.003	8.34×10^{-3}
1p _{1/2}	[MeV]	-33.891	-33.891	-	-
1d _{5/2}	[MeV]	-22.170	-22.169	0.001	4.51×10^{-3}
2s _{1/2}	[MeV]	-17.720	-17.720	-	-
1d _{3/2}	[MeV]	-17.431	-17.434	0.003	1.72×10^{-2}
1f _{7/2}	[MeV]	-9.262	-9.261	0.001	1.08×10^{-2}

Proton energy levels					
		GCG	hfbcsl_qrpa	Δ	$\Delta\%$
1s _{1/2}	[MeV]	-45.936	-45.930	0.006	1.31×10^{-2}
1p _{3/2}	[MeV]	-34.314	-34.311	0.003	8.74×10^{-3}
1p _{1/2}	[MeV]	-30.482	-30.483	0.001	3.28×10^{-3}
1d _{5/2}	[MeV]	-22.455	-22.454	0.001	4.45×10^{-3}
2s _{1/2}	[MeV]	-16.753	-16.751	0.002	1.19×10^{-2}
1d _{3/2}	[MeV]	-15.337	-15.340	0.003	1.96×10^{-2}

Tabella 5.6: ^{48}Ca , box size $[-12, +12]$ fm, step size 0.34 fm. Δ refers to the difference between the two codes in absolute value, while $\Delta\%$ refers to the relative difference in percent.

Physical quantities

		GCG	hfbcslqrpa	Δ	$\Delta\%$
E_{TOT}	[MeV]	-482.805	-482.700	0.105	2.18×10^{-2}
$\langle r_n^2 \rangle^{1/2}$	[fm]	3.6422	3.6433	0.0011	3.02×10^{-2}
$\langle r_p^2 \rangle^{1/2}$	[fm]	3.6968	3.6979	0.0011	2.97×10^{-2}
$\langle r_{ch}^2 \rangle^{1/2}$	[fm]	3.7722	3.7682	0.0040	0.106

Neutron energy levels

		GCG	hfbcslqrpa	Δ	$\Delta\%$
1s _{1/2}	[MeV]	-54.277	-54.260	0.017	3.13×10^{-2}
1p _{3/2}	[MeV]	-41.571	-41.562	0.009	2.16×10^{-2}
1p _{1/2}	[MeV]	-39.613	-39.611	0.002	5.05×10^{-3}
1d _{5/2}	[MeV]	-28.536	-28.530	0.006	2.10×10^{-2}
2s _{1/2}	[MeV]	-23.539	-23.545	0.006	2.55×10^{-2}
1d _{3/2}	[MeV]	-23.367	-23.361	0.006	2.57×10^{-2}
1f _{7/2}	[MeV]	-16.019	-16.018	0.001	6.24×10^{-3}

Proton energy levels

		GCG	hfbcslqrpa	Δ	$\Delta\%$
1s _{1/2}	[MeV]	-43.754	-43.740	0.014	3.20×10^{-2}
1p _{3/2}	[MeV]	-31.561	-31.555	0.006	1.90×10^{-2}
1p _{1/2}	[MeV]	-29.545	-29.545	-	-
1d _{5/2}	[MeV]	-19.017	-19.016	0.001	5.26×10^{-3}
2s _{1/2}	[MeV]	-14.004	-14.012	0.008	5.71×10^{-2}
1d _{3/2}	[MeV]	-13.891	-13.887	0.004	2.88×10^{-2}
1f _{7/2}	[MeV]	-6.934	-6.935	0.001	1.44×10^{-2}

Tabella 5.7: ^{56}Ni , box size [-13,+13] fm, step size 0.37 fm. Δ refers to the difference between the two codes in absolute value, while $\Delta\%$ refers to the relative difference in percent.

Physical quantities					
		GCG	hfbcs_qrpa	Δ	$\Delta\%$
E_{TOT}	[MeV]	-783.587	-783.325	0.262	3.34×10^{-2}
$\langle r_n^2 \rangle^{1/2}$	[fm]	4.2854	4.2872	0.0018	4.20×10^{-2}
$\langle r_p^2 \rangle^{1/2}$	[fm]	4.2196	4.2212	0.0016	3.79×10^{-2}
$\langle r_{ch}^2 \rangle^{1/2}$	[fm]	4.2767	4.2704	0.0063	0.148
Neutron energy levels					
		GCG	hfbcs_qrpa	Δ	$\Delta\%$
1s _{1/2}	[MeV]	-55.636	-55.615	0.021	3.78×10^{-2}
1p _{3/2}	[MeV]	-45.324	-45.309	0.015	3.31×10^{-2}
1p _{1/2}	[MeV]	-44.172	-44.160	0.012	2.72×10^{-2}
1d _{5/2}	[MeV]	-34.148	-34.137	0.011	3.22×10^{-2}
2s _{1/2}	[MeV]	-31.393	-31.391	0.002	6.37×10^{-3}
1d _{3/2}	[MeV]	-29.802	-29.797	0.005	1.68×10^{-2}
1f _{7/2}	[MeV]	-22.755	-22.748	0.007	3.08×10^{-2}
2p _{3/2}	[MeV]	-17.837	-17.840	0.003	1.68×10^{-2}
1f _{5/2}	[MeV]	-17.568	-17.563	0.005	2.85×10^{-2}
2p _{1/2}	[MeV]	-15.729	-15.723	0.006	3.82×10^{-2}
1g _{9/2}	[MeV]	-11.586	-11.580	0.006	5.18×10^{-2}
Proton energy levels					
		GCG	hfbcs_qrpa	Δ	$\Delta\%$
1s _{1/2}	[MeV]	-44.973	-44.956	0.017	3.78×10^{-2}
1p _{3/2}	[MeV]	-36.347	-36.336	0.011	3.03×10^{-2}
1p _{1/2}	[MeV]	-34.121	-34.115	0.006	1.76×10^{-2}
1d _{5/2}	[MeV]	-26.766	-26.759	0.007	2.62×10^{-2}
2s _{1/2}	[MeV]	-22.175	-22.178	0.003	1.35×10^{-2}
1d _{3/2}	[MeV]	-21.216	-21.214	0.002	9.43×10^{-3}
1f _{7/2}	[MeV]	-16.722	-16.718	0.004	2.39×10^{-2}
2p _{3/2}	[MeV]	-10.239	-10.236	0.003	2.93×10^{-2}
1f _{5/2}	[MeV]	-9.613	-9.618	0.005	5.20×10^{-2}
2p _{1/2}	[MeV]	-8.108	-8.104	0.004	4.94×10^{-2}

Tabella 5.8: ^{90}Zr , box size $[-15, +15]$ fm, step size 0.43 fm. Δ refers to the difference between the two codes in absolute value, while $\Delta\%$ refers to the relative difference in percent.

	^{16}O	^{48}Ca	^{56}Ni	^{90}Zr
E_{th} (MeV)	128.40	415.95	482.80	783.59
E_{exp} (MeV)	127.62	414.33	483.99	783.89
$r_{\text{ch, th}}$ (fm)	2.781	3.527	3.772	4.277
$r_{\text{ch, exp}}$ (fm)	2.699	3.477	3.763	4.269

Tabella 5.9: Comparison of experimental binding energies and charge radii with theoretical values calculated using the SLy5 functional. Data taken from [72, 100].

6 | Results for deformed nuclei

Having established that the code works as expected for spherical nuclei, we can extend the calculations to deformed systems. In this chapter, the GCG implementation is validated against well-established deformed codes. In addition, we also present some new original results with a focus on α -clustering and nuclei near the drip lines.

This chapter is organised as follows. First, in Section 6.1, the quadrupole deformation parameter β_2 is introduced and its two different definitions are compared. In Section 6.2, results for the deformed nucleus ^{24}Mg are presented and used as a benchmark for the performance of our code, first against the HO basis expansion code **HFBTHO** in Section 6.2.1, second against the Cartesian mesh code **EV8** in Section 6.2.2. Finally, in Section 6.3, original results on other deformed nuclei are discussed, in particular: in Section 6.3.1 results regarding an alpha-clustering study in ^{20}Ne , and in Section 6.3.2 results for the near-drip line nuclei ^{42}Si and ^{28}S .

6.1. Deformation parameters

When dealing with deformed nuclei, mean square radii are not sufficient to characterise the nuclear density. The main quantity used is the quadrupole deformation parameter β_2 , similar to the one encountered in Section 1.3. There is an ambiguity in its definition in literature, because some [50] compute it by using the actual mean square radius of the density

$$\beta_2 = \frac{4\pi \langle \mathcal{Q}_{20} \rangle}{5A \langle r^2 \rangle}, \quad (6.1)$$

where $\langle r^2 \rangle$ is the total mean square radius of the nucleus

$$\langle r^2 \rangle = \frac{\int (\rho_n + \rho_p) r^2 d\mathbf{r}}{\int (\rho_n + \rho_p) d\mathbf{r}} = \langle x^2 + y^2 + z^2 \rangle, \quad (6.2)$$

while others [14, 101] normalise the quadrupole moment with respect to the parametrised nuclear radius in formula (1.6), which yields

$$\beta_2 = \frac{4\pi \langle Q_{20} \rangle}{3AR^2}, \quad (6.3)$$

where the relation

$$\langle r^2 \rangle = \frac{3}{5}R^2 \quad (6.4)$$

is used and the value for r_0 is taken to be 1.2 fm.

Using either of the two formulae (6.1, 6.3), because of the normalization with respect to the total radius and mass, it allows comparing the parameter β_2 across the nuclear chart, at variance with $\langle Q_{20} \rangle$ which depends on mass and radius.

In Figure 6.1, a comparison between the two formulae is presented; as shown by the shape of the curves, it is possible to observe that the normalisation of β_2 with respect to the real radius has an asymptotic behaviour for large deformations, since for $\langle z^2 \rangle \rightarrow \infty$, assuming axial symmetry and constant volume V

$$\beta_2 \propto \frac{2z^2 - 2V/z}{z^2 + 2V/z} \xrightarrow[z \rightarrow \infty]{} 2, \quad (6.5)$$

while normalising with respect to the parametrised radius R has no such asymptotic behaviour, since R is constant for any deformation.

The choice of β_2 used in the present work is the one computed with the parametrised radius (6.3). To avoid confusion in the reader and present results in a consistent manner, when comparing results with the HFBTHO code, which uses formula (6.1), the bare quadrupole moment $\langle Q_{20} \rangle$ is shown instead.

6.1.1. Code parameters and axial constraint

As for our code, calculations are performed in a box $[-10, +10]$ fm. In the case of the ground state calculation, a step size of 0.33 fm is used, with a starting guess of a deformed Woods–Saxon with $\beta_2 = 0.4$.

The calculation in the case of the deformation curve is carried out imposing the following constraints:

$$\langle \text{Re } Q_{22} \rangle = \langle \text{Im } Q_{22} \rangle = 0, \quad (6.6)$$

$$\langle x \rangle = \langle y \rangle = \langle z \rangle = 0, \quad (6.7)$$

$$\langle Q_{20} \rangle = q_{20}. \quad (6.8)$$

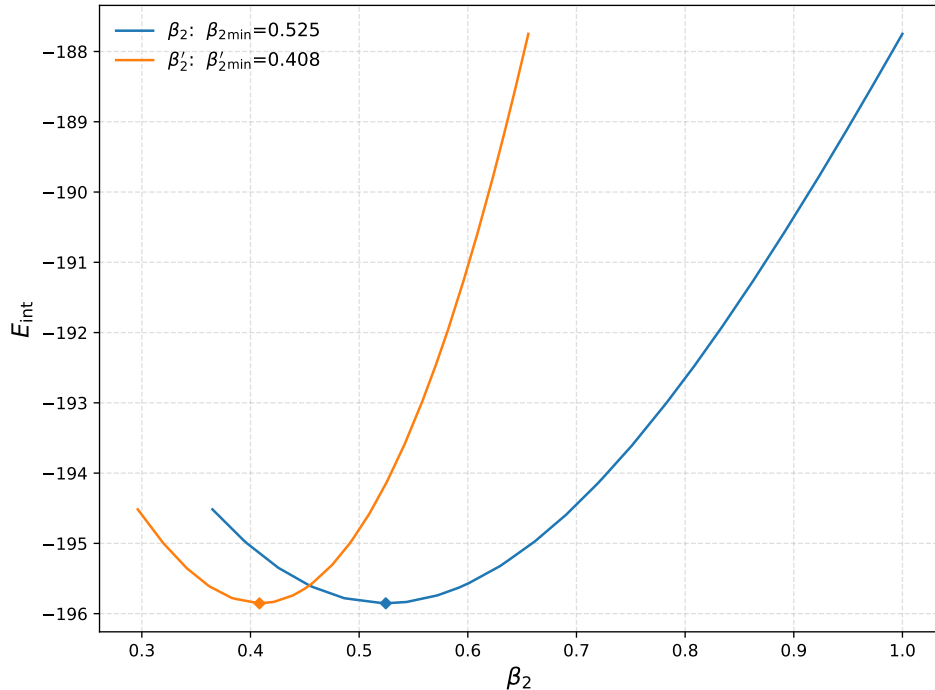


Figura 6.1: Comparison between the two formulae for β_2 in a deformation curve for ^{24}Mg . β'_2 refers to the deformation parameter normalised by the parametrised radius, while β_2 refers to the deformation parameter normalised by the actual mean square radius.

These constraints altogether impose an axial deformation on the system, the constraint on $\langle Q_{20} \rangle$ alone is not sufficient because on an unconstrained mesh like in our case, the nucleus may deform on a different axis from the chosen one (z) or the $\langle Q_{20} \rangle$ moment may be subject to spurious contributions from a centre of mass not in the origin; moreover, the axial symmetry of HFBTHO doesn't allow broken axial symmetry configurations.

Regarding the stiffness c and damping parameter μ of the ALM described in Section 4.3.1, $c = 0.005$ and $\mu = 0.02$ were used. As for convergence criteria, a tolerance of 0.001 on the value of $\beta_2 - \beta_{2,\text{target}}$ was used.

6.2. Benchmark for ^{24}Mg

In the following section, results for ^{24}Mg are presented and used as a benchmark for the performance of our code in a deformed case. ^{24}Mg is a light, deformed nucleus, in which pairing correlations are negligible in its ground state and for deformations around it [101].

In Section 6.2.1, the axially symmetric HO basis code HFBTHO is used, since it is a well-established code for axial calculations. We will compare results regarding the ground

state. In Section 6.2.2, a comparison of the deformation curve is presented using the Cartesian mesh code EV8.

6.2.1. HFBTHO code and calculation details

To benchmark the code against a basis expansion method in the case of nuclear deformation, the HFBTHO code was used [50]: this is a HFB solver which minimises the energy functional on a harmonic oscillator basis. Since ^{24}Mg is a light, well-bound nucleus, it still works well in this case. All calculations were carried out using 12 oscillator shells and neglecting pairing. Since the version of HFBTHO used in this work has been compiled with the J^2 terms disabled, we present the results from our code both with and without them. The results obtained without them serve as a benchmark for the code, while those including the J^2 contribution illustrate its impact on the ground state.

Ground state

Table 6.1 reports data of the comparison with HFBTHO for the ground state of ^{24}Mg . In Figure 6.2 contours of the density at $y = 0$ are shown, while in Figure 6.3 the density viewed ‘from the top’, ie on $z = 0$ is shown. As remarked by the density contours, the ground state is axially symmetric, quadrupole deformed, and parity-conserving.

Charge radii for the two codes are displayed but not compared, due to different formulas used for their computation. $\langle x^2 \rangle$, $\langle y^2 \rangle$ and $\langle z^2 \rangle$ are reported for our code but not for HFBTHO since it does not compute them.

		GCG	GCG no J^2	HFBTHO	Δ	$\Delta\%$
E_{TOT}	[MeV]	-195.854	-197.219	-197.030	0.189	9.52×10^{-2}
$\langle r_n^2 \rangle^{1/2}$	[fm]	3.0124	2.9998	2.9996	0.0002	6.67×10^{-3}
$\langle r_p^2 \rangle^{1/2}$	[fm]	3.0475	3.0346	3.0326	0.0020	6.59×10^{-2}
$\langle r_{ch}^2 \rangle^{1/2}$	[fm]	3.1364	3.1240	3.4614	-	-
$\langle z^2 \rangle^{1/2}$	[fm]	2.145	2.128	-	-	-
$\langle x^2 \rangle^{1/2}$	[fm]	1.511	1.511	-	-	-
$\langle y^2 \rangle^{1/2}$	[fm]	1.514	1.514	-	-	-
$\langle Q_{20} \rangle$	[fm 2]	34.981	33.905	33.881	0.024	7.08×10^{-2}

Tabella 6.1: Results for ^{24}Mg ground state, no pairing interaction, box $[-10, +10]$ fm, step size 0.33 fm, SkM* parametrisation.

The comparison shows good agreement between the two codes, with ground state physical

properties, energies and $\langle Q_{20} \rangle$ that are comparable to each other.

In Table 6.2, the single-particle states energies are reported, to showcase the shift of the levels based on the angular momentum projection along the deformation axis m_j . As predicted by the Nilsson model, within the same sub-shell, levels that have a lower $|m_j|$ projection are lowered in energy, while those with a higher projection are raised, with respect to the degenerate spherical case. This is shown in the graphical representation of the levels splitting in the Nilsson model in Figure 1.5.

Neutron energy levels			Proton energy levels		
Shell	$ m_j $	E [MeV]	Shell	$ m_j $	E [MeV]
1s _{1/2}	1/2	-39.281	1s _{1/2}	1/2	-34.250
1p _{3/2}	1/2	-28.381	1p _{3/2}	1/2	-23.556
1p _{3/2}	3/2	-24.224	1p _{3/2}	3/2	-19.390
1p _{1/2}	1/2	-18.680	1p _{1/2}	1/2	-13.964
1d _{5/2}	1/2	-16.743	1d _{5/2}	1/2	-12.121
1d _{5/2}	3/2	-14.130	1d _{5/2}	3/2	-9.537

Tabella 6.2: Single-particle energy levels in the ground state of ^{24}Mg . As predicted by the Nilsson model, levels with a lower $|m_j|$ projection are lowered in energy, while those with a higher projection are raised, with respect to the spherical (degenerate) case.

6.2.2. EV8 code and calculation details

HFBTHO can be used to judge how well our implementation behaves against other codes for deformed nuclei, but its numerical methodology is profoundly different.

An interesting alternative is provided by the EV8 code [14], which is a HF code that solves the problem on a 3D mesh. Unlike our case, the lattice is reduced to a single octant of the box, which allows for faster computational times, imposing plane reflection symmetry on the three planes $(x, y, 0)$, $(x, 0, z)$, $(0, y, z)$. The derivatives are computed using Lagrange derivatives.

EV8 code comparison

Figure 6.4 shows the comparison between the deformation curves of the two codes for ^{24}Mg . Regarding the input parameters of EV8, a step size of 0.8 fm, and a number of points on each axis of 32 is used. The results are compared using the definition of β_2 in formula (6.3), which uses a constant radius.

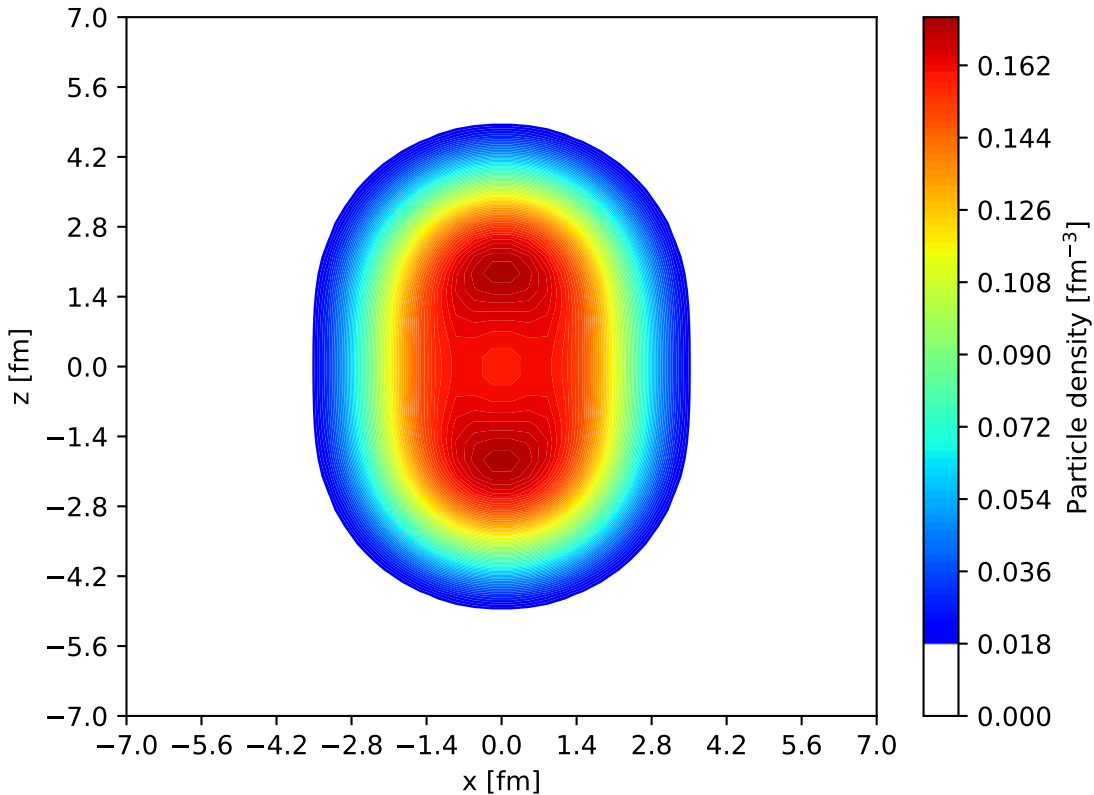


Figura 6.2: ^{24}Mg ground state density $\rho(x, 0, z)$, calculation done on a box $[-10, +10]$ fm, step size 0.33 fm, SkM* parametrisation. The nucleus is shown to be very deformed and prolate.

As shown by the comparison in Figure 6.4, the results are much closer than the ones obtained with the `HFBTH0` code. A slight deviation is still present, likely due to the different numerical methods used by the two codes, both for discretization of the derivatives and the minimisation of the energy functional. Nevertheless, the comparison is highly satisfactory.

6.2.3. Deformation curve for different functionals

In Figure 6.5, two deformation curves for ^{24}Mg are shown, comparing the SkM* and the SLy4 functionals.

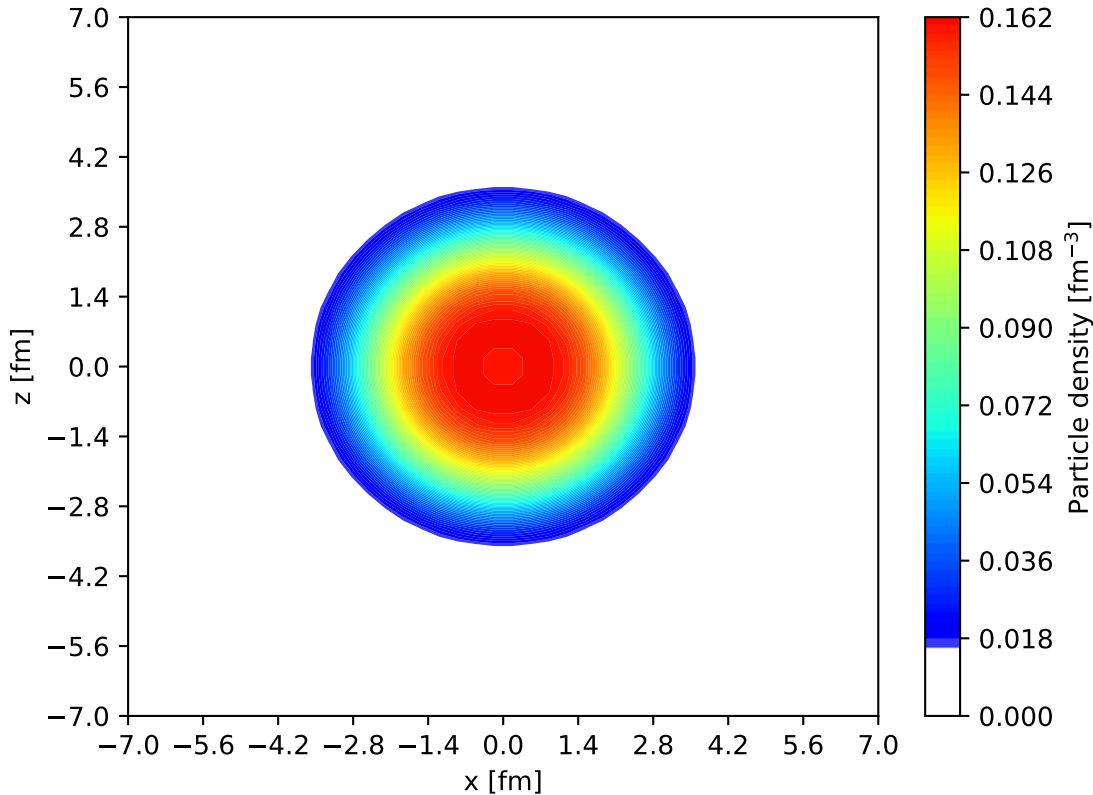


Figura 6.3: ^{24}Mg ground state density $\rho(x, y, 0)$, calculation done on a box $[-10, +10]$ fm, step size 0.33 fm, SkM* parametrisation. The nucleus is shown to be axially symmetric around the z axis.

6.3. Original results

In this final section, some original results for nuclei of interest are discussed. In Section 6.3.1, some results are presented for the ^{20}Ne nucleus, in particular, the Nucleon Localisation Function (NLF) is computed to highlight the formation of clusters. In Section 6.3.2, results for two nuclei near the drip lines are presented, namely ^{42}Si and ^{28}S . The former is a neutron-rich nucleus, with an experimental neutron separation energy of $S_n = 4.458$ MeV, while the latter is a proton-rich nucleus, with an experimental proton separation energy of $S_p = 2.556$ MeV. Both separation energies are much lower than the ones for stable nuclei, placing these isotopes close to the respective drip lines.

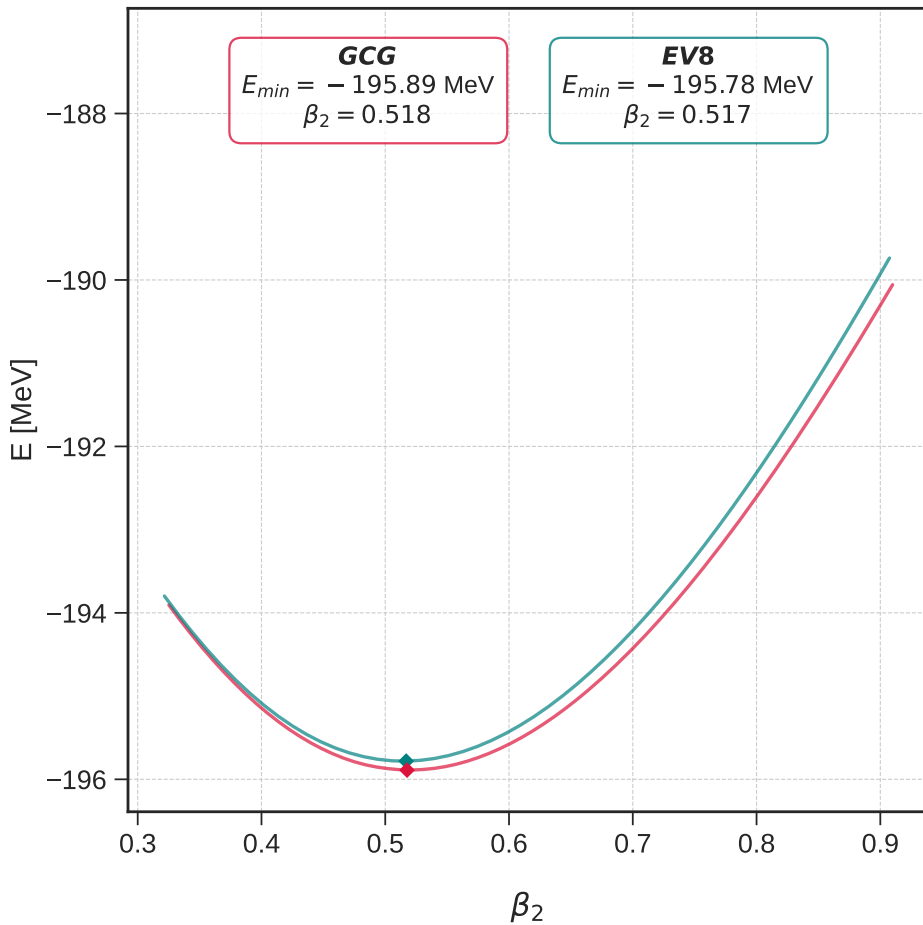


Figura 6.4: Comparison with the EV8 code for ^{24}Mg , no pairing interaction, box $[-10, +10]$ fm, step size 0.6 fm, SLy4 parametrisation. The comparison shows good agreement between the two codes, with similar shapes of the deformation curves and a comparable ground state energy and β_2 value.

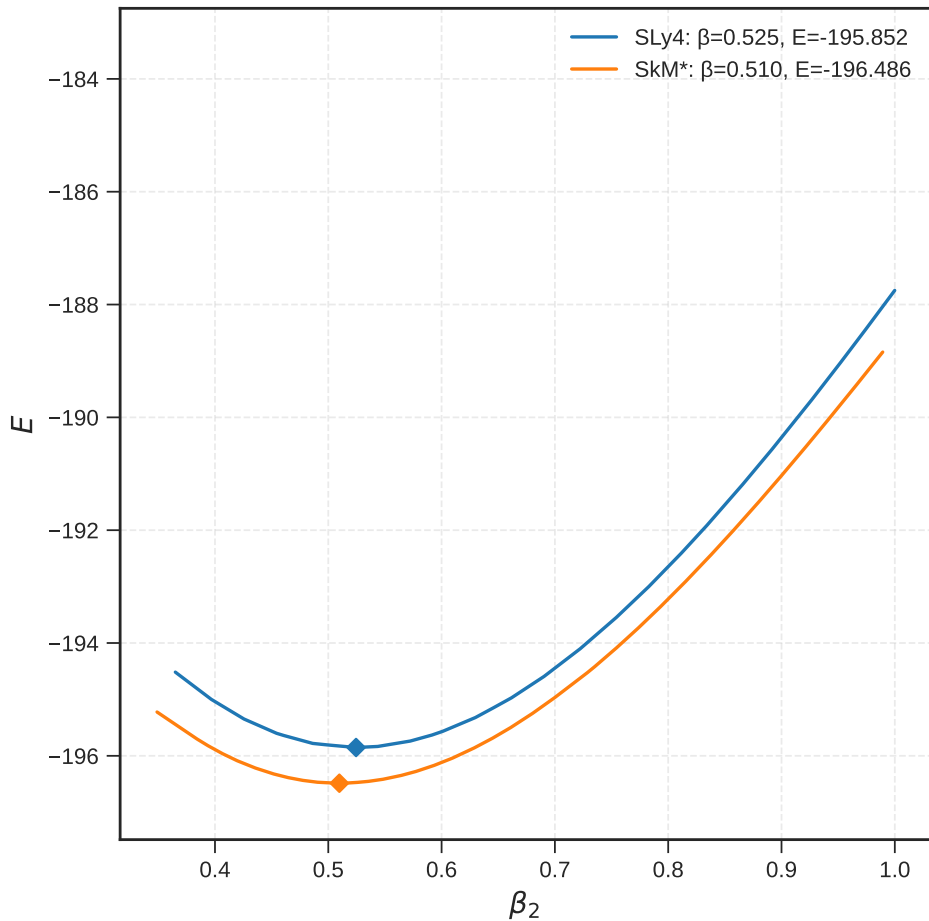


Figura 6.5: Comparison between the SkM* and the SLy4 Skyrme functionals of the ^{24}Mg deformation curves, box $[-10, +10]$ fm, step size 0.6 fm and J^2 terms included. The curves display a similar shape and minimum, with a difference which is due to the data used to fit the functionals.

6.3.1. α -clustering in light nuclei

The formation of clusters in light nuclei has been a focus of various researches in recent years. The interest stems from different reasons. The formation of clusters at low density is a strong indicator of specific correlations (n-p correlations or alpha-particle, ie ‘quartetting’ correlations) and a strong test for theory. At the same time, clustering may have an impact on reactions and astrophysical processes [102]. It has to be noted that cluster formation during fission has been highlighted [103]. One of the hypothesis is that some light nuclei tend to form clusters of lighter particles, mainly α -particles, in order to minimise their energy, by also displaying ‘molecular-like’ bonds and resonances among the clusters. The phenomenon is not yet fully understood. In the framework of the present work, we now illustrate that the formation of clusters is present in ^{20}Ne .

Nucleon localisation function

The study of clusters is made possible by the use of the nucleon localisation function (NLF) [104], which is a measure of the conditional probability of finding a nucleon in the short vicinity of another one in space. When dealing with spin-saturated nuclei, as is the case of ^{20}Ne , the NLF reduces to

$$C_q(\mathbf{r}) = \left[1 + \left(\frac{\tau_q \rho_q - \frac{1}{4} |\nabla \rho_q|^2}{\rho_q \tau_q^{\text{TF}}} \right)^2 \right]^{-1} \quad (6.9)$$

where τ_q^{TF} is the Thomas-Fermi kinetic energy density, defined as

$$\tau_q^{\text{TF}} = \frac{3}{5} (6\pi^2)^{2/3} \rho_q^{5/3}. \quad (6.10)$$

α -clustering in ^{20}Ne

In Figure 6.6, the total particle densities and proton NLF of ^{20}Ne are shown for different Skyrme functionals. It is possible to observe that while some functionals like KDE33 show strong peaks in the particle densities, all the considered functionals display well defined clusters in their respective NLF contours. Note that clustering in the intrinsic frame of the nucleus does not necessarily imply clustering in the laboratory frame, for which projection methods are required [105].

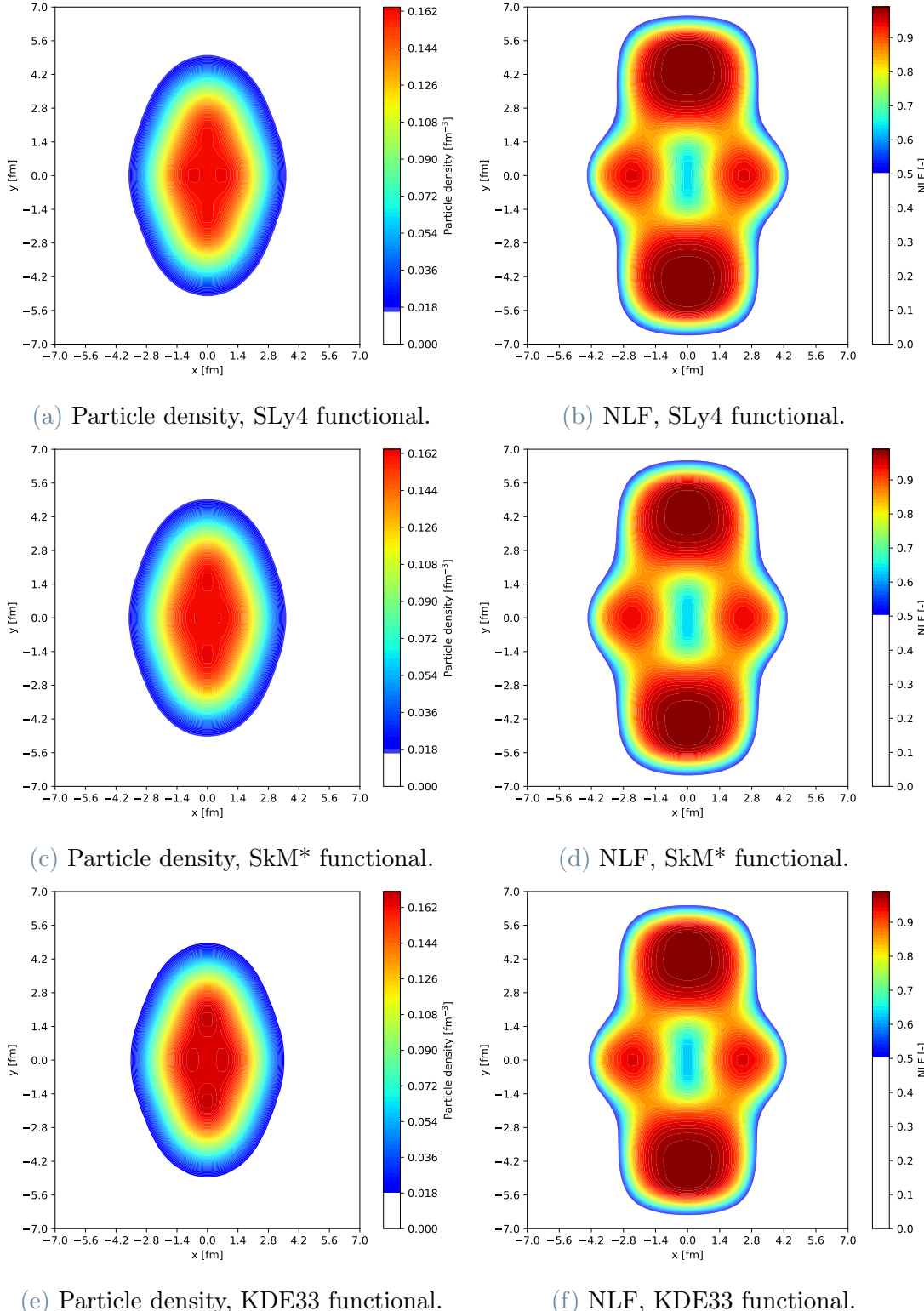


Figura 6.6: Particle densities and NLFs in ^{20}Ne for different Skyrme functionals. The densities show the nuclues to be very deformed and prolate, with possible clusters. The NLFs show a pronounced cluster formation on the top and bottom of a central core.

6.3.2. Nuclei near the drip lines

The need of a mesh representation to account for weakly bound systems has been largely emphasised in previous chapters (see 1, 2). In this section, results regarding the two nuclei near the drip lines ^{42}Si and ^{28}S are presented, the former being a neutron-rich nucleus, the latter being a proton-rich nucleus. Being weakly bound systems, taking direct measurements of quantities like radii, deformations through spectroscopy etc, is not yet possible.

We shall compare the experimental neutron S_n or proton S_p separation energy with the theoretical value calculated using Koopmans' theorem [106]. The theorem states that in a frozen orbitals approximation, where the mean-field is assumed to remain constant after the removal of a particle, the energy required to remove that particle is equal to the eigenvalue of the last occupied single-particle orbital with an opposite sign.

^{42}Si

^{42}Si is a deformed, light, neutron-rich nucleus, having $Z = 14$ and $N = 28$. We may look at its ground state neglecting the pairing interaction thanks to the magic number of neutrons, and the closed sub-shell $1d_{5/2}$. In Table 6.3, data computed with some functionals is reported, along with the experimental extrapolated binding energy and neutron separation energy. In Figure 6.7, the particle density of ^{42}Si is shown for the SLy4 functional.

		SLy4	SkM*	KDE33	Exp.
E	[MeV]	-313.129	-320.760	-326.102	-311.22
S_n	[MeV]	4.349	4.990	4.132	4.458
$\langle r_n^2 \rangle^{1/2}$	[fm]	3.716	3.705	3.666	-
$\langle r_p^2 \rangle^{1/2}$	[fm]	3.294	3.276	3.247	-
$\langle r_{ch}^2 \rangle^{1/2}$	[fm]	3.380	3.362	3.334	-
β_2	[-]	-0.332	0.313	-0.308	-

Tabella 6.3: Results for ^{42}Si , box $[-11, +11]$ fm, step size 0.37 fm. Experimental data taken from [25].

^{28}S

^{28}S is a deformed, light, proton-rich nucleus, having $Z = 16$ and $N = 12$. We may look at its ground state neglecting the pairing interaction thanks to the closed sub-shell $2s_{1/2}$ and a number of neutrons analogous to the one in ^{24}Mg . In Table 6.4, data computed with

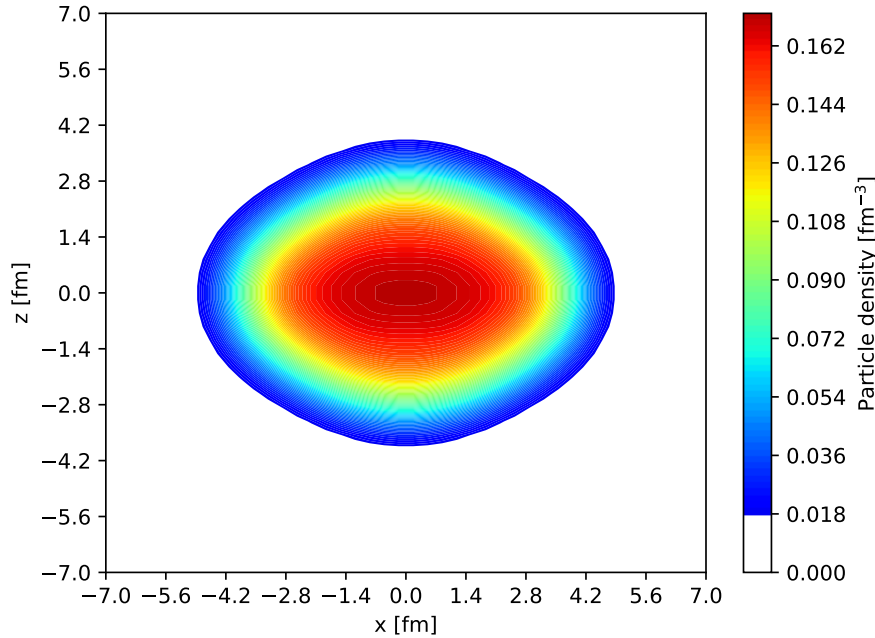


Figura 6.7: ^{42}Si density $\rho(x, 0, z)$, calculation done on a box $[-11, +11]$ fm, step size 0.37 fm, the nucleus is shown to be very deformed and oblate.

some functionals is reported, along with the experimental extrapolated binding energy and proton separation energy. In Figure 6.8, the particle density of ^{28}S is shown for the SLy4 functional.

		SLy4	SkM*	KDE33	Exp.
E	[MeV]	-209.688	-211.642	-221.668	-209.406
S_n	[MeV]	3.370	3.330	3.135	2.556
$\langle r_n^2 \rangle^{1/2}$	[fm]	3.013	2.997	2.964	-
$\langle r_p^2 \rangle^{1/2}$	[fm]	3.235	3.225	3.185	-
$\langle r_{ch}^2 \rangle^{1/2}$	[fm]	3.318	3.308	3.269	-
β_2	[‐]	0.314	0.289	0.293	-

Tabella 6.4: Results for ^{28}S , box $[-10, +10]$ fm, step size 0.34 fm. Experimental data taken from [25].

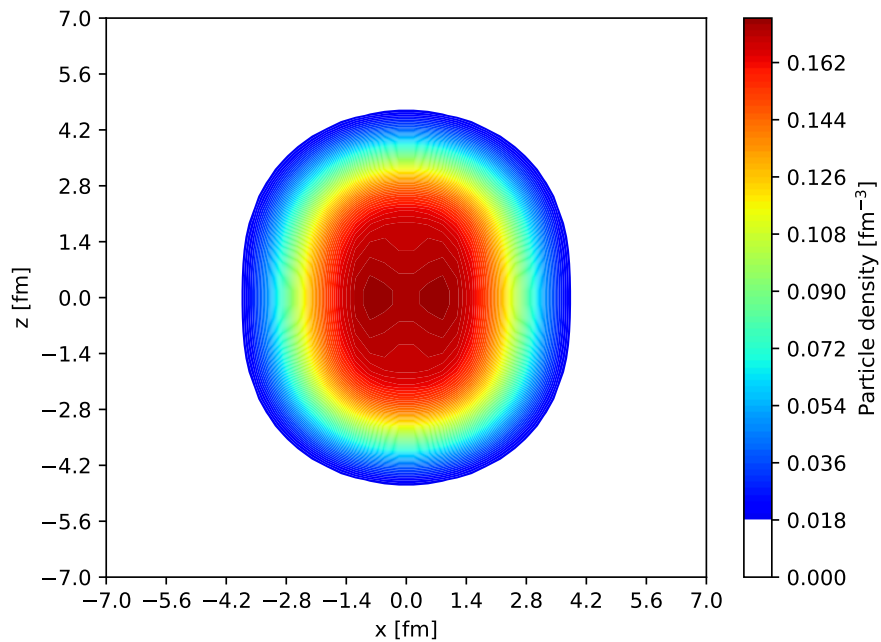


Figura 6.8: ^{28}S density $\rho(x, 0, z)$, calculation done on a box $[-10, +10]$ fm, step size 0.34 fm, the nucleus is shown to be deformed and oblate.

Conclusion and future developments

This work has been aimed to investigate the feasibility and performance of a fully unconstrained Cartesian mesh implementation of nuclear Density Functional Theory based on Skyrme Energy Density Functionals (EDFs). *Fully unconstrained* means here that no a priori spatial symmetry has been assumed for the system. The central objective was to assess whether the Generalised Conjugate Gradient eigensolver could provide a robust and efficient alternative to conventional iterative diagonalisation methods for the minimisation of nuclear energy functionals.

The implementation developed in this thesis demonstrated that this approach is viable and competitive. Benchmarking against the spherical nuclei ^{16}O , ^{48}Ca , ^{56}Ni , and ^{90}Zr showed excellent agreement with the established radial code `hfbcs_qrpa`, validating both the numerical accuracy of the solver and the correctness of the Skyrme EDF implementation. The method was subsequently applied to deformed systems. Comparisons with `HFBTHO` (harmonic oscillator basis expansion) and `EV8` (Cartesian mesh) for the nucleus ^{24}Mg demonstrated that the unconstrained solver reproduces deformation properties and ground-state energies with comparable precision.

Beyond these validation tests, the code was demonstrated to be viable for the exploration of clustering phenomena in the ground state of ^{20}Ne , as well as the structure of the near-drip line nuclei ^{42}Si and ^{28}S . These applications highlight the flexibility of the method in handling strongly deformed, correlated, and weakly bound configurations.

Overall, the GCG method proved to be an efficient and promising tool for DFT calculations, particularly in the frame of Cartesian meshes, which require the diagonalisation of large-scale matrices. The efficiency and precision of GCG make it a suitable candidate for future unconstrained studies, not only for Skyrme functionals, but for ab-initio methods and further physics applications as well.

The implementation presented here establishes a solid foundation but also leads the way for further improvements. These may be grouped into two broad categories: numerical developments and physics extensions.

Numerical improvements

While the GCG eigensolver enables unconstrained calculations, further work is required to optimise its performance and scalability. The most relevant numerical improvements include:

- introducing suitable preconditioning schemes for the approximate inverse power iteration, which would significantly accelerate convergence;
- improving spatial discretisation by employing more accurate derivative operators;
- implementing efficient iterative orthonormalisation strategies to handle large orbital sets; and
- enhancing the minimisation of the EDF through advanced mixing techniques such as Broyden mixing, DIIS, or Anderson acceleration.

Furthermore, additional performance gains could be achieved by exploiting modern computational hardware. In particular, GPU acceleration for linear algebra operations and a more careful optimisation of memory access patterns would improve runtime and allow larger grid sizes to be explored.

Physics additions

From the physics perspective, several important extensions lie naturally beyond the present work. These include:

- incorporating pairing correlations through a BCS or full HFB framework with an effective pairing interaction, enabling the description of superfluid systems. This may be relatively straightforward and, in a sense, could be considered the first priority;
- extending the formalism to odd-mass nuclei by introducing time-odd densities into the Skyrme functional and developing blocking techniques; and
- implementing cranking calculations to access rotational bands and the spectra of deformed nuclei.

Such improvements would substantially broaden the range of phenomena that can be studied with this framework. In addition, the orbitals, densities, and quasiparticle energies obtained from the solver provide a valuable starting point for beyond-mean-field methods, most notably QRPA, collective inertia calculations, and Generator Coordinate Method treatments of large-amplitude collective motion.

Final Remarks

Although many extensions remain to be implemented, the results presented in this thesis already demonstrate the strong potential of an unconstrained DFT solver written on a mesh, and based on the Generalised Conjugate Gradient method. The ability to perform three-dimensional, symmetry-unrestricted calculations with modest computational resources opens promising prospects for applications in nuclear structure. In particular, this work paves the way for studies of heavy nuclei, which are also of interest in the context of nuclear fission. Such investigations could be facilitated by extending the present code to include pairing correlations, enabling its execution on high-performance computing platforms and optimising it for parallel linear-algebra operations on GPUs.

In summary, the work developed here provides a first step towards a more general and flexible computational framework. Its extension to pairing correlations, odd nuclei, rotational states, and collective dynamics will further enhance its scope, ultimately contributing to a more complete microscopic description of nuclear structure and deformations.

Bibliografia

- [1] W. D. Myers and W. J. Swiatecki. Nuclear properties according to the lublin-strasbourg drop model. *Nuclear Physics A*, 601:141–167, 1996.
- [2] P. Möller, A. Sierk, T. Ichikawa, and H. Sagawa. Nuclear ground-state masses and deformations: Frdm(2012). *Atomic Data and Nuclear Data Tables*, 109–110:1–204, 2016.
- [3] N. Schunck and L. M. Robledo. Microscopic theory of nuclear fission: a review. *Reports on Progress in Physics*, 79(11):116301, 2016. doi: 10.1088/0034-4885/79/11/116301.
- [4] G. Hagen, T. Papenbrock, M. Hjorth-Jensen, and D. J. Dean. Coupled-cluster computations of atomic nuclei. *Reports on Progress in Physics*, 77:096302, 2014.
- [5] G. Colò. Nuclear density functional theory. *Advances in Physics: X*, 5(1):1740061, 2020. doi: 10.1080/23746149.2020.1740061. URL <https://doi.org/10.1080/23746149.2020.1740061>.
- [6] M. Bender, P.-H. Heenen, and P.-G. Reinhard. Self-consistent mean-field models for nuclear structure. *Reviews of Modern Physics*, 75(1):121–180, 2003. doi: 10.1103/RevModPhys.75.121.
- [7] D. Vautherin and D. M. Brink. Hartree–fock calculations with skyrme’s interaction. i. spherical nuclei. *Phys. Rev. C*, 5:626–647, Mar 1972. doi: 10.1103/PhysRevC.5.626. URL <https://link.aps.org/doi/10.1103/PhysRevC.5.626>.
- [8] N. Schunck, J. Dobaczewski, J. McDonnell, J. Sarich, A. Staszczak, and M. V. Stoitosov. Solution of the HFB equation in the oscillatory basis: the HFODD code. *Computer Physics Communications*, 183(1):166–191, 2012. doi: 10.1016/j.cpc.2011.09.018.
- [9] P. Marević, N. Schunck, and K. Sato. Axially-deformed solution of the skyrme-hartree–fock–bogoliubov problem in the harmonic-oscillator basis. *Computer Physics Communications*, 283:108640, 2022. doi: 10.1016/j.cpc.2022.108640.

- [10] P. Bonche, H. Flocard, and P. H. Heenen. Solution of the skyrme HF + BCS equation on a 3d mesh. *Computer Physics Communications*, 171(1):49–62, 2005. doi: 10.1016/j.cpc.2005.03.001.
- [11] W. Ryssens, P.-H. Heenen, and M. Bender. Symmetry-unrestricted skyrme mean-field study of heavy nuclei: the mocca code. *arXiv preprint*, 2016. arXiv:1611.01300 [nucl-th].
- [12] Mengzhi Chen, Tong Li, Bastian Schuetrumpf, Paul-Gerhard Reinhard, and Witold Nazarewicz. Three-dimensional skyrme hartree–fock–bogoliubov solver in coordinate-space representation. *Computer Physics Communications*, 275:108344, 2022. doi: 10.1016/j.cpc.2022.108344. This paper describes the new 3D, symmetry-unrestricted coordinate-space solver HFBFFT, which is based on the Sky3D code.
- [13] J.A. Maruhn, P.-G. Reinhard, P.D. Stevenson, and A.S. Umar. The tdhf code sky3d. *Computer Physics Communications*, 185(7):2195–2216, 2014. ISSN 0010-4655. doi: <https://doi.org/10.1016/j.cpc.2014.04.008>. URL <https://www.sciencedirect.com/science/article/pii/S0010465514001313>.
- [14] W. Ryssens, V. Hellemans, M. Bender, and P.-H. Heenen. Solution of the skyrme hf+bcs equation on a 3d mesh. ii. a new version of the ev8 code. *Computer Physics Communications*, 187:175–194, 2015. doi: 10.1016/j.cpc.2014.10.001.
- [15] Carlos A Bertulani. Nuclear physics in a nutshell. 2007.
- [16] Alexandre Obertelli and Hiroyuki Sagawa. *Modern nuclear physics*. Springer, 2021.
- [17] Peter Ring and Peter Schuck. *The nuclear many-body problem*. Springer Science & Business Media, 2004.
- [18] Robert Hofstadter. Electron scattering and nuclear structure. *Reviews of Modern Physics*, 28:214–254, 1956. doi: 10.1103/RevModPhys.28.214.
- [19] C. F. von Weizsäcker. Zur Theorie der Kernmassen. *Zeitschrift für Physik*, 96(7-8): 431–458, 1935. doi: 10.1007/BF01337700.
- [20] Daniel FR. Liquid drop model.svg: Illustration of the terms of the semi-empirical mass formula in the liquid drop model of the atomic nucleus. Wikimedia Commons, the free media repository, 2012. URL https://commons.wikimedia.org/wiki/File:Liquid_drop_model.svg. Original work by Honina, derivative by Daniel FR. Licensed under CC BY-SA 3.0.

- [21] Djelloul Benzaid, Salaheddine Bentridi, Abdelkader Kerraci, and Naima Amrani. Bethe–Weizsäcker semiempirical mass formula coefficients 2019 update based on AME2016. *Nuclear Science and Techniques*, 31(1):5, 2020. doi: 10.1007/s41365-019-0718-8.
- [22] J. W. Rohlf. *Modern Physics from Alpha to Z0*. John Wiley & Sons, 1994.
- [23] N. Schwierz, I. Wiedenhöver, and A. Volya. Parameterization of the woods–saxon potential for shell-model calculations. *arXiv preprint arXiv:0709.3525*, 2007. nucl-th/0709.3525.
- [24] Colo’ Gianluca. Nuclear physics - lecture notes (academic year 2021/22). Online PDF, Dipartimento di Fisica, Universita’ degli Studi di Milano / INFN Milano, 2021. Accessed from https://www0.mi.infn.it/~colo/Didattica/Nucleare/2021_22/nuclphys3.pdf.
- [25] Atomic Mass Data Center. Atomic Mass Data Center. URL <https://www-nds.iaea.org/amdc/>. Accessed: 19 October 2025.
- [26] Ben Mottelson. The nilsson model and sven gösta nilsson. *Physica Scripta*, 125, 2006.
- [27] Wikipedia contributors. Nilsson model graphical representation – wikipedia. <https://en.wikipedia.org/w/index.php?curid=60892381>, 2025.
- [28] J Dudek and T Werner. New parameters of the deformed woods–saxon potential for $a=110\text{--}210$ nuclei. *Journal of Physics G: Nuclear Physics*, 4(10):1543, oct 1978. doi: 10.1088/0305-4616/4/10/006. URL <https://doi.org/10.1088/0305-4616/4/10/006>.
- [29] P. Jachimowicz, M. Kowal, and J. Skalski. Adiabatic fission barriers in superheavy nuclei. *Phys. Rev. C*, 95:014303, Jan 2017. doi: 10.1103/PhysRevC.95.014303. URL <https://link.aps.org/doi/10.1103/PhysRevC.95.014303>.
- [30] Wiktor Kurcewicz. Octupole deformation in the actinide region. *Hyperfine Interactions*, 129(1):175–184, 12 2000. ISSN 1572-9540. doi: 10.1023/A:1012609832646. URL <https://doi.org/10.1023/A:1012609832646>.
- [31] B. Bucher, S. Zhu, C.-Y. Wu, R. V. F. Janssens, D. Cline, A. B. Hayes, M. Albers, A. D. Ayangeakaa, P. A. Butler, C. M. Campbell, M. P. Carpenter, C. J. Chiara, J. A. Clark, H. L. Crawford, M. Cromaz, H. M. David, C. Dickerson, E. T. Gregor, J. Harker, C. R. Hoffman, B. P. Kay, F. G. Kondev, A. Korichi, T. Lauritsen, A. O. Macchiavelli, R. C. Pardo, A. Richard, M. A. Riley, G. Savard, M. Scheck,

- D. Seweryniak, M. K. Smith, R. Vondrasek, and A. Wiens. Direct evidence of octupole deformation in neutron-rich ^{144}Ba . *Phys. Rev. Lett.*, 116(11):112503, 2016. doi: 10.1103/PhysRevLett.116.112503.
- [32] B. Bucher, S. Zhu, C.-Y. Wu, R. V. F. Janssens, R. Bernard, L. M. Robledo, T. R. Rodríguez, D. Cline, A. B. Hayes, A. D. Ayangeakaa, M. Buckner, C. M. Campbell, M. P. Carpenter, J. A. Clark, H. L. Crawford, H. M. David, C. Dickerson, J. Harker, C. R. Hoffman, B. P. Kay, F. G. Kondev, T. Lauritsen, A. O. Macchiavelli, R. C. Pardo, G. Savard, D. Seweryniak, and R. Vondrasek. Direct evidence for octupole deformation in ^{146}Ba and the origin of large $e1$ moment variations in reflection-asymmetric nuclei. *Phys. Rev. Lett.*, 118(15):152504, 2017. doi: 10.1103/PhysRevLett.118.152504.
- [33] P. A. Butler, L. P. Gaffney, P. Spagnoletti, K. Abrahams, M. Bowry, J. Cederkäll, G. de Angelis, H. De Witte, P. E. Garrett, A. Goldkuhle, C. Henrich, A. Illana, K. Johnston, D. T. Joss, J. M. Keatings, N. A. Kelly, M. Komorowska, J. Konki, T. Kröll, M. Lozano, B. S. Nara Singh, D. O'Donnell, J. Ojala, R. D. Page, L. G. Pedersen, C. Raison, P. Reiter, J. A. Rodriguez, D. Rosiak, S. Rothe, M. Scheck, M. Seidlitz, T. M. Shneidman, B. Siebeck, J. Sinclair, J. F. Smith, M. Stryjczyk, P. Van Duppen, S. Vinals, V. Virtanen, N. Warr, K. Wrzosek-Lipska, and M. Zielińska. Evolution of octupole deformation in radium nuclei from coulomb excitation of radioactive $^{222,228}\text{Ra}$ beams. *Phys. Rev. Lett.*, 124(4):042503, 2020. doi: 10.1103/PhysRevLett.124.042503.
- [34] P. A. Butler. Octupole collectivity in nuclei. *Progress in Particle and Nuclear Physics (review / conference chapter)*, 2016. review / summary of Coulomb-excitation results and octupole collectivity.
- [35] Niels Bohr and John A. Wheeler. The mechanism of nuclear fission. *Physical Review*, 56:426–450, 1939.
- [36] V. M. Strutinsky. Shell effects in nuclear masses and deformation energies. *Nuclear Physics A*, 95:420–442, 1967.
- [37] M. Brack, J. Damgaard, A. J. Jensen, H. C. Pauli, V. M. Strutinsky, and C. Y. Wong. Funny hills: the shell-correction approach to nuclear shell effects and its applications to the fission process. *Reviews of Modern Physics*, 44:320–405, 1972.
- [38] M. Bender, R. Bernard, G. F. Bertsch, S. Chiba, J. Dobaczewski, N. Dubray, S. A. Giuliani, K. Hagino, W. Nazarewicz, N. Schunck, et al. Future of nuclear fission

- theory. *Journal of Physics G: Nuclear and Particle Physics*, 48(4):043001, 2021. doi: 10.1088/1361-6471/abcf62.
- [39] Philip Goddard, Paul Stevenson, and Arnau Rios. Fission dynamics within time-dependent hartree–fock: Deformation-induced fission. *Phys. Rev. C*, 92:054610, Nov 2015. doi: 10.1103/PhysRevC.92.054610. URL <https://link.aps.org/doi/10.1103/PhysRevC.92.054610>.
- [40] M. V. Stoitsov, J. Dobaczewski, W. Nazarewicz, S. Pittel, and D. J. Dean. Systematic study of deformed nuclei at the drip lines and beyond. *Phys. Rev. C*, 68(5):054312, 2003. doi: 10.1103/PhysRevC.68.054312.
- [41] J. Dobaczewski, W. Nazarewicz, T. R. Werner, J. F. Berger, C. R. Chinn, and J. Decharge. Mean-field description of ground-state properties of drip-line nuclei: Pairing and continuum effects. *Phys. Rev. C*, 53(1):2809, 1996. doi: 10.1103/PhysRevC.53.2809.
- [42] Gianluca Colo' and Xavier Roca-Maza. User guide for the hfbcsvrpa(v1) code.
- [43] J. C. Pei, M. V. Stoitsov, G. I. Fann, W. Nazarewicz, N. Schunck, and F. R. Xu. Deformed coordinate-space hartree–fock–bogoliubov approach to weakly bound nuclei and large deformations. *Physical Review C*, 78(6):064306, 2008. doi: 10.1103/PhysRevC.78.064306.
- [44] Mengzhi Chen, Tong Li, Bastian Schuetrumpf, Paul-Gerhard Reinhard, and Witold Nazarewicz. Three-dimensional skyrme hartree–fock–bogoliubov solver in coordinate-space representation. *Computer Physics Communications*, 276:108344, 2022. ISSN 0010-4655. doi: <https://doi.org/10.1016/j.cpc.2022.108344>. URL <https://www.sciencedirect.com/science/article/pii/S0010465522000625>.
- [45] T.H.R. Skyrme. The effective nuclear potential. *Nuclear Physics*, 9(4):615–634, 1958. ISSN 0029-5582. doi: [https://doi.org/10.1016/0029-5582\(58\)90345-6](https://doi.org/10.1016/0029-5582(58)90345-6). URL <https://www.sciencedirect.com/science/article/pii/0029558258903456>.
- [46] P. Hohenberg and W. Kohn. Inhomogeneous electron gas. *Phys. Rev.*, 136:B864–B871, Nov 1964. doi: 10.1103/PhysRev.136.B864. URL <https://link.aps.org/doi/10.1103/PhysRev.136.B864>.
- [47] W. Kohn and L. J. Sham. Self-consistent equations including exchange and correlation effects. *Phys. Rev.*, 140:A1133–A1138, Nov 1965. doi: 10.1103/PhysRev.140.A1133. URL <https://link.aps.org/doi/10.1103/PhysRev.140.A1133>.

- [48] Richard M. Martin. *Electronic Structure: Basic Theory and Practical Methods*. Cambridge University Press, Cambridge, UK, 2004. ISBN 9780521534406.
- [49] J. A. Koponen, K. Pellikka, S. Tanimoto, K. Dendo, T. Lesinski, and K. Terasaki. The axial hartree–fock + BCS code SkyAx. *Computer Physics Communications*, 267:108034, 2021. doi: 10.1016/j.cpc.2021.108034.
- [50] P. Marević, N. Schunck, E.M. Ney, R. Navarro Pérez, M. Verriere, and J. O’Neal. Axially-deformed solution of the skyrme-hartree–fock–bogoliubov equations using the transformed harmonic oscillator basis (iv) hfbtho (v4.0): A new version of the program. *Computer Physics Communications*, 276:108367, 2022. ISSN 0010-4655. doi: <https://doi.org/10.1016/j.cpc.2022.108367>. URL <https://www.sciencedirect.com/science/article/pii/S0010465522000868>.
- [51] J. Dobaczewski. Generalisation of the bloch-messiah-zumino theorem. *Phys. Rev. C*, 62:017301, May 2000. doi: 10.1103/PhysRevC.62.017301. URL <https://link.aps.org/doi/10.1103/PhysRevC.62.017301>.
- [52] J. C. Pei, A. T. Kruppa, and W. Nazarewicz. Quasi-particle continuum and resonances in the hartree–fock–bogoliubov theory. *Physical Review C*, 84(2):024311, 2011. doi: 10.1103/PhysRevC.84.024311.
- [53] M. Brack, J. Damgaard, A. S. Jensen, H. C. Pauli, V. M. Strutinsky, and C. Y. Wong. Funny hills: The shell-correction approach to nuclear shell effects and its applications to the fission process. *Reviews of Modern Physics*, 44(2):320–405, 1972. doi: 10.1103/RevModPhys.44.320.
- [54] S. Bjørnholm and J. E. Lynn. The double-humped fission barrier. *Reviews of Modern Physics*, 52(4):725–931, 1980. doi: 10.1103/RevModPhys.52.725.
- [55] H. J. Krappe and K. Pomorski. *Theory of Nuclear Fission: A Textbook*. Springer, 2012. doi: 10.1007/978-3-642-23515-3.
- [56] N. Dubray and D. Regnier. Numerical search of discontinuities in self-consistent potential energy surfaces. *Computer Physics Communications*, 183(10):2035–2041, 2012. doi: 10.1016/j.cpc.2012.04.001.
- [57] H. Goutte, J.-F. Berger, P. Casoli, and D. Gogny. Microscopic approach of fission dynamics applied to fragment kinetic energy and mass distributions in ^{238}u . *Physical Review C*, 71(2):024316, 2005. doi: 10.1103/PhysRevC.71.024316.

- [58] D. Regnier, N. Dubray, M. Verrière, and N. Schunck. Microscopic description of complex fission phenomena using the time-dependent generator coordinate method. *Physical Review C*, 99(2):024611, 2019. doi: 10.1103/PhysRevC.99.024611.
- [59] M. Bender, P.-H. Heenen, and P.-G. Reinhard. Configuration mixing of angular-momentum projected self-consistent mean-field states for low-spin states in ^{240}pu . *Physical Review C*, 69(6):064303, 2004. doi: 10.1103/PhysRevC.69.064303.
- [60] M. Samyn, S. Goriely, and J. M. Pearson. Fission barriers in the d1s gogny force with particle-number and parity restoration. *Physical Review C*, 72(4):044316, 2005. doi: 10.1103/PhysRevC.72.044316.
- [61] John W. Negele. The mean-field theory of nuclear structure and dynamics. *Reviews of Modern Physics*, 54(4):913–1015, 1982. doi: 10.1103/RevModPhys.54.913.
- [62] A Bulgac and K J Roche. Time-dependent density functional theory applied to superfluid nuclei. *Journal of Physics: Conference Series*, 125(1):012064, jul 2008. doi: 10.1088/1742-6596/125/1/012064. URL <https://doi.org/10.1088/1742-6596/125/1/012064>.
- [63] A. Bulgac, P. Magierski, K. J. Roche, and I. Stetcu. Induced fission of ^{240}pu within a real-time microscopic framework. *Physical Review Letters*, 116(12):122504, 2016. doi: 10.1103/PhysRevLett.116.122504.
- [64] S. Ayik. A stochastic mean-field approach for nuclear dynamics. *Physics Letters B*, 658(3):174–178, 2008. doi: 10.1016/j.physletb.2007.09.072.
- [65] M. Warda, J. L. Egido, L. M. Robledo, and K. Pomorski. Microscopic description of the fission path of actinides with the gogny force. *Physical Review C*, 66(1):014310, 2002. doi: 10.1103/PhysRevC.66.014310.
- [66] G. F. Bertsch, L. M. Robledo, and W. Younes. Fission potential energy surfaces from constrained self-consistent mean-field theory. *Physical Review C*, 97(2):024306, 2018. doi: 10.1103/PhysRevC.97.024306.
- [67] C. Simenel and A. S. Umar. Nuclear quantum many-body dynamics: From collective vibrations to heavy-ion collisions. *Progress in Particle and Nuclear Physics*, 103: 19–66, 2018. doi: 10.1016/j.ppnp.2018.01.004.
- [68] E. Chabanat, P. Bonche, P. Haensel, J. Meyer, and R. Schaeffer. A skyrme parametrisation from subnuclear to neutron star densities. *Nuclear Physics A*, 627(4):710–746, 1997. ISSN 0375-9474. doi: [https://doi.org/10.1016/S0375-9474\(97\)80003-7](https://doi.org/10.1016/S0375-9474(97)80003-7).

- 1016/S0375-9474(97)00596-4. URL <https://www.sciencedirect.com/science/article/pii/S0375947497005964>.
- [69] J Erler, P Klüpfel, and P-G Reinhard. Misfits in skyrme-hartree–fock. *Journal of Physics G: Nuclear and Particle Physics*, 37(6):064001, mar 2010. doi: 10.1088/0954-3899/37/6/064001. URL <https://doi.org/10.1088/0954-3899/37/6/064001>.
- [70] P.-G. Reinhard and H. Flocard. Nuclear effective forces and isotope shifts. *Nuclear Physics A*, 584(3):467–488, 1995. ISSN 0375-9474. doi: [https://doi.org/10.1016/0375-9474\(94\)00770-N](https://doi.org/10.1016/0375-9474(94)00770-N). URL <https://www.sciencedirect.com/science/article/pii/037594749400770N>.
- [71] P.D. Stevenson and M.C. Barton. Low-energy heavy-ion reactions and the skyrme effective interaction. *Progress in Particle and Nuclear Physics*, 104:142–164, 2019. ISSN 0146-6410. doi: <https://doi.org/10.1016/j.ppnp.2018.09.002>. URL <https://www.sciencedirect.com/science/article/pii/S0146641018300851>.
- [72] E. Chabanat, P. Bonche, P. Haensel, J. Meyer, and R. Schaeffer. A skyrme parametrisation from subnuclear to neutron star densities part ii. nuclei far from stabilities. *Nuclear Physics A*, 635(1):231–256, 1998. ISSN 0375-9474. doi: [https://doi.org/10.1016/S0375-9474\(98\)00180-8](https://doi.org/10.1016/S0375-9474(98)00180-8). URL <https://www.sciencedirect.com/science/article/pii/S0375947498001808>.
- [73] M. Beiner, H. Flocard, Nyguyen van Giai, and P. Quentin. Nuclear ground state properties and selfconsistent calculations with the Skyrme interactions: 1. Spherical description. *Nucl. Phys. A*, 238:29–69, 1975. doi: 10.1016/0375-9474(75)90338-3.
- [74] J. Bartel, P. Quentin, M. Brack, C. Guet, and H.-B. Häkansson. Towards a better parametrisation of skyrme-like effective forces: A critical study of the skm force. *Nuclear Physics A*, 386(1):79–100, 1982. ISSN 0375-9474. doi: [https://doi.org/10.1016/0375-9474\(82\)90403-1](https://doi.org/10.1016/0375-9474(82)90403-1). URL <https://www.sciencedirect.com/science/article/pii/0375947482904031>.
- [75] M. Kortelainen, T. Lesinski, J. Moré, W. Nazarewicz, J. Sarich, N. Schunck, M. V. Stoitsov, and S. Wild. Nuclear energy density optimization. *Phys. Rev. C*, 82: 024313, Aug 2010. doi: 10.1103/PhysRevC.82.024313. URL <https://link.aps.org/doi/10.1103/PhysRevC.82.024313>.
- [76] Huai-Qiang Gu, Haozhao Liang, Wen Hui Long, Nguyen Van Giai, and Jie Meng. Slater approximation for coulomb exchange effects in nuclear covariant density func-

- tional theory. *Phys. Rev. C*, 87:041301, Apr 2013. doi: 10.1103/PhysRevC.87.041301. URL <https://link.aps.org/doi/10.1103/PhysRevC.87.041301>.
- [77] John David Jackson. *Classical Electrodynamics*. John Wiley & Sons, New York, 3rd edition, 1998. ISBN 978-0471309321.
- [78] Pei-bai Zhou. *Finite Difference Method*, pages 63–94. Springer Berlin Heidelberg, Berlin, Heidelberg, 1993. ISBN 978-3-642-50319-1. doi: 10.1007/978-3-642-50319-1_3. URL https://doi.org/10.1007/978-3-642-50319-1_3.
- [79] Gene H. Golub and Charles F. van Loan. *Matrix Computations*. JHU Press, fourth edition, 2013. ISBN 1421407949 9781421407944. URL <http://www.cs.cornell.edu/cv/GVL4/golubandvanloan.htm>.
- [80] Yousef Saad. *Numerical Methods for Large Eigenvalue Problems*. Manchester University Press, Manchester, UK, 1992.
- [81] Jonathan Richard Shewchuk. An introduction to the conjugate gradient method without the agonizing pain. 1994. URL <http://www.cs.cmu.edu/~quake-papers/painless-conjugate-gradient.pdf>.
- [82] Aravindh Krishnamoorthy and Deepak Menon. Matrix inversion using cholesky decomposition. In *2013 Signal Processing: Algorithms, Architectures, Arrangements, and Applications (SPA)*, pages 70–72, 2013.
- [83] John W Pearson and Jennifer Pestana. Preconditioners for krylov subspace methods: An overview. *GAMM-Mitteilungen*, 43(4):e202000015, 2020.
- [84] Cornelius Lanczos. Solution of systems of linear equations by minimised iterations. *J. Res. Nat. Bur. Standards*, 49(1):33–53, 1952.
- [85] A. V. Knyazev. *A Preconditioned Conjugate Gradient Method for Eigenvalue Problems and its Implementation in a Subspace*, pages 143–154. Birkhäuser Basel, Basel, 1991. ISBN 978-3-0348-6332-2. doi: 10.1007/978-3-0348-6332-2_11. URL https://doi.org/10.1007/978-3-0348-6332-2_11.
- [86] Jeheon Woo, Seonghwan Kim, and Woo Youn Kim. Gaussian-approximated poisson preconditioner for iterative diagonalization in real-space density functional theory. *The Journal of Physical Chemistry A*, 127(17):3883–3893, 2023. doi: 10.1021/acs.jpca.2c09111. URL <https://doi.org/10.1021/acs.jpca.2c09111>. PMID: 37094552.

- [87] Tommaso Nottoli, Ivan Gianni, Antoine Levitt, and Filippo Lipparini. A robust, open-source implementation of the locally optimal block preconditioned conjugate gradient for large eigenvalue problems in quantum chemistry. *Theoretical Chemistry Accounts*, 142(8):69, 2023. ISSN 1432-2234. doi: 10.1007/s00214-023-03010-y. URL <https://doi.org/10.1007/s00214-023-03010-y>.
- [88] Lin Lin, Sihong Shao, and Weinan E. Efficient iterative method for solving the dirac-kohn-sham density functional theory. *Journal of Computational Physics*, 245:205–217, 2013. ISSN 0021-9991. doi: <https://doi.org/10.1016/j.jcp.2013.03.030>. URL <https://www.sciencedirect.com/science/article/pii/S0021999113002088>.
- [89] B Li, ZX Ren, and PW Zhao. Efficient solution for the dirac equation in 3d lattice space with the conjugate gradient method. *Physical Review C*, 102(4):044307, 2020.
- [90] Yu Li, Hehu Xie, Ran Xu, Chun'guang You, and Ning Zhang. A parallel generalised conjugate gradient method for large scale eigenvalue problems. *CCF Transactions on High Performance Computing*, 2(2):111–122, jun 2020. ISSN 2524-4930. doi: 10.1007/s42514-020-00029-6. URL <https://doi.org/10.1007/s42514-020-00029-6>. The corresponding computing package can be downloaded from the web site: <https://github.com/pase2017/GCGE-1.0>.
- [91] Åke Björck. Numerics of gram-schmidt orthogonalization. *Linear Algebra and Its Applications*, 197:297–316, 1994.
- [92] P. Bonche, H. Flocard, and P.-H. Heenen. Self-consistent calculation of nuclear rotations: The complete yrast line of 24mg. *Nuclear Physics A*, 443(1):39–63, 1985. doi: 10.1016/0375-9474(85)90224-7.
- [93] H. Flocard, P. Quentin, A.K. Kerman, and D. Vautherin. Nuclear deformation energy curves with the constrained hartree–fock method. *Nuclear Physics A*, 203(3):433–472, 1973. ISSN 0375-9474. doi: [https://doi.org/10.1016/0375-9474\(73\)90357-6](https://doi.org/10.1016/0375-9474(73)90357-6). URL <https://www.sciencedirect.com/science/article/pii/0375947473903576>.
- [94] R. Y. Cusson, P. G. Reinhard, M. R. Strayer, J. A. Maruhn, and W. Greiner. Density as a constraint and the separation of internal excitation energy in tdhf. *Zeitschrift für Physik A Atoms and Nuclei*, 320:475–482, 1985. doi: 10.1007/BF01415725. URL <https://doi.org/10.1007/BF01415725>.
- [95] W. Ryssens, V. Hellemans, M. Bender, and P.-H. Heenen. Solution of the skyrme-hf+bcg equation on a 3d mesh, ii: A new version of the ev8 code. *Computer Physics Communications*, 187:175–194, 2015. ISSN 0010-4655. doi: <https://doi.org/10.1016/j.cpc.2015.06.019>.

- org/10.1016/j.cpc.2014.10.001. URL <https://www.sciencedirect.com/science/article/pii/S0010465514003361>.
- [96] A. Staszczak, M. Stoitsov, A. Baran, and W. Nazarewicz. Augmented lagrangian method for constrained nuclear density functional theory. *The European Physical Journal A*, 46:85–90, 2010. doi: 10.1140/epja/i2010-11018-9. URL <https://doi.org/10.1140/epja/i2010-11018-9>.
- [97] Bjarne Stroustrup. An overview of c++. In *Proceedings of the 1986 SIGPLAN workshop on Object-oriented programming*, pages 7–18, 1986.
- [98] Gaël Guennebaud, Benoît Jacob, et al. Eigen. <http://eigen.tuxfamily.org>, 2010.
- [99] W. Bertozzi, J. Friar, J. Heisenberg, and J.W. Negele. Contributions of neutrons to elastic electron scattering from nuclei. *Physics Letters B*, 41(4):408–414, 1972. ISSN 0370-2693. doi: [https://doi.org/10.1016/0370-2693\(72\)90662-4](https://doi.org/10.1016/0370-2693(72)90662-4). URL <https://www.sciencedirect.com/science/article/pii/0370269372906624>.
- [100] I. Angeli and K.P. Marinova. Table of experimental nuclear ground state charge radii: An update. *Atomic Data and Nuclear Data Tables*, 99(1):69–95, 2013. ISSN 0092-640X. doi: <https://doi.org/10.1016/j.adt.2011.12.006>. URL <https://www.sciencedirect.com/science/article/pii/S0092640X12000265>.
- [101] S. Hilaire and M. Girod. Hartree–fock–bogoliubov results based on the gogny force, 2006. URL https://www-phynu.cea.fr/science_en_ligne/carte_potentiels_microscopiques/carte_potentiel_nucleaire_eng.htm. Part of the "AMEDEE" database.
- [102] Ivano Lombardo and Daniele Dell'Aquila. Clusters in light nuclei: history and recent developments. *La Rivista del Nuovo Cimento*, 46(9):521–618, sep 2023. ISSN 1826-9850. doi: 10.1007/s40766-023-00047-4. URL <https://doi.org/10.1007/s40766-023-00047-4>.
- [103] B. Li, D. Vretenar, Z. X. Ren, T. Nikšić, J. Zhao, P. W. Zhao, and J. Meng. Fission dynamics, dissipation, and clustering at finite temperature. *Phys. Rev. C*, 107: 014303, Jan 2023. doi: 10.1103/PhysRevC.107.014303. URL <https://link.aps.org/doi/10.1103/PhysRevC.107.014303>.
- [104] P.-G. Reinhard, J. A. Maruhn, A. S. Umar, and V. E. Oberacker. Localisation in light nuclei. *Phys. Rev. C*, 83:034312, Mar 2011. doi: 10.1103/PhysRevC.83.034312. URL <https://link.aps.org/doi/10.1103/PhysRevC.83.034312>.

- [105] J.-P. Ebran, M. Girod, E. Khan, R. D. Lasseri, and P. Schuck. α -particle condensation: A nuclear quantum phase transition. *Phys. Rev. C*, 102:014305, Jul 2020. doi: 10.1103/PhysRevC.102.014305. URL <https://link.aps.org/doi/10.1103/PhysRevC.102.014305>.
- [106] Tjalling Koopmans. Über die Zuordnung von Wellenfunktionen und Eigenwerten zu den einzelnen Elektronen eines Atoms. *Physica*, 1(7-12):104–113, 1934. doi: 10.1016/S0031-8914(34)90011-2.

A | Appendix

A.1. Spherical harmonics

Spherical harmonics, of degree λ and order μ , are defined as

$$Y_{\lambda\mu}(\theta, \phi) = (-1)^\mu \sqrt{\frac{2\lambda+1}{4\pi} \frac{(\lambda-\mu)!}{(\lambda+\mu)!}} P_\lambda^\mu(\cos \theta) e^{i\mu\phi}. \quad (\text{A.1})$$

Being able to provide the expression for arbitrary μ, λ through an algorithm is important in the current framework, to solve the Poisson equation and investigate nuclear properties.

The major challenge is to generate the associated Legendre polynomials P_λ^μ . They can be expressed in the form (for positive μ)

$$P_\lambda^\mu(x) = (1-x^2)^{\mu/2} \frac{d^\mu P_\lambda(x)}{dx^\mu}, \quad (\text{A.2})$$

where $x = \cos \theta$ and

$$P_\lambda(x) = \frac{1}{2^\lambda \lambda!} \frac{d^\lambda (x^2 - 1)^\lambda}{dx^\lambda}. \quad (\text{A.3})$$

To compute the arbitrary λ, μ associated Legendre polynomial we can employ a recursive approach, setting $\lambda = \mu$

$$P_\mu^\mu(x) = (2\mu - 1)!! (1 - x^2)^{\mu/2}, \quad (\text{A.4})$$

where $(2\mu - 1)!! = 1 \cdot 3 \cdot 5 \dots (2\mu - 1)$ denotes the double factorial. Once $P_\mu^\mu(x)$ is known, the next element with $\lambda = \mu + 1$ reads

$$P_{\mu+1}^\mu(x) = x(2\mu + 1) P_\mu^\mu(x). \quad (\text{A.5})$$

All higher degrees are then generated using the standard upward recurrence relation in λ :

$$(\lambda - \mu + 1) P_{\lambda+1}^\mu(x) = (2\lambda + 1) x P_\lambda^\mu(x) - (\lambda + \mu) P_{\lambda-1}^\mu(x), \quad (\text{A.6})$$

valid for all $\lambda \geq \mu + 1$.

A.1.1. Algorithm

1. Compute the base case P_μ^μ from the closed-form formula.
2. If $\mu = \lambda$ the procedure ends, otherwise
3. Evaluate $P_{\mu+1}^\mu$, if $\lambda = \mu + 1$ the procedure ends, otherwise
4. Apply the recurrence relation $P_{\lambda+1}^\mu$ until the desired degree is reached

This ought to be applied only for $\mu \geq 0$. For $\mu < 0$ the procedure is carried out using $-\mu$ and in the end using the relation

$$Y_{\lambda-\mu} = (-1)^\mu Y_{\lambda\mu}^*. \quad (\text{A.7})$$

A.2. 5-point derivatives

The first and second derivatives of a function $\psi(x)$ in $x = x_i$, using 5-points formulae, read

$$\psi'(x_i) = \frac{\psi_{i-2} - 8\psi_{i-1} + 8\psi_{i+1} - \psi_{i+2}}{12h} \quad (\text{A.8})$$

$$\psi''(x_i) = \frac{-\psi_{i-2} + 16\psi_{i-1} - 30\psi_i + 16\psi_{i+1} - \psi_{i+2}}{12h^2} \quad (\text{A.9})$$

A.3. Functional derivatives

Given a functional $\mathcal{F}[\rho]$, the functional derivative is defined as the variation of \mathcal{F} with respect to a small change in the density ρ , formally

$$\frac{\delta \mathcal{F}[\rho]}{\delta \rho} = \lim_{\delta \rho \rightarrow 0} \frac{\mathcal{F}[\rho + \delta \rho] - \mathcal{F}[\rho]}{\delta \rho}.$$

Power dependence Let us suppose to have $\mathcal{F}[\rho] = A\rho^\sigma$, where A is a constant. A variation $\delta \rho$ of ρ yields

$$\mathcal{F}[\rho + \delta \rho] - \mathcal{F}[\rho] = A[(\rho + \delta \rho)^\sigma - \rho^\sigma].$$

Expanding to first order in $\delta \rho$ (Taylor expansion) we obtain

$$(\rho + \delta \rho)^\sigma = \rho^\sigma + \sigma \rho^{\sigma-1} \delta \rho + \mathcal{O}((\delta \rho)^2),$$

hence

$$\mathcal{F}[\rho + \delta\rho] - \mathcal{F}[\rho] = A\sigma\rho^{\sigma-1}\delta\rho + \mathcal{O}((\delta\rho)^2).$$

Dividing by $\delta\rho$ and taking the limit $\delta\rho \rightarrow 0$ gives the usual result for the functional derivative

$$\frac{\delta\mathcal{F}[\rho]}{\delta\rho} = A\sigma\rho^{\sigma-1}. \quad (\text{A.10})$$

Divergence of a vector field Consider the functional

$$\mathcal{G}[\mathbf{J}](\mathbf{r}) = \nabla_{\mathbf{r}} \cdot \mathbf{J}(\mathbf{r}).$$

A small variation $\delta\mathbf{J}$ induces

$$\delta\mathcal{G}(\mathbf{r}) = \nabla_{\mathbf{r}} \cdot \delta\mathbf{J}(\mathbf{r}).$$

We can express the variation $\delta\mathbf{J}(\mathbf{r})$ in terms of its values at all points \mathbf{r}' as

$$\delta\mathbf{J}(\mathbf{r}) = \int d^3r' \delta\mathbf{J}(\mathbf{r}') \delta(\mathbf{r} - \mathbf{r}').$$

Substituting this into the expression for $\delta\mathcal{G}(\mathbf{r})$ yields

$$\delta\mathcal{G}(\mathbf{r}) = \int d^3r' \nabla_{\mathbf{r}} \cdot [\delta\mathbf{J}(\mathbf{r}') \delta(\mathbf{r} - \mathbf{r}')].$$

Since \mathbf{r} and \mathbf{r}' are independent variables, the derivative acts only on the delta function:

$$\delta\mathcal{G}(\mathbf{r}) = \int d^3r' (\nabla_{\mathbf{r}} \delta(\mathbf{r} - \mathbf{r}')) \cdot \delta\mathbf{J}(\mathbf{r}').$$

By the definition of the functional derivative as the kernel relating $\delta\mathcal{G}(\mathbf{r})$ to $\delta\mathbf{J}(\mathbf{r}')$, we can read off

$$\frac{\delta\mathcal{G}[\mathbf{J}](\mathbf{r})}{\delta\mathbf{J}(\mathbf{r}')} = \nabla_{\mathbf{r}} \delta(\mathbf{r} - \mathbf{r}'). \quad (\text{A.11})$$

In compact vector form [77],

$$\frac{\delta(\nabla_{\mathbf{r}} \cdot \mathbf{J}(\mathbf{r}))}{\delta\mathbf{J}(\mathbf{r}')} = \nabla_{\mathbf{r}} \delta(\mathbf{r} - \mathbf{r}').$$

A.4. \bar{U} , \bar{V} matrix structure

The blocked form of the \bar{U} and \bar{V} matrices in Section 3.2.2 is given by

$$\bar{U} = \begin{pmatrix} 0 & & & & \\ & \ddots & & & \\ & & 0 & & \\ & & u_1 & 0 & \\ & & 0 & u_1 & \\ & & & & \ddots \\ & & & & u_n & 0 \\ & & & & 0 & u_n \\ & & & & & 1 \\ & & & & & & \ddots \\ & & & & & & & 1 \end{pmatrix}$$

$$\bar{V} = \begin{pmatrix} 1 & & & & & \\ & \ddots & & & & \\ & & 1 & & & \\ & & & 0 & v_1 & \\ & & & -v_1 & 0 & \\ & & & & & \ddots \\ & & & & & 0 & v_n \\ & & & & & -v_n & 0 \\ & & & & & & 0 \\ & & & & & & & \ddots \\ & & & & & & & & 0 \end{pmatrix}$$

Elenco delle figure

1.1	Binding energy per nucleon as a function of A .	6
1.2	Visual representation of the liquid drop model.	8
1.3	Graphical representation of the harmonic oscillator shells, together with the spin-orbit coupling.	11
1.4	Odd-even staggering for Sn isotopes.	13
1.5	Nilsson model single-particle energy levels trends.	17
1.6	Graphical representation of possible octupole deformations.	18
1.7	Fission path of ^{226}Ra , with different imposed spatial constraints.	19
1.8	Visual representation of the fission process.	20
4.1	Comparison between the steepest descent method and the conjugate gradient method.	64
4.2	Pseudocode of the Hartree–Fock program.	75
4.3	HF calculation convergence with varying CG tolerance for ^{16}O .	76
4.4	HF calculation convergence with varying number of inverse power steps for ^{16}O .	76
4.5	HF calculation convergence with varying number of inverse power steps for the deformed nucleus ^{24}Mg .	77
4.6	Numerical stability map of the HF solver for ^{16}O for different box and step sizes.	78
6.1	Comparison between the two formulae for β_2 .	91
6.2	^{24}Mg ground state density $\rho(x, 0, z)$.	94
6.3	^{24}Mg ground state density $\rho(x, y, 0)$.	95
6.4	^{24}Mg Deformation curves comparison with EV8.	96
6.5	Comparison between the SkM* and the SLy4 Skyrme functionals of the ^{24}Mg deformation curves.	97
6.6	Particle densities and NLFs in ^{20}Ne for different Skyrme functionals.	99
6.7	^{42}Si density $\rho(x, 0, z)$.	101
6.8	^{28}S density $\rho(x, 0, z)$.	102

Elenco delle tabelle

1.1	A typical parametrisation of the coefficients in the SEMF (1.3).	8
1.2	Typical Woods–Saxon potential parameters.	9
5.1	Parameters used to compute the charge mean square radius.	80
5.2	^{16}O including C_0^ρ , C_1^ρ , C_0^τ , C_1^τ terms and neglecting the Coulomb interaction.	81
5.3	^{16}O including C_0^ρ , C_1^ρ , C_0^τ , C_1^τ , $C_0^{\nabla \cdot J}$, $C_1^{\nabla \cdot J}$ terms, neglecting the Coulomb interaction and J^2 terms.	82
5.4	^{16}O neglecting the Coulomb interaction.	83
5.5	^{16}O complete of the Skyrme functional and Coulomb interaction.	84
5.6	Results for the spherical ^{48}Ca .	85
5.7	Results for the spherical ^{56}Ni .	86
5.8	Results for the spherical ^{90}Zr .	87
5.9	Comparison of experimental binding energies and charge radii with theoretical values calculated using the SLy5 functional.	88
6.1	Results for ^{24}Mg ground state, SkM* parametrisation.	92
6.2	Single-particle energy levels in the ground state of ^{24}Mg .	93
6.3	Results for ^{42}Si .	100
6.4	Results for ^{28}S .	101

List of Symbols

Variable	Description	Value (SI units)
c	Speed of light in vacuum	2.99792458×10^8 m/s
e	Elementary charge	$1.602176634 \times 10^{-19}$ C
\hbar	Reduced Planck constant	$1.054571817 \times 10^{-34}$ J·s
m_p	Proton mass	$1.67262192 \times 10^{-27}$ kg
m_n	Neutron mass	$1.67492749 \times 10^{-27}$ kg
μ_N	Nuclear magneton	$5.050783746 \times 10^{-27}$ J·T ⁻¹

